UTS UNIVERSITY OF TECHNOLOGY SYDNEY

Performance of structures to simultaneous blast loading and fragment impact

by JIA YUAN LIM

Thesis submitted in fulfilment of the requirements for the degree of

Master of Engineering (Research)

under the supervision of Professor Chengqing Wu and Associate Professor Jun Li

University of Technology Sydney
Faculty of Engineering and Information Technology

August 2025

CERTIFICATE OF ORIGINAL AUTHORSHIP

I, Jia Yuan Lim declare that this thesis, is submitted in fulfilment of the requirements for the award of MASTER OF ENGINEERING (RESEARCH), in the School of Civil and Environmental Engineering at the Faculty of Engineering and Information Technology at the University of Technology Sydney.

This thesis is wholly my own work unless otherwise referenced or acknowledged. In addition, I certify that all information sources and literature used are indicated in the thesis.

This document has not been submitted for qualifications at any other academic institution.

This research is supported by the Australian Government Research Training Program.

Signature:

Production Note:
Signature removed prior to publication.

Date: 11 August 2025

ACKNOWLEDGEMENT

My heartfelt gratitude goes to my supervisor, Professor Chenqing Wu, for his invaluable counsel, support, and steadfast encouragement through my MEng journey. His expertise and insightful feedback have played a crucial role in defining and refining my research. I am also deeply appreciative of Associate Professor Jun Li whose constant encouragement and constructive feedback pushed me towards excellence. His advice and expertise in numerical methods have been instrumental in my progress. My sincere thanks go to my supervisors from the Defence Science and Technology Agency, Singapore for sponsoring me to pursue this MEng Degree. I am especially grateful to Er Yong Hong Koh for his trust in me and steadfast support. Additionally, I am also thankful for Dr Kok Wei Kang and Dr Melvin Goh for their mentorship and for continuously challenging me to improve my work.

Lastly, on a personal note, I would like to thank my wife Samantha for the unwavering belief in me and constant support she has provided on my journey.

LIST OF PUBLICATIONS

This thesis builds on the research that was presented in the following papers:

I. Lim, J. Y., Goh, C. Y. M., Kang, K. W., Li, J., & Wu, C. (2025). Structural response of steel-concrete composite panels to near field simultaneous blast and fragmentation loading. *International Journal of Impact Engineering*, *195*, 105142.

Table of contents

LIST OF FIGURES

LIST OF TABLES

NOTATIONS

Latin

D	Detonation Velocity
d	Diameter of Primary Fragments
B	Width of the SCC panel
C	Mass of High Explosive
C_{EB}	Equivalent bare charge mass
CS	Cowper-Symonds
F_p	Peak Fragment Impact Force
f'_c	Concrete Compressive Strength
l_c	Length of the Case of the Charge
M_c	Mass of Case
M_{el}	Elastic Moment Capacity
M_f	Total fragment mass
M_{pl}	Plastic Moment Capacity
P_p	Peak Fragment Impact Pressure
R	Distance from Centre of Detonation
T_a	Fragment Arrival Time
T_p	Duration of Fragment Penetration
t_c	Thickness of Concrete
t_{pf}	Thickness of Concrete required against perforation
t_s	Thickness of the Steel
V_0	Initial Fragment Velocity
V_r	Residual Velocity of the Fragment after Perforation
V_s	Striking Velocity
V_x	Critical Perforation Velocity
W_f	Single Fragment Weight
X_f	Penetration Depth into Concrete
X_s	Penetration Depth into Steel

Greek

θ	Taylor's angle

Abbreviations

ALE	Arbitrary Lagrange Euler
DIF	Dynamic Increase Factors
EOS	equation of state
HSC	High Strength Concrete
JC	Johnson-Cook
JWL	Jones-Wilkins-Lee
MM-ALE	Multi-Material Arbitrary Lagrangian-Eulerian
NSC	Normal Strength Concrete
RC	Reinforced Concrete
SALE	Structured Arbitrary Lagrangian Eulerian
SCC	Steel Concrete Composite
SDOF	Single Degree of Freedom

TOA	Time of Arrival
UHPC	Ultra High-Performance Concrete

ABSTRACT

In the current climate of uncertainty, protection of critical infrastructures against explosion is becoming a significant design aspect to be considered. Steel-concrete composite (SCC) sandwich panels have proved superior performance in blast environments and are used for blast doors and blast walls in protective infrastructure for protection against blast loads and fragment impact in far-field loading regimes. In the design of such panels in far-field scaled distances, modern design standards address blast and fragment loading separately. However, in close-in explosion scenarios, the synergistic damage potential from the simultaneous blast loading and fragment impact needs to be considered. As knowledge in this field is limited, an explosive test was performed to evaluate the damage to the SCC panels exposed to cased charges detonated at a close-in scaled distance of 0.39 to 0.78 $m/kg^{1/3}$. The response of the panels from the combined effects was assessed, revealing significant structural damage from the fragment impact. However, the panels successfully retained their structural integrity throughout the tests. A characterization test was conducted to quantify the blast overpressure and the fragment properties from the cased charge. Subsequently, the panels were subjected to three-point quasi-static load tests to compare the difference in their load resistance between a panel in pristine condition, and the post-blast panels with various damage conditions due to the explosive effects. Furthermore, numerical studies were performed to examine the dynamic response and the corresponding failure modes of SCC panels to the combined loads, validated with experimental data reported. Individual fragments were modelled using rigid materials and assigned initial velocities based on analytical solutions. The charge was modelled with Arbitrary Lagrangian-Eulerian (ALE) formulations and coupled with the SCC panel modelled with Lagrangian formulations to obtain a coupled fluid structure interaction. The numerical model demonstrated good agreement in damage patterns and structural deflections. Subsequently, a simplified approach was proposed to estimate the structural deformation of SCC panels subjected to the combined loadings. The model returned favourable match with the maximum deflection time history although the damage mode was not fully replicated in the panel. The significance of the study lies in their relevance to the design of protective structures vulnerable to extreme loads induced by cased charges at a close-in loading regime.

1. INTRODUCTION

1.1. Definition and Background

The global escalation of terrorism since the turn of the 21st century, coupled with the increased accessibility to advanced technologies, has raised significant concerns worldwide on the potential explosive threats to critical infrastructures. In the event of an explosion, structural members may fail and trigger a structural collapse, endangering the lives of hundreds or thousands of occupants and crippling the operations of critical infrastructures. Hence, engineering protective systems that are capable of protection against an explosive event in critical infrastructures is a significant design aspect to be considered.

Steel-concrete composite structures have become prevalent in contemporary construction due to its ease of construction, facilitated by prefabrication technologies. These structures leverage the combined strength of concrete and steel, optimizing material utilization in design. Steel Concrete Composite (SCC) panels are constructed by steel plates that is framed with stiffener beams forming a sandwich panel. The centre core is then infilled with concrete that is connected mechanically to the steel plates to form an integral structure. In recent years, performance of SCC panels to far field explosive environments has been validated, extending the use of these panels in nuclear facilities and protective infrastructure (Liew at al., 2010; Varma, 2014; Bruhl, 2015). As threat scenarios evolve, protective systems are required to perform under more complex threat scenarios, one such threat scenario is a cased explosive detonated at close-in scaled distances. Under such loading regimes, the need to consider fragment loading and the synergistic damage potential with the simultaneous blast loading significantly complicates the analysis (Girhammer, 1990). Modern design manuals like UFC 3-340-02 (DOD, 2008) recommend the consideration of the blast overpressure and fragment effects separately in the design analysis. The fragment impact is managed by analysing the penetration resistance of the section from a single fragment impact while the blast effects are analysed through localised material damage and global dynamic response. When the cased charge is detonated at close-in stand-off distances, the structure would be subjected to the simultaneous impact of multiple high-velocity fragments, along with the blast overpressure. The fragment impact causes localized damage from the penetration due to the impact into the structure. Simultaneously, momentum from the fragment mass upon impact is transferred to the panel (Grisaro et al., 2018).

A research gap in the study of close-in explosive tests of SCC panels to cased charges at lesser than 1.2 m/kg$^{1/3}$ was identified, underscoring the need to evaluate the performance of SCC panels in an explosive environment at close-in ranges.

1.2. Research Objectives

This study seeks to expand the comprehension of the dynamic behaviour of SCC panels that are exposed to simultaneous blast loading and fragment impact through comprehensive review, experimental tests and refined numerical modelling. The goal is to propose a design approach for SCC panels against the combined loading. This thesis aims to:

- Examine the performance of SCC panels to blast loading and fragment impact at close-in stand-off distances through experimental testing.
- Quantify blast overpressure and fragment characteristics from an explosive cased charge at close-in standoff distances through experimental testing and numerical studies.
- Quantify structural response of SCC panels to combined loading at close-in stand-off distances based on the experimental testing, and numerical studies.

To attain these objectives, the overview of the scope of work is as follows.

- Conduct an extensive review of analytical, numerical, and experimental works in far field and near field blast loading on steel concrete composite panels that address the derivation of structural responses to blast loading.
- Conduct experimental test program consisting of three phases: 1) Characterization test for case charge effect, 2) field blast tests and 3) quasi-static load test for post-test panels.
    - The charge characterization test consists of 2 instrumented field tests in an arena setup to obtain the blast loading profiles and fragments distribution and velocity.
    - The field blast test consists of SCC panels that are exposed to the combined effects of cased charges at scaled distances Z=0.39 m/kg$^{1/3}$ to 0.78 m/kg$^{1/3}$.
    - Three-point quasi-static load tests were conducted to establish the panel's load resistance. The test was conducted on 3 types of panels, 1) pristine panel, 2) fragment damaged panel and 3) panel subjected to combined loads to distinguish the difference between their resistances in pristine condition and residual capacities.
    -

- Numerical study on the experimental tests:
  - Numerical studies to simplify the blast hazards description from the cylindrical cased charge to a cylindrical bare charge validated with the results from the charge characterization test. The numerical study addresses the complexity of estimating the blast overpressure from a cylindrical charge, attending to issues such as model parameter selection (JWL parameters, mesh size) and accounting for possible shape effects on the resultant overpressure profile. Comparisons on the loading profile at varying scaled distances are made with conventional estimations (from spherical charges) from UFC 3-340-02.
  - Numerical studies to replicate the blast test to establish the structural response mechanism of the panels to combined loads. First, the baseline response with conventional blast design is predicted. The panels are loaded with only blast loading to evaluate the baseline structural response without the influence of fragments. Next, the fragments were included into the model to replicate the structural response, validated against the experimental tests.
  - A simplified methodology including to idealise the fragment load was proposed. The additional impulse from fragment loading is applied to the panel and the structural response obtained from the numerical modelling and the experiments is analysed and quantified.
  - Lastly, optimisation studies were performed to examine how different material build-up of the sandwich panels affected their response to improve future design of SCC panels in protective engineering applications.

This thesis is structured into five chapters. Chapter One introduces the background of the study and discusses the motivation behind it. It also outlines the main objectives and defines the scope of the research. Chapter Two provides a literature review covering current analytical design methodologies addressing concurrent blast and fragment loading, as available in the public domain. It explores protective structural components and the numerical methods relevant to these threats. Chapter Three presents a test programme carried out by the Defence Science and Technology Agency (DSTA) of Singapore, in collaboration with the Swedish Defence Research Agency (FOI), to assess the performance of SCC panels subjected to concurrent loading from blast and fragments. The contributions from Roger Berglund, Martin Nilsson, Oskar Paradis and Tobias

Carlberg from FOI to the success of the program are gratefully acknowledged. In this chapter, the author was responsible for reporting, validating and investigation of all experimental test reported, including the charge characterization tests, field blast tests and quasi-static load tests. The experimental results were compared with analytical predictions and key findings were discussed. Chapter Four focuses on numerical investigations, introducing a validated model capable of simulating the damage and structural response of SCC panels under the combined loads. The numerical study first presents on the calibrating the charge material parameters and weight. Next, a coupled model was presented, simulating the response of the panel from the blast loads through fluid structure interaction techniques and incorporating the fragment impact loads by unique contact modules. Subsequently, a simplified version of the model is also proposed to capture the maximum structural response. Additionally, an optimisation study is included to compare SCC panel performance and demonstrate their advantages in high-threat scenarios.

Chapter Five concludes the thesis by summarising the outcomes of the experimental, analytical and numerical work. It also identifies areas requiring further research to address the knowledge gaps revealed in this study.

2. LITERATURE REVIEW

2.1. Introduction

Critical infrastructures are vulnerable to explosive threats from both intentional and accidental sources. The designs of infrastructures against these explosive threats are complex and are dependent on several considerations, such as 1) scaled distance (Z) of the charge, 2) type of explosive charges, 3) cased or bare charges to determine the response of the structures. This chapter consolidates the study of the published research and summarizes the foundational concepts for analysing structures subjected to combined explosive loading effects in close-in loading regimes.

2.2. Explosive Charges

When an explosive charge is detonated, a blast wave is formed through the instantaneous release of hot gases that expands to the surroundings. The resultant blast wave produced depends on the elevation of the charge detonation. When the explosive detonates in air, the phenomenon of a Mach front is created when the blast wave reflects off the ground and merges with the incident wave (TM 5-855-1, 1986), as illustrated in Figure 2.1. The resultant pressure of the Mach front is larger than the incident pressure. Whereas in a surface detonation, the ground reflection of the blast wave happens instantaneously and hence a plane wave can be used to approximate the wave front (TM 5-855-1, 1986), as shown in Figure 2.2.

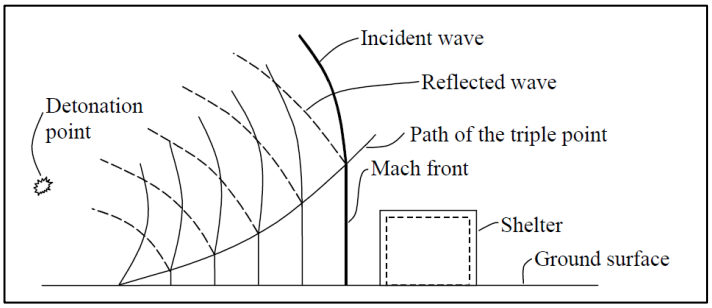

Figure 2.1. Schematic of mid-air blast environment (TM 5-855-1, 1986)

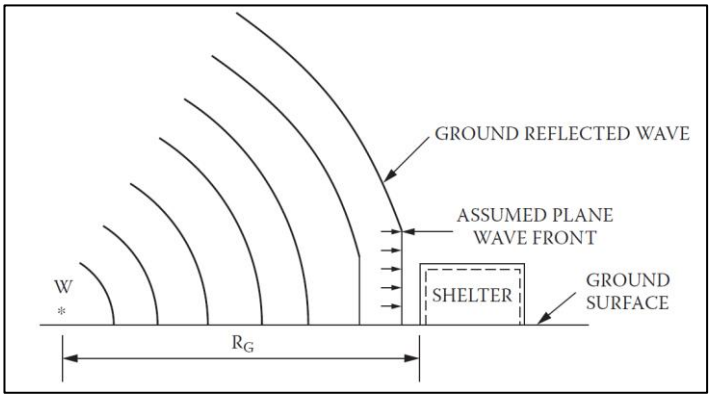

Figure 2.2. Schematic of surface blast conditions (TM 5-855-1, 1986)

Brode (1959) developed close form solutions to describe the blast overpressure generated from a spherical TNT charge. Kingery & Bulmash (1984) used semi-empirical methods to characterize air blast parameters generated by TNT explosions for both spherical and hemispherical air burst. These methods were subsequently implemented to computer code ConWep (Hyde, 1992). Modern standards like the UFC 3-340-02 (DOD, 2008) use scaled distance and a spherical/hemispherical TNT charge assumption for the assessment of the blast overpressures from the high explosives in various applications. While a spherical/hemispherical charge shape assumption provides a consistent benchmark for the scientific study of blast wave propagation, real applications may not always conform to this assumption. The geometry of the charge significantly influences the distribution profile of blast overpressure, highlighting the critical importance of considering charge geometry in blast analysis. The use of cylindrical charges is common, and considerable tests have been performed to characterize the blast wave spatial distribution. In contrast, for a cylindrical charge, the blast waves propagate out from the tubular and end faces of the cylinder, causing reflections and bridging waves when the two wave fronts meet (Knock, 2013). Handbook of HE explosives effects (Petes, 1986) provides peak overpressure conversion from Z= 8 m/kg$^{1/3}$ to 1.6 m/kg$^{1/3}$ for cylindrical charges. It was also shown that at closer scaled distance of less than about 2.6 m/kg$^{1/3}$ the blast along the radial direction of the charge yields higher pressure than a spherical charge, the amplification is larger at closer scaled distances. Additionally, when the slenderness of the cylinder increases, a higher peak overpressure is expected. A large charge length to diameter ratio (L/D) of 3 to 6 can yield higher peak overpressure of up to 1.5 times when compared to charges with L/D ratio of 1 and up to 1.8 times when compared to spherical charges. However, no information was provided for the amplifications of blast impulse. Ismail and Murray (1993) investigated cylindrical charges using tetryl at Z = 2.6 m/kg$^{1/3}$ to 8.2 m/kg$^{1/3}$. They showed blast wave profile is directly influenced by the positioning of the cylindrical charge. At 2.6 m/kg$^{1/3}$ the peak pressure measured along the radius of the charge was considerably larger (about 2 times) than along the long axis for a charge with L/D ratio of 4. At 4 m/kg$^{1/3}$, there was no significant difference in the peak pressure. Another test using a charge with L/D ratio of 2 similarly displayed larger (about 1.5 times) peak pressure measured at 3.3 m/kg$^{1/3}$ along the radial axis as compared to along the longitudinal axis. In addition to the peak pressure, the duration of the blast overpressure and impulse is an important parameter, it was demonstrated that charges with higher L/D

ratio would yield a slower decay in the pressure time history curves, i.e. higher impulse, which is characteristic of a non-spherical blast wave. Zimmerman et al (1999) examined the differences between charges with both spherical and cylindrical geometries with varying aspect ratios. It was reported that the detonation location of the charge would affect both peak pressures and impulse generated. The study found that charges with higher L/D ratios directed a greater amount of energy in the radial direction. Anderson and Kateslis (2001) studied the overpressures of bare cylinder charges at Z = 1 m/kg$^{1/3}$ to 1.7 m/kg$^{1/3}$ and reported similar findings that at near field, the cylindrical charges directed more energy perpendicular to the cylindrical axis and hence higher overpressure as compared to a sphere charge. At far field, the respective blast overpressures are comparable. Wu et al. (2010) performed comparison studies on the blast profile of cylindrical charges and spherical charges at Z = 0.75 m/kg$^{1/3}$ and 3 m/kg$^{1/3}$ with varying length to diameter (L/D) ratios and varying detonation points. Consistent to previous findings, they reported higher peak overpressure along the radius of the charge and higher L/D ratios yielded higher peak overpressures. They also compared peak overpressure of cylindrical charges with L/D = 1 against predictions using UFC-3-340-02 and found that the code underestimated the maximum reflected pressures and impulse along the longitudinal axis but along the radial directions, the pressures were overestimated. They also noted that the code consistently over predicts the peak overpressure for spherical charges in near field conditions (Z less than 2 m/kg$^{1/3}$).

2.3. Cased Explosive Charges

When a cased charge detonates, the explosive filling turns into hot gases and creates a high internal pressure that swells the case and subsequently fracturing it into fragments, as illustrated in Figure 2.3. During the swelling of the case, radial tensile cracks and shear cracks form on the outer and inner face of the casing, respectively. Fragments form when cracks propagate to a free surface, causing them to accelerate instantly away from the detonation point (Curran, 1997.

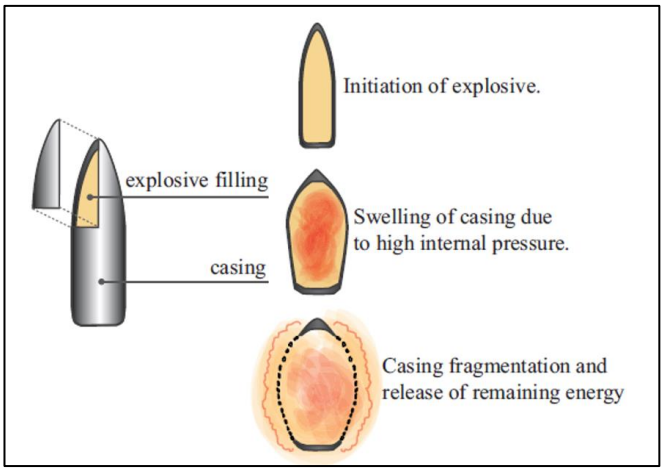

Figure 2.3. Illustration of fragmentation process of a typical cased charge (Nyström, 2013)

Concurrently, the remaining energy expands and propagates the blast wave to the surroundings. Energy and momentum are required to be conserved in the fracturing of the casing into fragments and simultaneous generation of the air blast. Therefore, the resultant blast load has a smaller peak pressure and impulse as compared to a bare charge. Gurney (1943) equated the terminal fragment velocity from the ratio of charge mass (M) against the mass of the case (C) based on energy balance methods. Zulkouski (1976) proposed an exponential formula to model edge wave rarefaction and its effect on fragment launch velocities along the casing's longitudinal axis. On blast effects, Fisher (1953) reported a formula for the calculation of the equivalent charge based on the ratio of the mass of charge against the mass of case. Crowley (2006) argued that using energy conservation is not appropriate as the blast wave imparts strong impulses to the casing, transferring momentum from the explosive gases to the casing. Subsequently, Hutchinson (2009) proposed the calculation of the charge equivalence that is founded on momentum conservation of the explosive and casing. The formula showed good match with experimental data for both low and high M/C ratios.

2.4. Effect of Blast Loading on Building Structures

When a blast wave collides with a concrete surface, compressive stress waves are generated. The stress wave propagates longitudinally and transversely through the structure and can be described with one dimension wave equations derived based on constitutive laws on equilibrium and compatibility. When the wave reflects of the back boundary of the structure, tensile stress waves with equal magnitude are generated due to the low acoustic impedance of air. This results in localized damage, leading to rear-face scabbing failure when the induced tensile stress exceeds the concrete’s tensile strength.

When the explosion occurs near the structure, the blast wave can be strong enough to crush the front face of the concrete and produce a crater, in addition to the rear face scabbing. When the crater and scab zones are large enough such that the failure surfaces join across the cross section, the structure is breached, as illustrated in Figure 2.4.

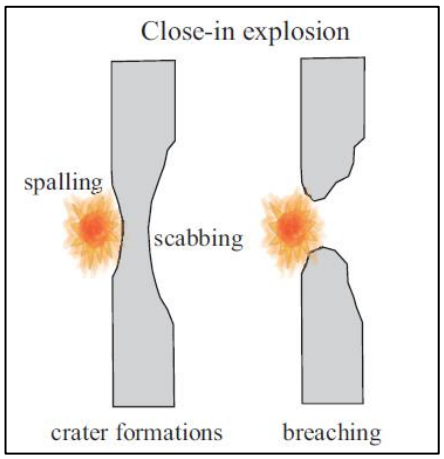

Figure 2.4. Concrete failure modes in close-in explosion scenarios (Nyström, 2013)

The capacity for the materials to resist these localized damage effects will dictate the thickness of the section required. Globally, the stress wave will propagate to the supports and the structural component will respond dynamically in flexural or shear modes. When the materials are loaded dynamically, the effect of the loading rate would cause a strength increase in the materials, thus, UFC 3-340-02 recommends a strength increase of 36% for steel and 25% for concrete under dynamic analysis. The structural dynamic response can be solved analytically through a Single Degree of Freedom (SDOF) analysis (Biggs, 1964), the structure is idealized into a single mass and spring system excited by a forcing function. The displacement of the mass is described through equation of motion and equated against the force time function from Newton's law of motion. The described equations are solved by time step integration for the peak displacements along the structure to quantify the structural integrity (Krauthammer, 2008).

2.5. Fragment Impact on Structures

When a fragment from a cased explosive charge hits the structure, it penetrates the surface causing localized damage to the concrete. The surface concrete will be crushed, forming a crater around the penetrated concrete. Additionally, the regions around the crater will experience substantial cracking and the loss in strength. When fragment impact is sufficiently large, it can create a full perforation through the concrete. Scabbing damage can occur at the rear face of the concrete when the pressure wave created by the fragment

impact transforms into a tension wave upon reflection and exceeds its tensile strength, causing the concrete to crack and fail, as shown in Figure 2.5.

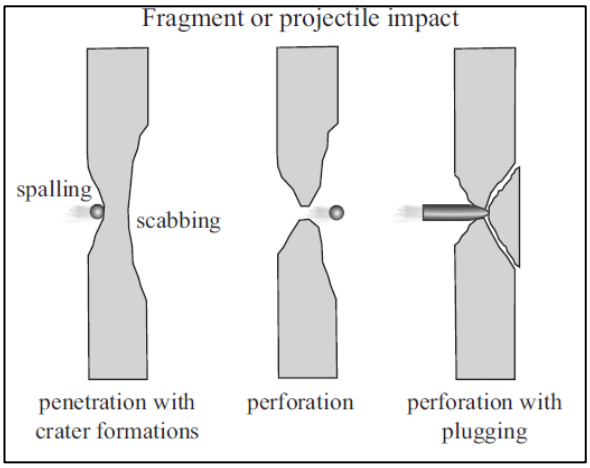

Figure 2.5. Failure modes of concrete from fragment impact (Nyström, 2013)

In the analysis of fragment penetration into multilayered structures, the penetration behaviour within each layer is evaluated independently assuming no interaction of the layers. The trajectory of the fragment is tracked through each layer to determine if perforation occurs. If the fragment perforates the layer, it exits with a residual velocity which serves as the impact velocity for the assessment of the next layer. The structure successfully prevents perforation when the fragment comes to rest within a layer (Krauthammer, 2008). An illustration of this methodology is presented in Figure 2.6.

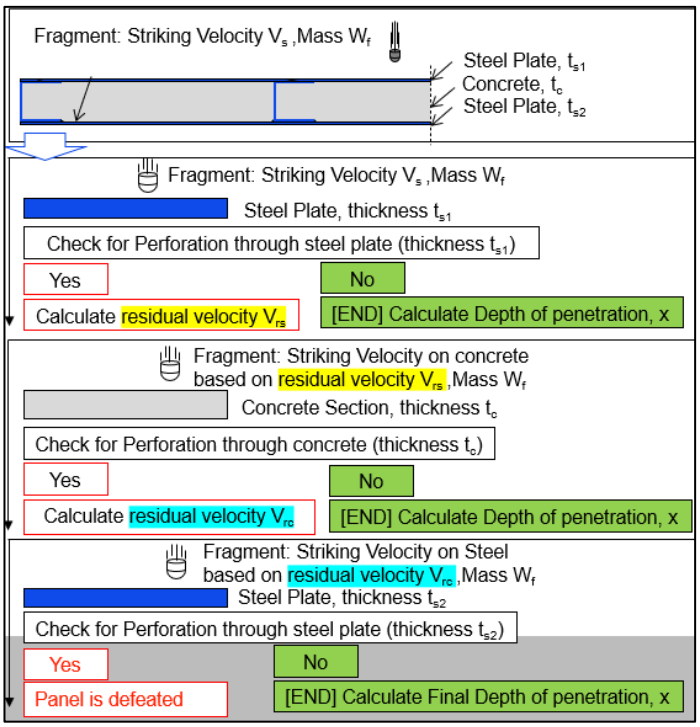

Figure 2.6. Illustration of fragment penetration calculation in multi layered structures

UFC 3-340-02 (DOD, 2008) treats the blast loading and fragment impact analysis separately. Fragment impact is addressed in terms of the penetration resistance through the section, while the blast overpressure is considered for local damage and structural dynamic response.

2.6. Effects of Simultaneous Blast loading and Fragment Impact

When analysing the loading of cased explosives at close-in scenarios, the complexity increases due to the need to account for both fragment loading and its interaction with blast effects (Girhammer, 1990). Along with the blast wave loading, the structure is also subjected to the impact from multiple high velocity fragments. Fragments induce two primary structural responses: first, localized physical damage caused by high-velocity impact and penetration into the structure. In fragment penetration design, codes often treat the fragments as discrete projectiles in perforation or scabbing calculations. At close-in loading ranges, the high density of impacting fragments causes more damage than a single fragment due to potential overlap in spalling or scabbing surfaces (Li et al., 2020). Additionally, the momentum transfer from multiple high-velocity fragments, which is not accounted for in conventional design codes, further amplifies structural damage. Consequently, the combined loading from cased charges in close-in scenarios cause significantly severe damage than that from blast effects of bare charges.

A series of experiments were reported by Hader (1983) to examine local effects to reinforced concrete (RC) walls from bare and cased explosives. It was reported that the cased charges perforated the concrete slabs at up to ten times distances, as compared to a bare charge of similar weight. Similarly, the wall thickness must be scaled up about three times thicker to prevent perforation of cased charges as compared to bare charges of similar weight.

Ernst Mach Institute (Koos, 1987) showed that for close-in detonation of cased charges, the impulses from both the air blast and fragments are loaded onto the structure. The study comprises of bare charge, light cased charge and heavy cased charge, where the ratio of mass of case to mass of equivalent TNT is around 1 and 4, respectively. A higher impulse was experienced by the structure when the weight of the case increased. At $Z= 3$ m/kg$^{1/3}$, a light cased charge yielded impulse that is about 1.6 times as compared to the bare charge. For heavy cased charges, the difference is bigger, the impulse yielded was 2.5 times when compared to the light cased charge and 4 times when compared to the bare

charge. They also reported a difference in the arrival time, at close distances of less than 3 m, the air blast arrives the target first, while fragments would arrive first at further standoff distances of about 10 m.

Nordstrom & Forsen (1994) reported on a series of tests that subjected RC slabs to fragment loading to assess their damage as shown in Figure 2.7. The fragments were formed using steel ball bearings bound to the charge and designed with an areal density of up to 0.2 kg/m^2 and impact velocities between 1500 m/s to 2300 m/s. The fragment sizes were also varied for a fixed areal density to study fragment size effect on the damage. To assess the damage impact to the structural capacity of the slab, a three-point load test was conducted and compared with the pristine panels. They reported that for high fragment density loading of 0.2 kg/m^2, although the maximum resistance of the damaged slab was lower, the slab exhibited more ductility. At about 5 degrees deflection, the energy absorption capability of the damaged slabs was consistently lower. The energy absorption suffered about 50% reduction at fragment velocities of 1600 m/s, and exhibited the most reduction of up to 80% at fragment velocities of 2200 m/s. The energy absorption capacity of the damaged slabs at about 10 deg deflection is also reduced as compared to the pristine panels, however, due to the increased ductility, the reduction is lesser as compared against results from the test at 5-degree rotation. The largest reduction in energy absorption occurred at fragment with the smallest size, highest areal density at velocities of ~2200 m/s. At higher velocities, a smaller reduction was reported. It was reported at 10 deg deflections, the slabs with low areal density loading of 0.1 kg/m^2 showed superior energy absorption as compared to the pristine slabs. This is possibly attributed to the small cracks in the slab caused by the fragments that helped strain the reinforcement bars at multiple locations thus creating a more ductile behaviour.

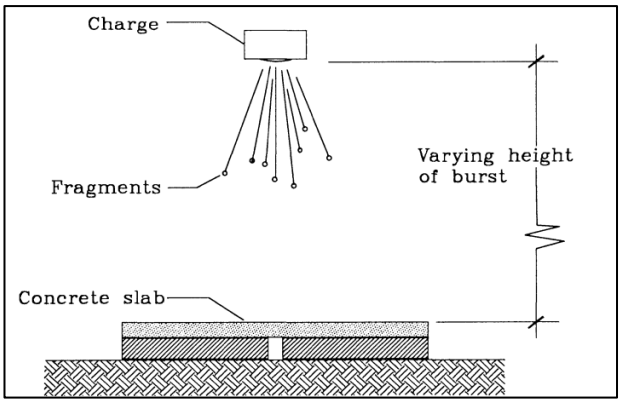

Figure 2.7. Illustration of test setup with fragment loading on slab (Nordstrom & Forsen, 1994)

In the 1980s, the US AFESC conducted a series of tests on RC panels with close-in detonation of cased charges, demonstrating that the synergy of the fragment impact loads and blast pressure from the detonation of a cased charge is more severe than environments created by the blast loads only from an equivalent bare charge (Marchand et al, 1992). They reported that the influence of the ratio of the mass of the casing against TNT significantly affected the damage potential to a concrete structure, i.e., larger breach and spall area. Tests were done at $Z = 0.14$ m/kg$^{1/3}$ for heavy and light cased charge, where the ratio of mass of case to equivalent TNT is around 2.4 and 0.5, respectively. They reported the heavy cased charge produced about 1.7 times more interior stresses on the structure as compared to light cased charge, and 4 times higher as compared to equivalent bare charge.

A series of experiments performed by Held and Tan (2003) attempted to measure the impulse from the fragment impact. They used fixed sleds on roller bearings that received fragment impact from case detonation to derive the fragment impulse and reported that the cased charges generated larger impulses as compared to the bare charges. Furthermore, as the thickness of the case increased, there was corresponding increase in the panel velocity, indicating a higher total momentum transfer. These studies reinforced the need to consider the damage synergy of the combined loading at closed-in loading regimes.

2.7. Materials in Protective Structures

Concrete and steel are the two common building materials used in building of protective infrastructures. The response mechanism of concrete in dynamic conditions and its representation in numerical modelling have been explored extensively. Under dynamic conditions, concrete exhibits a highly non-linear behaviour that cannot be represented in a single constitutive model owing to its dependence on multiple parameters such as the rate of loading and confining pressures. The mesomechanical composition of the concrete which results largely in micro-cracking and plastic compaction of the cement matrix, cell wall buckling causing pore compaction and compaction of the granular composition. To develop an accurate material constitutive model for numerical implementation, these micromechanical effects must be homogenized into a macromechanical framework that appropriately accounts for the interdependence of stress and strain parameters, relating to plastic strain properties, loading strain rate response, damage, and failure. Holmqvist and Whirley (1991) developed concrete material models under high strain rates, large

deformations and high pressure. Subsequently, Malvar et al. (1997) proposed an improved constitutive model for concrete to describe its plastic behaviour along multiple radial paths that integrates an equation of state (EOS) to account for confining pressures and loading rates. The limit state is characterized by three surfaces: the initial yield surface (IYS), the maximum yield surface (MYS), and the subsequent residual failure surface (RFS), as shown in Figure 2.8. When initially loaded, the stresses behave elastically until they reach the IYS, further loading will increase the stresses until the MYS. Beyond this point, the response may either be plastic or exhibit softening behaviour along the RFS. The material model was validated through explosive tests conducted in the 1960s, which involved standard dividing walls subjected to blast loads.

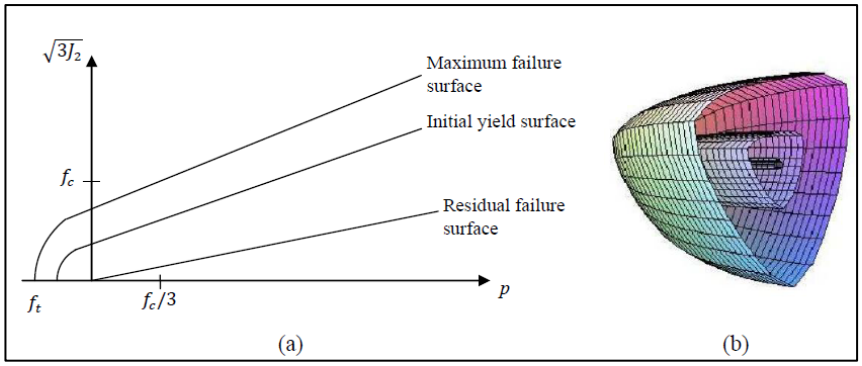

Figure 2.8. Schematic of K&C R3 limit surfaces stresses in (a) 2-Dimensional and (b) 3-Dimensional space

Riedel et al. (2000) introduced the RHT strength model, which integrates an equation of state (EOS) to describe the compaction of pores within the concrete matrix, as illustrated in Figure 2.9. The volumetric compaction of concrete is governed by two primary pressures: 1) crushing pressure of the pores and 2) pressure of compaction. Initially, before reaching the crushing pressure, the volumetric strain adopts a linear correlation, representing the initial compaction of the pores. Once the pores collapse, the cement matrix undergoes plastic compaction, reducing both the effective bulk modulus and the material's volumetric stiffness. As a result, the concrete experiences irreversible compaction, where unloading leads to permanent volumetric strain, following the elastic stiffness down to zero pressure. Once fully compacted and reaching the compaction pressure, a conventional EOS can be applied. The RHT model is similarly defined by three different limit surfaces: 1) the initial elastic yield surface (EYS), 2) the failure surface (FS), and 3) the residual friction surface (RFS). Initially, the material would behave elastically until the EYS is reached. After which, the EYS and FS are interpolated

incorporating plastic properties to obtain the effective yield surface. Once the stresses reach FS, the FS and the RFS are interpolated to obtain the post-failure stress limit surface, that would describe the damage propagation.

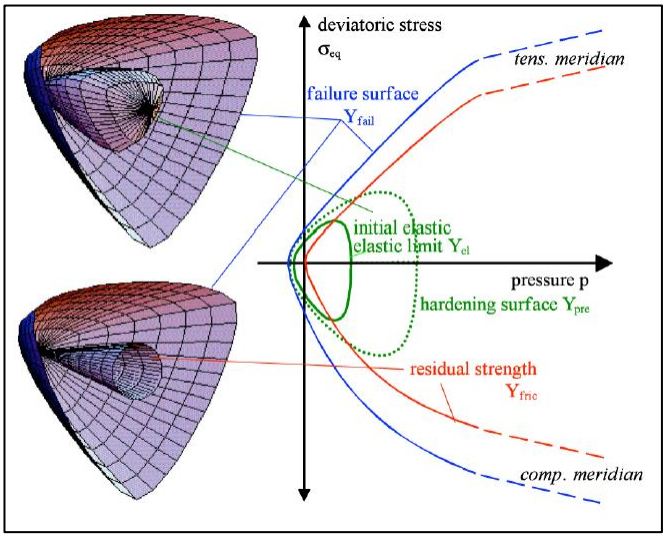

Figure 2.9. Illustration of three RHT limit surfaces (Riedel, 2009)

In contrast with concrete, steel exhibits greater ductility and strength, making it more resistant to blast loading. The Johnson-Cook (JC) material model is widely used to characterize steel behaviour under varying loading rates. Alternatively, the plastic-kinematic model that follows a bi-linear stress-curve, can be used. In this model, the strain-rate dependency is accounted for using the Cowper-Symonds strain rate formulation (Hallquist, 2006).

2.8. Effects of the Combined Loading on Concrete Structures

Since 2000s, computational power and numerical methods have advanced. The study of structural response to blast loading and fragment impact is complex as it involves wave propagation effects, high stress and strain levels and highly non-linear behaviour. The use of hydrocodes in numerical simulations coupled with different finite element methods such as Lagrangian for structural elementals, Arbitrary Lagrange Euler (ALE) for fluids and Smooth Particle Hydrodynamics (SPH) for structures that fractured (e.g. cases with charges) has proofed efficient in solving these problems. General-purpose finite element simulation software such as LS-DYNA and AUTODYN which are developed by Livermore Software Technology Corporation and Ansys, respectively, are used to replicate and study the structural response from blast loading. The research on the simultaneous blast loading and fragment impact is validated by comparing field test

results with numerical studies to evaluate the synergistic damage potential of the combine loading.

Leppanen (2002) highlighted the complexity of numerically modelling simultaneous blast loading and fragment impacts and presented on the challenges of numerically modelling projectile impact penetration into concrete. The analysis was performed with AUTODYN, calibrated against a series of experimental results by Hansson (1998), and was subsequently validated against the experiments that were performed by Forrestal et al. (1994). The analysis was performed with both Eulerian and Lagrangian methods, of which both models predicted the penetration depth well. However, owing to the need for erosion specification in the Lagrangian model, there is an inevitable loss of mass and energy from the model resulting in a non-physical solution, the Eulerian model is therefore preferred. The Eulerian model however costs more computational resources.

Leppanen (2005) conducted component level tests on concrete cubes that were loaded simultaneously with blast and fragment impact at a Z = 0.5 m/kg$^{1/3}$ to 0.86 m/kg$^{1/3}$. The experiment utilized cylindrical charges attached with ball bearings on the surface. The charges impacted concrete blocks positioned between 0.6 m to 1 m away as shown in Figure 2.10. A validated numerical model using AUTODYN was also presented, RHT concrete constitutive model (Riedel, 2000) was used for concrete, and strength parameters were derived from compressive tests and tensile splitting tests conducted, the parameters were subsequently used in the calculations of the failure surfaces and residual strength using model proposed by Attard (1996). The blast overpressure was applied as a piecewise curve derived from ConWep and the fragments were physically modelled to impact the concrete with an initial velocity around 1450 m/s to 1650 m/s, the loads were applied based on their respective estimated time of arrival to the structure. A mesh size approximately similar to the radius of the fragment was found to be optimal, the top quarter along the axis facing the fragment penetration was modelled with the same mesh size to capture the initial penetration behaviour upon impact, the mesh was subsequently made coarser away from the impact face for optimisation. The study reported that damage from combined loading localised and contained within the surface zone of impact, while the concrete strength beneath the impact area remained unaffected. The numerical methods employed effectively simulated the spalling zone, highlighting the importance of accounting for both blast wave and fragment loading to achieve accurate predictions. Comparisons with models considering only blast or fragment impacts revealed that

combined blast and fragment loading resulted in greater overall damage. Additionally, damage within the spalling zone was primarily attributed to fragment impacts, suggesting the potential to distinguish between global structural response and localized damage caused by fragment penetration.

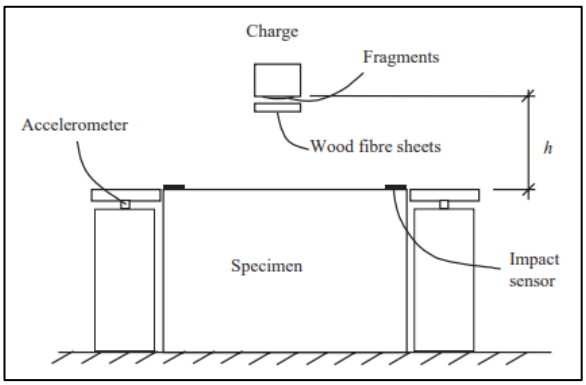

Figure 2.10. Illustration of test setup with fragment loading on slab (Leppanen, 2005)

Nystrom & Gylltoft (2009) performed numerical studies using hydrocode, AUTODYN 3D with Lagrange solver, similar to Leppanen (2005). They studied the blast and fragment loading effects from a 110 kg TNT thin cased explosive at Z = 1 m/kg$^{1/3}$ wall panels spanning 2.7 m. The blast overpressure was applied as a piecewise curve derived from ConWep, and full TNT weight was used without the consideration of TNT reduction due to casing effects. From ConWep's 95% confidence distribution, the fragments weighted 21.9 g. The fragments were modelled as a sphere with 4 mm mesh size and an initial velocity between 1890 m/s to 1760 m/s, with linear elastic material assumption. The loads were applied based on their respective estimated time of arrival to the structure. RHT concrete constitutive model (Riedel, 2000) was used for concrete, and strength parameters were derived from past work by Magnusson and Hansson (2005) and Leppanen (2005). Mesh size of 6 mm was found to be optimal for the modelling of the wall, the top one third along the axis facing the fragment penetration was modelled with the same mesh size to capture the initial penetration behaviour upon impact, the mesh was subsequently made two times coarser (12 mm mesh size) away from the impact face to improve computational efficiency. They reported that high density-fragment impact in close-in case explosions could lead to synergistic scabbing of the concrete, that is not expected from a single fragment impact, illustrated in Figure 2.11. The damage to the concrete section from the fragment penetration occurs almost instantaneously upon impact, which would directly affect the structural response. The study found that the combined loading produced damage synergy that was much greater than the sum of the individual damage

assessed from the blast loads and fragment impact, respectively. Specifically, the midspan deflection of the structure exceeded the combined deflections observed when considering blast and fragment effects separately.

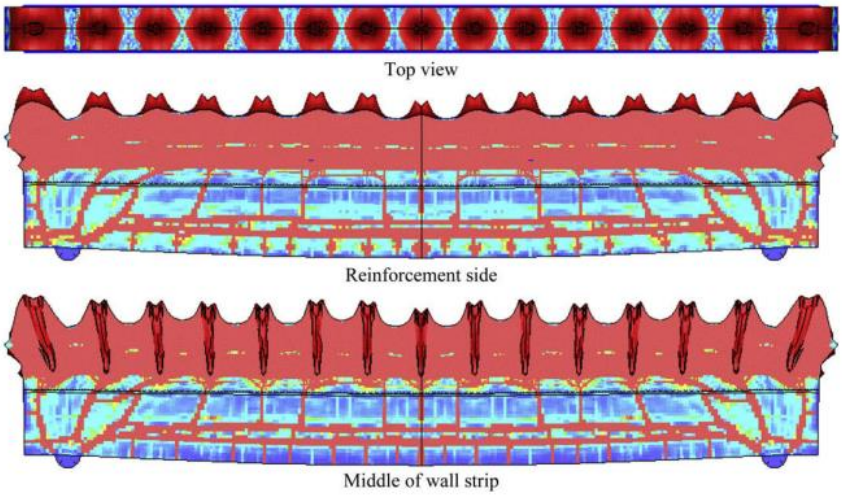

Figure 2.11. Illustration of the damage simulated on concrete (Nystrom & Gylltoft, 2009)

Ek & Mattsson (2009) proposed design methodologies against the simultaneous loading of blast and fragment impact, focusing on the treatment of the fragment loading's impact to a structure. They characterized the fragment impact into two parts: 1) impulse of the fragment and 2) damage to the structure by the fragment penetration. The derivation of the impulse of the fragments is based on momentum conservation from the impact of the fragments to the structure. A triangular pulse was assumed for pressure-time curve of the fragment impact, the time of arrival of the pulse was derived based on the kinematics considering the launch velocity of the fragment from Gurney (1983), accounting for air drag resistance from UFC 3-340-02 (DOD.2008). The loading duration is derived by assuming a linear deceleration along the penetration depth of the fragment. The peak force is derived accordingly based on Newton laws and kinematic equations. According to the fragment loading characteristics, fragment penetration into concrete will partially destroy materials and cause serious localized material damage. Three methods to analyse the removal of the material were studied. The first method involves removing the concrete layer impacted by fragments from the cross section, essentially removing both stiffness and mass of the section. The reduction is implemented at the beginning of the analysis prior to any load application. The second method is like the first, the damaged cross section is removed in the analysis, however, the removal of the section only occurs when the fragments hit the concrete. Finally, the third method involves removing the stiffness of the material in the top layer while retaining its mass, resulting in a substantially reduced

section stiffness to simulate destroyed concrete. Similar to the second method, the removal of the concrete also occurs at the time of the envisaged fragment impact. Subsequently, SDOF analysis using bilinear elasto-plastic material response was compared with finite element analysis and found that the section capacity mobilisation from the FE model was not fully elasto-plastic, hence causing differences in results. The use of a uniform load model to the idealization of the fragment loads provides a good estimation. They concluded the removal of concrete to simulate damage did not give consistent results, in the FE simulations, the removal appeared beneficial while in the SDOF results, the deflections increased, no conclusive explanation was provided.

Forsen (2015) reported experiments which subjected RC slabs to the impact of pre-formed spherical fragments. In the study, they assumed the fragments would strike the structure prior to the blast wave and hence, an equivalent slab that had a reduced section depth was proposed to represent the damage. The fragment impulse was derived based on momentum conservation and was added with the blast impulse with the same time of arrival and loading duration of the blast over pressure, and structure response analysis was performed with the reduced concrete section.

Lan & Morrill (2016) studied numerical methods with LS-DYNA applied with a Lagrange solver for similar studies with large-scale experiments at Z = 0.91 m/kg$^{1/3}$ to 1.3 m/kg$^{1/3}$, with fragment density of 0.17 kg/m^2 to 0.3 kg/m^2. K&C material model was used for the concrete, reinforcement bars were modelled but no details were provided. The blast loads were generated by an equivalent bare charge to account for the energy loss to the case. The fragment loads individually generated by proprietary software KC-Frag are assumed as a triangular pressure-time curve, that is derived from the momentum transfer of individual fragments. The individual fragment impulse was applied to individual elements on the contact surface, as shown in Figure 2.12. It was noted that the fragment impact on the concrete slab was not modelled. They reported that at a close stand-off distance, the damage in the slab can be significantly influenced by the fragment loading and the residual capacities of the structure.

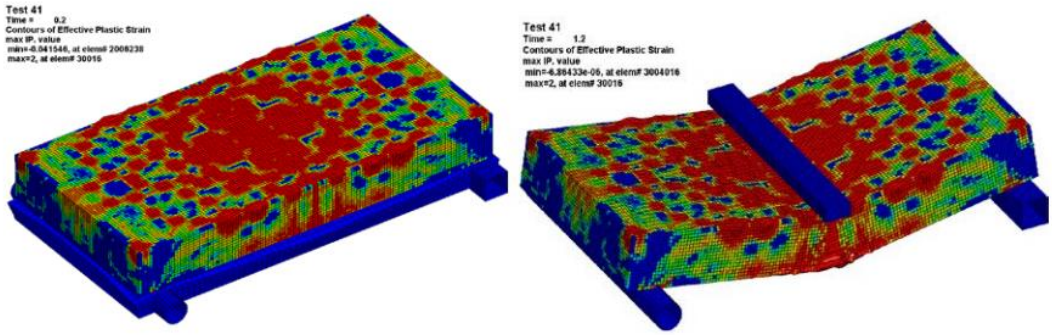

Figure 2.12. Simulation results illustrating replication of structural damage (Lan & Morrill, 2016)

Del Linz (2016) presented tests performed on a rectangular RC slab at Z = 1 m/kg$^{1/3}$ to study the effect of collective blast and fragment loading. The experiment used 8.9 kg cylindrical TNT charges with preformed 8 mm diameter ball bearings glued to the surface of the charge to replicate the fragments, with an expected impact velocity of 1750 m/s. The concrete slab thickness of 100 mm – 200 mm was used for the test and was placed at about 2.1 m standoff distance. They also presented a validated numerical model using Lagrangian formulation. The K&C material model (MAT_72R3) was used to model the concrete (Malvar, Crawford et al., 1997). Fragments were modelled with 1 mm hexahedral elements using JC material to capture the deformation of the fragments as compared to a rigid impactor assumption by other authors (wang, li et al, 2007). They reported that the penetration depth and damage crater around the impact sites in the numerical model agreed closely with the experiment. It was also reported that although there were multiple fragment impacts, no perforation was found in the concrete panel.

Del Linz et al (2021) analysed the structural response of RC panels at a close-in cased blast loading. Two-way concrete wall panels were tested with cased explosives at a close-in distance where shear plugging, and flexural deformations are expected. The results from the experiment revealed severe damage that was concentrated near where the charge was located, the reinforcement bars within the concrete were exposed from the catering and scabbing damage of the concrete. On the rear, extensive spalling of the concrete cover was observed, the deteriorated concrete within the section was held together between the reinforcement bars. In heavily damaged areas, residual thickness of about a few centimetres of concrete was left, indicating the loading was close to breaching threshold. Next, they presented an approach to numerical modelling of the combined loading using smooth particle hydrodynamics (SPH), validated with new experiment conducted and past work. For the concrete structure, hexahedral elements with an average element size

12.5 mm, derived from mesh sensitivity analysis, were used, while constrained beam elements were used for the steel reinforcements. The RC structure is modelled with the RHT material constitutive models which considers pore pressures, stress triaxiality and strain rate dependent strengths. The steel reinforcements were described with JC model with eroding elements to simulate failure. Plastic strain erosion limits of 30% was used to prevent premature localized failure of the elements, this was verified as no reinforcement bars failed in both the numerical and experimental results. A cylindrical cased charge was employed to represent the fragment loading. The charge was modelled using a Lagragian mesh with hexahedral elements of about 5 mm, and the detonation was described by Jones-Wilkins-Lee (JWL) EOS (Menikoff, 2015). To prevent mass loss by element erosion of the fragment, the case was described by SPH particles with JC material model. The particles have low interpolation distance for independent behaviour and a constant mass of 5 g, based on average experimental values. The fragment size distribution would influence the extent of spalling damage due to cratering caused by discrete fragments. The tests show that when the stand-off is near, the damage on the structure is less dependent on the fragment size distribution due to the high impact density, and the assumption of average fragment mass in the numerical model is valid. The contact description between the charge and case adopted surface to node contacts with penalty stiffness ensuring the full transfer of detonation energy to the casing particles. The fragment velocity was calibrated based on the maximum fragment velocity of about 1700 m/s through the erosion parameters of the charge. The blast was affected with ConWep based equations and the consideration of the use of equivalent TNT to account for the casing effect to the charge was not mentioned. The simulation showed that the fragment arrived before the blast in the simulations, comparable with the test. Spalling damage predicted on both faces on the concrete matched the tests well, moreover, the near breaching phenomenal was captured in damage analysis along the section of the concrete, which agreed well with the test observations, as shown in Figure 2.13. The structural response of the panel was deduced through analysis of the velocities and displacement of the around the centre of the panel. An initial shear plug failure was observed from the initial high velocities that were developed. The subsequent reduction of the velocities indicated that the plug failure was disrupted and held back by the surrounding structure. The displacement analysis similarly showed initial plugging phase, and subsequent dynamic flexural deformation of the plate. The differences of the natural

period of a pristine panel against the dynamic response under non-linear conditions were reported at 7 msec and a response between 5 msec to 20 msec, respectively. They also reported that simulations performed with blast loading only significantly underpredicted the damage and structural response. From the deflection profile of the slab from the blast loading only, period of the slab was close to 7 msec, which is approximately the natural period of the pristine panels. This shows that the fragment impacts dominated the concrete response and highlighted the importance of both blast and fragment loading in close-in explosive environments to accurately predict the damage response.

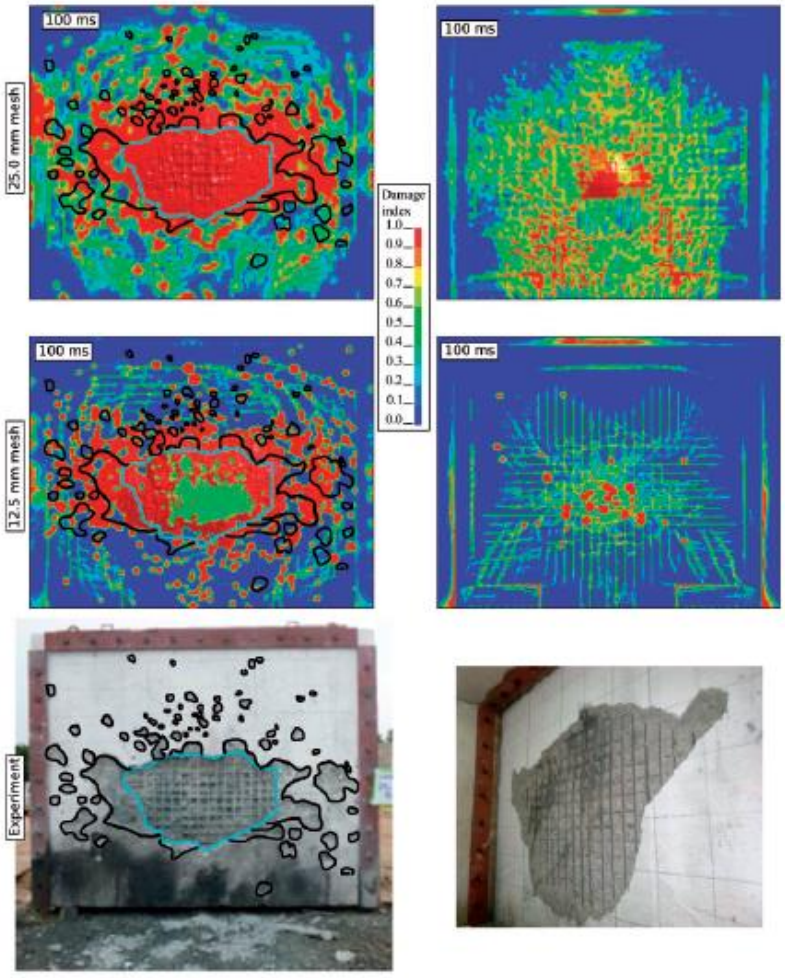

Figure 2.13. Comparison of damage in the concrete between experimental and simulation results (Del Linz et al, 2021)

Li et al. (2020) reported on a series of experiments that subjected RC slabs to blast and fragment loads from case charges to study the damage mode of the structures from the combined loads. A 1 m square RC panel was tested with a heavy cased charge, the mass of TNT was about 850 g and the casing to charge TNT ratio of about 4, at a range of 1.69 $m/kg^{1/3}$ to 3.7 $m/kg^{1/3}$. It was noted that the fragments collected were of different shape

and sizes, and measured average velocity was 1035 m/s. The study reported varying degrees of panel damage, ranging from minor, with only a few through penetrations caused by fragment impacts, to severe, where the concrete was completely breached, leaving large sections of reinforcement bars exposed. They presented a validated 3D numerical model constructed using smooth particle hydrodynamics (SPH) and numerical iterations performed varying both the charge weight and standoff distances independently while keeping the case to charge weight ratio constant. The fragmentation of the cased charge involves complex numerical erosion of failed elements, hence by using SPH which comprises of discrete particles adopting a grid-less Lagrangian hydrodynamics instead of finite elements, the complex element failure computation can be solved. They presented empirical equations for damage prediction of the RC slab based on the numerical simulation iterations. It was noted that the equations predicted the damage to close-in scaled distance of 0.85 m/kg$^{1/3}$, which is an extrapolation from the test data, performed to scaled distance of 1.69 m/kg$^{1/3}$. The study concluded that the synergistic effect of combined loading at close-in ranges cannot be overlooked. It was observed that impacts from multiple fragments led to overlapping spall surfaces, resulting in a significantly larger damage area.

Grisaro et al. (2018) reported field tests performed on RC T-walls that were subjected to combined loading from cased explosives at a scaled distance range from 1.16 m/kg$^{1/3}$ to 2.33 m/kg$^{1/3}$, as shown in Figure 2.14. The case charges used were mainly cylindrical pipe charges which had mass ratios between the case and charge of 1.1. They reported that the cased charges yielded a weaker blast wave as compared to charges without casings, and both the Hutchinson and Fisher models that were used to calculate equivalent TNT yielded good estimations to the experimental results. The fragments recovered followed the form of a Mott distribution. The fragment velocity was estimated by TEMA ARENA software, which gave good agreement with the experiment. The damage due to the high velocity fragment impact is concentrated within a band along the height of the structure, highlighting the importance of the consideration of fragments at close-in scaled distance. Grisaro et al. (2018) characterized the behaviour of blast and fragment loading, identifying two key effects of fragment impact beyond conventional blast loading. First, they highlighted the localized damage caused by individual fragment penetrations. Second, they emphasized the global structural response due to the additional impulse from fragment impacts. In their analysis of the coupled structural response, the

importance of accounting for the arrival timing of both the blast wave and fragments was underscored. Since fragment penetration alters the structure's integrity and natural frequency, it consequently influences the overall structural response. The blast wave propagates in a spherical form and will arrive at each point on the structure at a unique time. Similarly, each fragment along the case has a different initial velocity and will not impact the structure simultaneously, this is further complicated by the difference in mass distribution of the fragments. Studies from Charron (1979) showed that most of the fragments, especially those generated in the middle of the case have similar initial velocity. Comparing the times of arrival, the velocity of the blast wave is about 2000 – 10000 m/s while the fragments are launched at about 1500 – 2500 m/s. However, the blast wave decelerates quicker than the fragments and thus, at close-in ranges, the structure would be struck by the blast wave and subsequently by the fragments, while the fragments will impact the structure first at further loading conditions. Studies conducted by Nystrom (2009) show that for a 250 kg cased charge with 50% mass TNT, the blast wave would arrive at the structure first at distances less than about 5 m, conversely, at further distances, fragment would arrive at the structure first. Similar observations from Krauthammer (2008) and Kazemahvazi et al. (2014) support the understanding of the relative time of arrival between the blast and fragments to be dependent of distance. Conversely, studies by Burchfield (2016) and Forsen (2015) ignored the difference in the arrival time and the blast and fragment were considered reaching the structure simultaneously. The blast and fragment impulse were summed up with the same time of arrival. Additionally, there is significant distinction between the loading time of the blast wave and fragment impact. The duration of the blast overpressure is in the magnitude of several milliseconds, while studies by Mattsson (2009) found that the duration of a fragment penetration is less than 1 ms. The short loading duration of the fragment penetration as compared to the blast overpressure shows that it is reasonable to decouple the effects of the loadings and to first consider fragment damage on the structure and subsequent structural response to the reflected blast overpressure. They subsequently presented a simplified model for the derivation of fragment impulse since it is not discussed in modern design manuals. The simplified model derived average fragment impulse as the total impacting fragment momentum smeared across the area of the structural panel. The total fragment momentum is derived by the total weight of the striking fragments on the structure multiplied by the average fragment velocity striking

the panel. The average fragment velocity is calculated based on the average integration of initial velocities along the length of the cylinder. The force time profile of the fragment impact was derived from Newton's law on conservation of momentum, assuming constant deceleration of the fragment while it is penetrating the structural medium. From kinematics equations, the deceleration can be calculated from the velocity of impact and the depth of penetration, which is estimated from penetration model from UFC-3-340-02 (DOD, 2008). It was noted that the actual deceleration of the projectile in concrete is not constant, as shown in studies conducted by Forrestal (1996), Warren (2014) and Sobeski (2015). They adopted cavity expansion theory and estimated the deceleration of the projectile penetration into concrete to be linear plateau, the deceleration increased until penetration depth of 1.5 – 2.5 times diameter of the projectile and stayed constant through the remaining penetration process. In addition, it was noted that since the depth of penetration directly affects the fragment deceleration and hence the force profile, the shape of the fragment assumed becomes important and it can influence the force time profile by up to 35%. They subsequently presented a series of analytical study on the derivation of the fragment impulse based on the simplified approach proposed, validated with the experiments performed by Helf and Tan (2003). They reported that the fragment pressure time history is similar to that of blast overpressures, described by a sharp rise in pressure and a short loading duration. They elaborated that the impulse is directly dependent on the fragment nose shape as it influences the penetration depth and hence the deceleration of the fragments. Comparing different fragment shapes, they reported that the shape suggested by UFC 3-340-02 yields an average pressure time curve as compared to a sharp nose, which yields about 30% lesser impulse, and a flat nose, which yields about 15% more impulse.

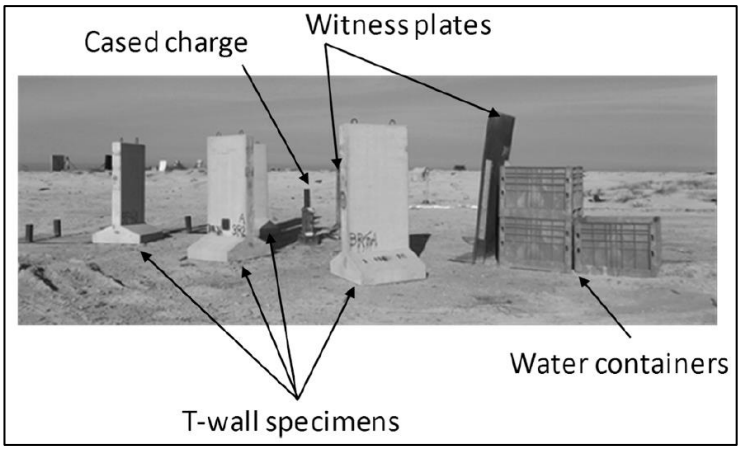

Figure 2.14. Illustration of field blast test arena setup (Grisaro et al., 2018)

Grisaro & Dancygier (2019) presented a methodology and calculation model to account for fragmentation loading effects that are prevalent in cased charges at close-in loading regimes. The method defines zones with high damage as intense strips on the structure, derived from the line of sight of the fragment throw from the cased charge to the structure. These strips are loaded with fragment impulse in addition to blast loads, calculated based on momentum transfer as outlined in previous studies, and accounted for damage by the proposal of an equivalent reduced cross-section height. The equivalent height is derived from the removal of an effective penetration depth from the full height of the section. The effective penetration depth is calculated considering the influence area that is damaged by the fragment penetration, including the front face crater and the actual penetration depth itself. The approach for defining the damage strip was validated with static load-deflection curves test and image analysis from experimental results with good agreement.

2.9. Steel Concrete Composite Structures in Explosive Environments

Steel-concrete composite structures are widely used in protective applications, particularly in blast-resistant designs. SCC panels, commonly employed in blast doors and blast walls, consist of two steel face plates enclosing a concrete-filled core. These components are mechanically connected in various ways to ensure structural integrity and composite action. The connection details between the steel plates and the concrete core are crucial, as the system's performance relies on adequate connector strength and ductility. Under extreme loading, significant deformation occurs, making bond strength highly dependent on connector spacing, anchorage, and design. While these connectors enhance structural performance, their installation requires greater precision, time, and labour. Heng et al. (1995) demonstrated through SDOF analysis that incorporating a concrete core within cellular steel box panels improves blast resistance as compared to hollow configurations. Lan et al. (2005) validated this through experimental tests on sandwich structures that were subjected to bare charges with TNT mass of 100 kg at Z = 1.08 m/kg$^{1/3}$. Their findings showed that panels with air gaps exhibited more than twice the deflection of those infilled with concrete, confirming that the concrete core significantly enhances strength, stiffness, and blast resistance. They concluded that integrating a concrete core within a cellular steel box substantially reduces deflection under blast loading. Liew et al. (2010) further reinforced these findings through experiments on composite panels subjected to bare charge blasts at a scaled distance of 1

m/kg$^{1/3}$. Their research supported the extended use of these panels in protective structures and nuclear facilities (Varma, 2014; Bruhl, 2015).

Kang (2012) investigated the blast resistance of steel composite panels through experimental studies, subjecting them to bare charges with TNT mass of 100 kg at Z = 1.08 m/kg$^{1/3}$, as shown in Figure 2.15. In addition to blast test, quasi-static load tests were performed to compare the static resistance of the panels with different types of connectors, including panels without connectors. The findings revealed that while all panels exhibited similar elastic stiffness and yield points, those without interface shear connectors experienced global compression buckling in the top steel face plate upon yielding. This was due to the absence of mechanical connectors, resulting in reduced plastic resistance when compared to other panels. Blast field tests further demonstrated the superior performance of panels that possessed a concrete core as they sustained significantly less damage than those without a concrete core. The additional mass and stiffness of the concrete core minimized local buckling of the steel face plates, helping the panel maintain its structural integrity and geometry. This highlights the role of the concrete core in enhancing residual load-bearing capacity and mitigating buckling failure after yielding.

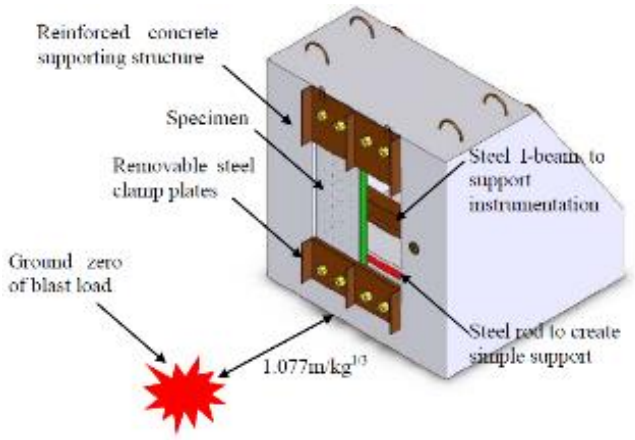

Figure 2.15. Illustration of field blast test on the steel concrete composite panel (Kang, 2012)

A validated numerical model was also presented. It was configured with LS-DYNA software that employed hydrocodes with a Lagragian solver. It was noted that the numerical model was first calibrated based on the quasi-static load test and subsequently validated against the blast test. Shell elements with an elasto-plastic material model were used to model the steel plates (Hallquist, 2006). The concrete core was idealised with solid elements employing K&C concrete (*MAT_072R3) material model (Malvar et al., 1997). The boundary of the steel and concrete is described by a coefficient of friction of

0.25 and a penalty-based approach algorithm was applied to prevent undesired contact merging of the two materials. The blast load is modelled based on ConWep (Hyde, 1992) blast parameters. The numerical model was reported to be able to replicate the structural behaviour of the composite panels to the prescribed blast loadings, as shown in Figure 2.16.

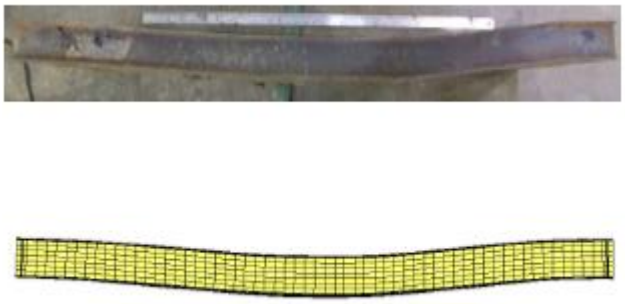

Figure 2.16. Comparison of failure modes from simulations against the experimental results (Kang, 2012)

Rana et al (2019) examined the response of SCC panels to simultaneous blast loading and fragments impact from a cased charge, as illustrated in Figure 2.17. The panels were subjected to a 15 kg TNT charge at a scaled distance of approximately 3.2 m/kg$^{1/3}$. Constructed as welded box sections, the panels consisted of steel face plates encasing a concrete infill, with no mechanical connectors at the steel-concrete interface.

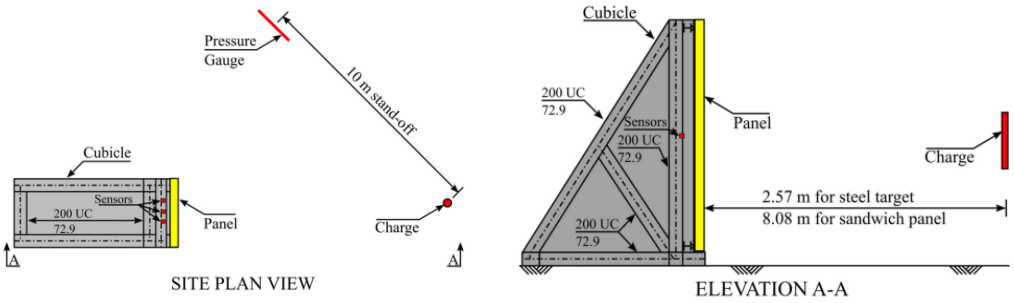

Figure 2.17. Illustration of blast test on the steel concrete composite panel (Rana et al, 2019)

The case used was a 7 mm thick steel tube with a mass ratio of the casing to charge of approximately 1. They reported that the fragments did not perforate the panels and were contained by the concrete core. A numerical model using LS-DYNA with Lagrangian solver that was validated against the blast test was presented. Similar to other studies, the steel concrete sandwich panels were modelled using a Lagrangian mesh. The RHT material model was used to model the concrete core, largely using automatically generated parameters based on the concrete strength input. The steel plate was modelled

using JC model and Gruneisen EOS to account for Dynamic Increase Factors (DIF) under high strain rate loading conditions. The modelling of the contact algorithm between the concrete and the steel plates was not mentioned. The blast loading is modelled with *LOAD_BLAST_ENHANCED which is based on ConWep algorithms. The fragments were modelled with 8 mm solid elements with varying mass based on Motts distribution with velocities calculated based on Gurney equation. It was reported that the validated numerical model was able to replicate the failure mode, as shown in Figure 2.18. Additionally, the model predicted the maximum deflection reasonably well. Additional study was also reported that simplified the modelling of the fragment impact to an equivalent fragment loading impulse that was smeared across the loading surface. They reported that the deflection response of the panels from the simplified load application produced similar deflection response as the models with the fragment impact.

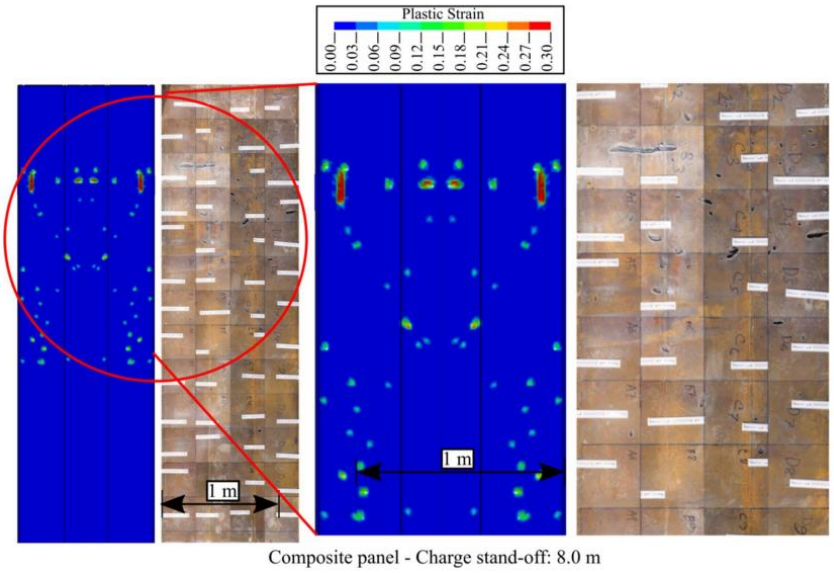

Figure 2.18. Failure modes of composite panels from simulations compared with the experimental results (Rana et al, 2019)

Bruhl and Varma (2018) reported experiments done on steel composite wall panels that were subjected to blast loading induced through a shock tube setup. The tested pressures were equivalent to TNT charges detonated at 2.7 m/kg$^{1/3}$. The study reported that the panels failed primarily in flexure, with no signs of shear failure. Additionally, the measured displacements closely aligned with SDOF calculations, validating the accuracy of the model and demonstrating the panels' effectiveness under far-range blast loading.

Zhao et al (2021) presented a series of experiments done on a 2-way spanning steel composite sandwich panels subjected to damage from 280 g equivalent TNT contact

charges. The sandwich panels tested used commercially available headed shear studs for the interface connections between the steel and concrete as shown in Figure 2.19. It was noted that the length of the stud used was only about one third of the section depth of the concrete, hence the shear studs from the top and bottom steel plates do not have mechanical continuity, as compared to most conventional design. They reported that the sandwich panel performed well in the test, proving their blast resistance against contact charges. There was no breach reported, and the steel plates were effective in confining the concrete and preventing spall damage from the panel. Localized bulging was observed at the rear face of the panel indicating localize failure of the concrete core and steel stud connections.

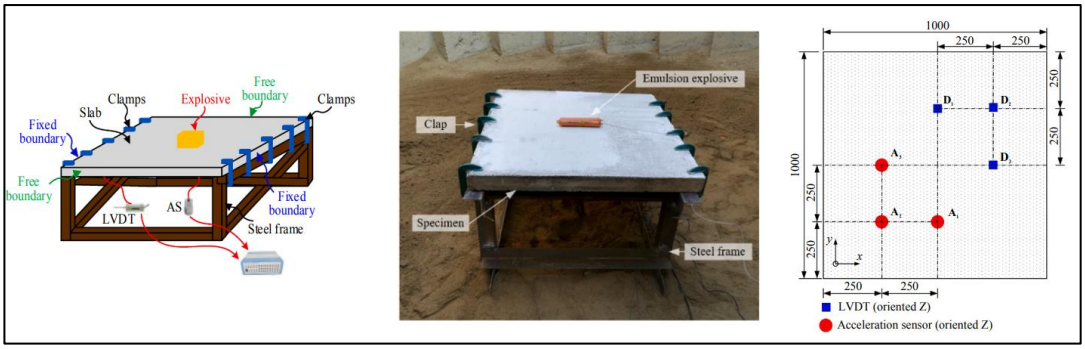

Figure 2.19. Illustration of contact charge test setup on the test panel (Zhao et al, 2021)

A numerical model using LS-DYNA with Lagrangian solver that was validated against the blast test was presented. Similar to other studies, the steel concrete sandwich panels were modelled using a Lagrangian mesh. The concrete adopted the Mat 072R3 material model from K&C largely using automatically generated parameters based on the concrete strength input. The steel plate was idealised with JC model coupled with Gruneisen EOS to account for Dynamic Increase Factors (DIF) under high strain rate loading conditions. The shear connectors were modelled using a linear elastic material model. The air and explosive domains were modelled using the Arbitrary Lagrangian-Eulerian (ALE) method to replicate the coupling of the structures in the fluid, using the algorithm *Constrained_Lagrange_in_Solids. The air was modelled adopting a non-viscous ideal gas assumption. JWL EOS was adopted for the TNT using published parameters noting the initial internal energy values were not reported. The mesh size of 10 mm selected was based on a convergence study of the mid-span displacement for the panels simulated. The numerical model was also able to accurately predict the damage craters of the panel, it was noted that the concrete core in the numerical model suffered a breaching failure,

which was contained by the back face steel plates as shown in Figure 2.20. Additionally, the structural response around the slab within its one-third span was also predicted accurately. It was noted that the mid span deflections were marginally underpredicted, proving the complexity of damage prediction in contact explosions.

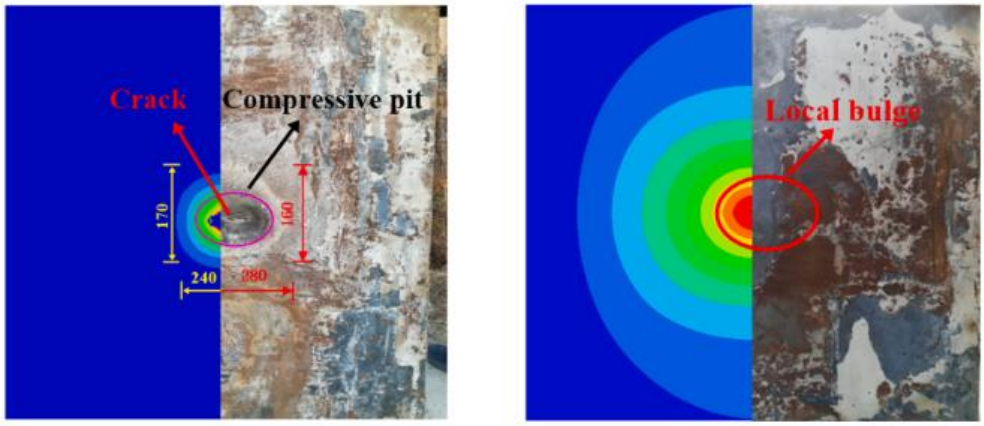

(a) front surface (b) rear surface

Figure 2.20. Comparison of failure modes of simulations against the test results (Zhao et al, 2021)

Yu et al. (2023) conducted a series of experiments to examine the response of SCC panels to close-in blast environments. The panels were subjected to a 4 kg bare cylindrical TNT charge at a scaled distance of 0.4 to 0.6 m/kg$^{1/3}$, as shown in Figure 2.21. The SCC panel consists of 2.4m x 1m 1-way spanning steel sandwich panels that were 100 mm thick and infilled with concrete to form a composite section. The steel plate was 2.5 mm thick having a yield strength of about 255 MPa. The concrete and steel interfaces of the SCC panels were connected mechanically by headed stud and tie bar connectors ensuring a composite action of the panel. The test consists of SCC panels possessing 2 different concrete cores and a conventional RC panel with steel reinforcement densities like that of the steel plates in the SCC panel, the first type consists of grade 26 normal strength concrete (NSC) tested with a standard cylinder sample and the second type consists of grade 125 ultra high-performance concrete (UHPC). The test panels were suspended horizontally across a reaction frame and the cylindrical TNT charge suspended on a tripod frame at various standoff distance above the centre of the panel. The experimental setup also consists of incident pressure gauges provided around the charge to record the blast pressure characteristics and the structural response was measured with displacement transducers at the bottom face of the panels.

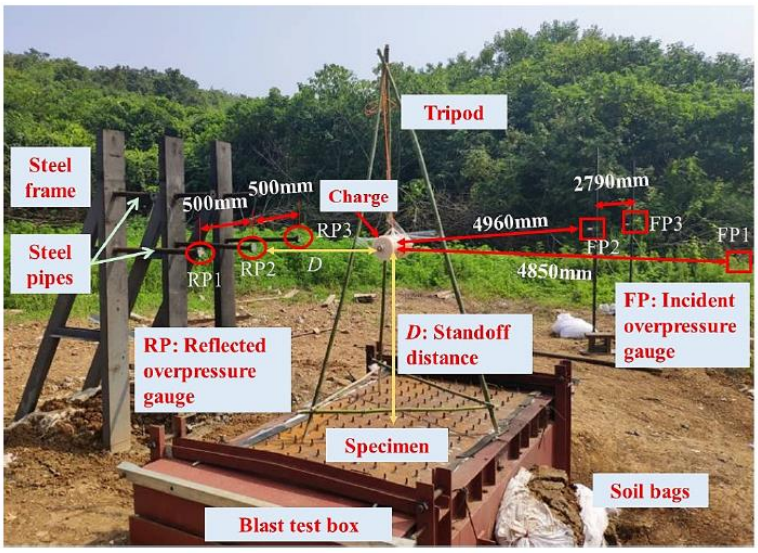

Figure 2.21. Illustration of setup of the composite panel blast test (Yu et al, 2023)

The experimental results revealed that the response of the SCC panels was primarily flexure-controlled, demonstrating the superior blast resistance of SCC panels in close-in blast loading conditions. When compared to RC panels tested at a similar scaled distance, the SCC panels showed 40% less peak deformation and 78% reduction in residual deformation. Interestingly, similar to other reported experiments by Lan et al. (2005), SCC panels that were infilled with UHPC core demonstrated enhanced shear capacity as compared to those with a NSC core, although deflections remained largely unchanged. The SCC panel using UHPC core did not reduce the peak displacement but did marginally reduce the residual displacement by about 22% from its counterpart with NSC core. With the use of interface mechanical connectors at the interface of the steel concrete sandwich panels ensuring composite action of the 2 materials, the panels mitigated plate local buckling on the top steel plate and slippage between the bottom steel plate and concrete indicating that the shear connectors worked well. Upon dissecting the panel, inclined cracks within the concrete near the support of the panel with NSC was witnessed indicating that the panel is weak in shear resistance. This was not witnessed in the panel with UHPC core which indicates the enhanced shear resistance the UHPC core is able to provide.

A validated numerical 3D model was subsequently presented using LS-DYNA constructed with a decoupled model by first determining the blast loading and subsequently applying the loading to the structure model formulated with Lagrangian elements for the structural response. The simulation of the blast generated by the

cylindrical charge was performed using a 2D axis-symmetric finite element model with a radial mesh size of 4 mm and mapped to a 3D air domain with a rectangular grid size of 10 mm immediately prior to the reflection of the blast wave on the structure. The fluid domains largely followed modelling principles as shared by past researchers. The air was modelled as an ideal gas using *MAT_NULL material model combined with linear polynomial EOS. The TNT was modelled with JWL EOS with TNT parameters from Dobratz, (1981). The TNT was filled into the Eulerian grids using *INITIAL_VOLUME_FRACTION_GEOMETRY. The concrete adopted K&C concrete model that is coupled together with the EOS *EOS_TABULATED_COMPACTION which relates the volumetric strain and bulk modulus to varying hydrostatic pressure. The model largely adopted automatically generated parameters except for the compressive and tensile softening parameters (b1 and b2) which describe the yield factor and equivalent plastic strain. These parameters would describe the post peak softening behaviour of the compressive and tensile strength curves of the concrete; hence the parameters were recalibrated using single element analysis under unconfined uniaxial loading and comparing the fracture energy with the local width. The dynamic increase factors were incorporated with models from Wu et al. (2015) for NSC and Ren et al. (2018) for UHPC. The steel plates were modelled with *MAT_PIECEWISE_LINEAR_PLASTICITY with the true stress strain curves measured. The tie bars, shear studs and rebars were modelled with bilinear plastic model using *MAT_PLASTIC_KINEMATIC. Strain rates were considered with Cowper-Symonds model with C and P values of 40 and 5, respectively, following studies from Chen et al. (2019) and Wu et al. (2022). The simulation results show good agreement with the experimental data and proved to be able to replicate the failure modes of the panels together with the crack patterns, as shown in Figure 2.22. Furthermore, they conducted a parametric study on the configuration of the panels to improve its blast resistance and reported that improving the parameters that directly affect the flexural capacity of the panel such as thickening the steel plate or increasing the depth of the panel would improve its blast performance, while decreasing the plates slenderness by providing more shear studs did little improve the bending resistance as long as the top plate in compression does not fail in local compression buckling.

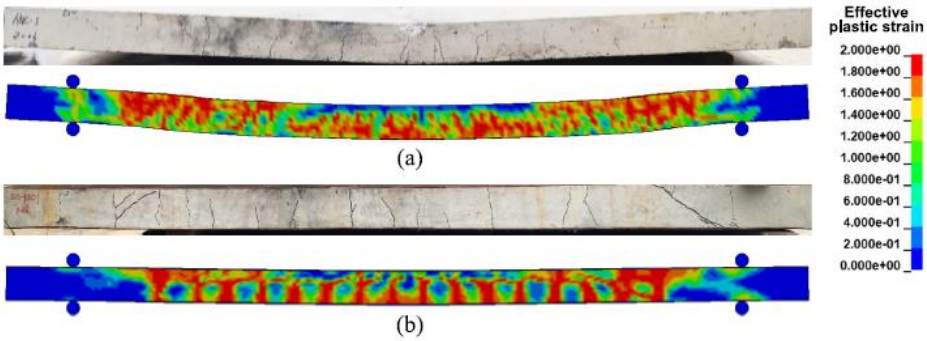

Figure 2.22. Illustration of failure modes of composite panels from simulations compared against the post-test observations (Yu et al, 2023)

Yu et al. (2023) presented a series of experiments that subjected buried straight wall circular arches that were 1.8 m tall, spanned 1.8 m with a radius of 0.9 m and a width of 1.2 m, as shown in Figure 2.23. The arch panels were constructed by a corrugated steel plates base and cast over by a concrete section with a total section thickness of 166 mm. Interface shear studs were provided to provide full composite action of the arch panels and the test adopted panels with different configuration of corrugated steel plates. The thickness of the corrugated steel plate is 2 mm with a yield strength of 235 MPa, while the concrete had a cube compressive strength of 32.5 MPa. The test panels were buried in sandy clay, the charge that comprised of cylindrical TNT with a mass of 3 kg was placed within the soil above the apex of the test panels at a scaled distance of 0.312 m/kg$^{1/3}$ to 0.624 m/kg$^{1/3}$.

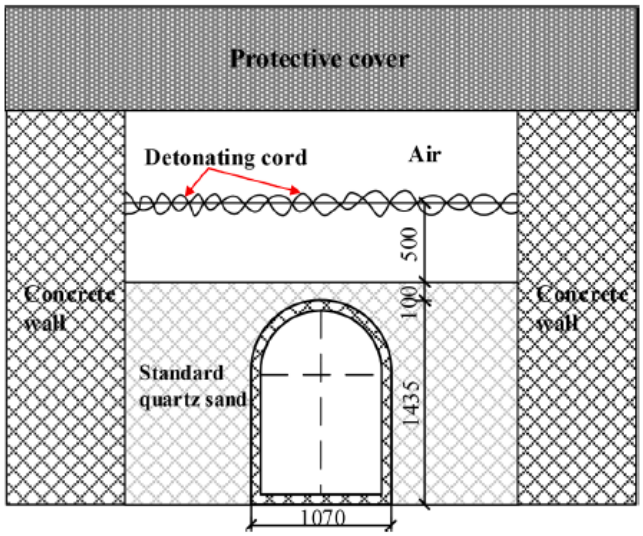

Figure 2.23. Illustration of the test setup of the buried arch Yu et al. (2023)

From the experimental tests, they reported that the corrugated steel plate backing behaved like a spall plate, successfully containing the spalled concrete preventing secondary

fragments entering the protected space. The study further highlighted the superior blast resistance of the composite panel, showcasing its ability to undergo significant elongation and plastic deformation. Under high strain-rate dynamic loading, the panel maintained both large deformation and high elasticity. The corrugated steel plate's deformation and oscillation effectively delayed the blast's impact and dissipated a significant portion of the shock wave energy. The corrugated steel plate reduced the amplitude of the tensile wave reflected reducing the extent of the spalling of the concrete.

The study of the resistance of steel composite structures to contact explosion has also peaked in interest. Yu et al. (2024) presented a series of experiments that subjected steel composite panels to contact explosive from 0.2 Kg to 1 kg bare cylindrical TNT charges as shown in Figure 2.24. The steel composite panels consist of a 2 mm thick corrugated mild steel plates with a yield strength of 243 MPa that was top up with about 116 mm of grade 30 normal strength concrete, constructed similar to a composite floor slab system. Shear studs are welded to the corrugated steel plate to provide a mechanical interlock with the concrete to mobilise a full composite action. The overall test panel is 1.2 m width and 1.5 m length with a depth of 166 mm spanning one way across a reaction frame, with the charge placed on the surface of the concrete at the middle of the panel. The panel was instrumented for displacement monitoring under the slab, acceleration and strain sensors were placed on the corrugated steel plate to measure the panel’s dynamic response.

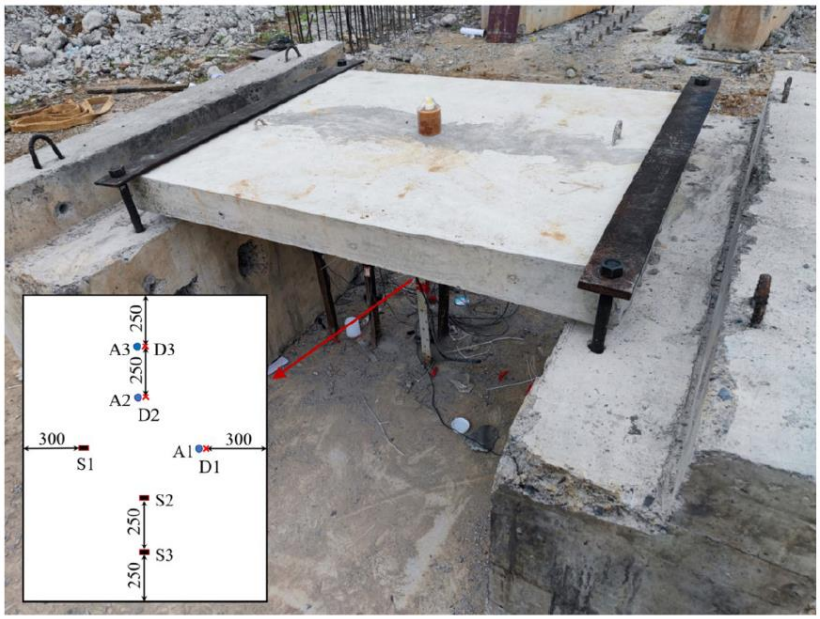

Figure 2.24. Test setup of the composite panels subjected to contact charges (Yu et al., 2024)

The experimental results show increased cratering diameter and damage of the concrete face as the charge weight is increased from 0.2 kg to 1 kg as a result of the compression of the concrete by the rapid expansion and high temperature detonation of the charge. On the sofit of the panel, when the charge was 0.2 kg, the steel plate exhibited minimal damage. The corrugated steel plate exhibited plastic deformation but no fracture when the charges were increased to 0.5 kg and 0.7 kg, maintaining a good connection with the concrete section. When the charge was increased to 1 kg, the concrete was penetrated through, and the steel plate was teared resulting in a loss of capacity of the panel. The response of the panel was mainly heavy localised damage directly under the contact charge that was accompanied by dynamic bending with the associated damage as its primary mechanism to dissipate energy. The experiments prove the overall superior performance of the corrugated steel concrete slab panel to extreme loading scenarios. They subsequently presented a validated fully coupled 3D numerical model on LS-DYNA using arbitrary Lagrange-Euler (ALE) formulations with 8 mm hexahedral mesh for the air and Lagragian formulations with 5 mm hexahedral mesh for the concrete and steel plate. The TNT was artificially filled into the mesh with keyword *INITIAL_VOLUME_FRACTION_GEOMETRY similar to technique employed by past researchers, and the coupling of the fluid structure interaction was performed using keyword *CONSTRAINTED_LAGRANGE_IN_SOLID. To optimise computational resource, the model was built with ¼ plane symmetric taking advantage of the symmetrical layout of the experiment. The concrete adopted the RHT model with some customised input parameters; the minimum damaged residual strain = 0.01 was used and the maximum principal strain erosion threshold was coupled with keyword *MAT_ADD_EROSION with an erosion criterion of 0.2 to prevent distortion of the failed mesh and premature cell deletion. The steel plate was modelled using JC model and the Gruneisen EOS while the dynamic increase factor DIF employed default strain rate term that is linear in the logarithm of the strain rate adopting a value of c = 0.017. The shear connectors and reinforcement employed a strain rate dependent elastoplastic material model *MAT_PLASTIC_KINEMATIC, with strain rate effect described by Cowper-Symonds model with C and P parameters adopting 40 and 5, respectively, similar to other published work. The air adopted similar formulations assuming an ideal gas criteria described by *MAT_NULL and the EOS by keyword *EOS_LINEAR_POLYNOMIAL. The TNT adopted similar formulations employing the

*MAT_HIGH_EXPLOSIVE with JWL EOS. The parameters used were largely similar to Dobratz (1981), with the exception of parameters B and R1, adopting customised values of 375 GPa and 4.5, respectively. The results of the numerical simulation were in good agreement with the experimental data indicating the numerical model is able to replicate the behaviour of the steel composite panel that was subjected to contact charges, as shown in Figure 2.25. Through the analysis of the simulations, they reported that the corrugated steel plate at the base of the concrete slab functioned like a scab plate, allowing energy adsorption and dispersion of the energy and reducing the magnitude of the reflected tensile stress waves on the concrete section. Due to the higher elastic wave velocity of the steel as compared to the concrete, the steel plate acts as a suppression, reducing the magnitude of the shock wave reflected off the back of the concrete. The corrugated plate also provides confinement of the spalled concrete from the rear face and hence enhances the protection from secondary fragmentation of the concrete sections. Finally, they proposed an empirical equation to quantify the damage expected on the corrugated steel concrete composite panel based on the charge weight and section thickness.

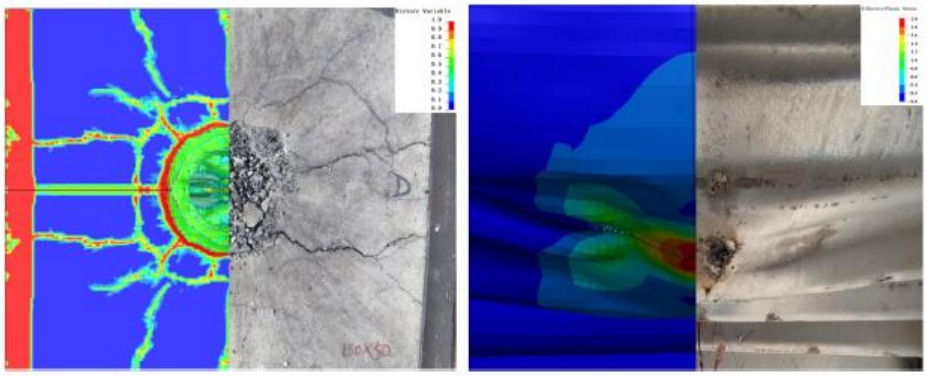

Figure 2.25. Comparison of failure modes of composite panels from simulations (Yu et al., 2024)

Zhu et al. (2024) reported on a series of experimental tests that subjected steel concrete composite slabs to contact explosives. The test panels are 1.2 m x 1 m that consist of a base mild steel plate with varying thickness of 6 mm to 8 mm built up with a 100 mm thick concrete section like a composite floor slab. The test studied the use of shear studs and prefabricated bonded ribs at the interface of the steel plate and concrete to evaluate its effectiveness to provide composite action mobilisation when subjected to contact explosives. The contact explosive consists of a cylindrical TNT with a weight of 340 g that is detonated at the centre of the slabs, as illustrated in Figure 2.26. The panel is

instrumented with displacement sensors and accelerometers at the rear of the panel. Similar to the previous study reported by Yu et al. (2024), the experimental results show that the contact charge mainly exhibited catering failure on the concrete at the surface contact with the explosive, on the rear, the steel plates provided confinement to the concrete and exhibited plastic deformation failure without any tearing or fracture of the steel plate.

Figure 2.26. Illustration of contact charge test setup (Zhu et al., 2024)

A validated 3D model was presented using LS-DYNA. The fluid sections similarly adopted ALE formulations and the structural components such as the concrete and steel sections employed Lagrangian formulations. Similar to previous studies, the coupling of the fluid structure interaction was performed using keyword *CONSTRAINT_LAGRANGE_IN_SOLID, formulations of the air similarly adopted ideal gas formulations with MAT_NULL and linear polynomial EOS. The TNT employed MAT_HIGH_EXPLOSION_BURN with JWL EOS with parameters adopted from Lee et al., (1973). The concrete employed K&C material model coupled with keyword *MAT_ADD_EROSION with an erosion failure criterion of 0.2. The steel plates were modelled with keyword *MAT_PLASTIC_KINEMATIC with strain rate effects defined by Cowper-Symonds model. The erosion criterion was provided based on the effective plastic strain of 0.2 for the steel elements. The mesh size was selected based on convergence analysis; 5 mm was used for the steel plate while a 10 mm mesh was used for the concrete sections. The results of the numerical simulation showed good agreement with the experimental data, replicating the damage modes and deflections well. Through the analysis of the numerical simulations, they reported a 2 staged failure pattern in the composite slab, the first was the propagation of the shock wave through the section right

after the detonation of the contact charge, the deformation of the concrete slab is restrained by the steel plate due to its larger compressive strength. Subsequently, the stress wave is reflected when it reaches the end of the concrete section and is reflected of the steel plate causing the interface to be separated due to the propagation of a tensile stress wave back to the concrete section. They reported that the use of prefabricated bonded ribs offered some stress wave attenuation while specimens with shear studs did not, which was reflected in the maximum deflection and acceleration recorded from the panel.

More recently, these steel concrete composite panels have also been used against underwater contact explosive scenario. Chen et al. (2024) presented on a series of experiments subjecting steel concrete composite sandwich panel to underwater contact explosion. The composite panels consist of steel sandwich panel using Q345 steel that are 5 mm thick and infilled with NSC core that is 90 mm thick. The panels adopted a 1.3 m x 1.3 m square layout that is bolted to a water- tight reaction frame by a series of bolts along the perimeter of the panel. The charges consist of charges varying from 100 g to 200 g rectangular TNT charges and 50 g cylindrical TNT charges. The reaction frame and the test panels were submerged underwater in a specialised facility and the charge was detonated at the centre of the panel as shown in Figure 2.27. The test results showed that the panels experienced significant structural deformation on both the front and back steel plates but overall maintained their structural integrity and did not suffer from any tears or cracks. The interior section of the panel was exposed using hydro jet cutting revealing a heavily damaged concrete core. The tests concluded that the steel concrete sandwich panels showed superior blast performance even in underwater scenarios where the blast loading impulse is expected significantly higher than conventional free field detonation.

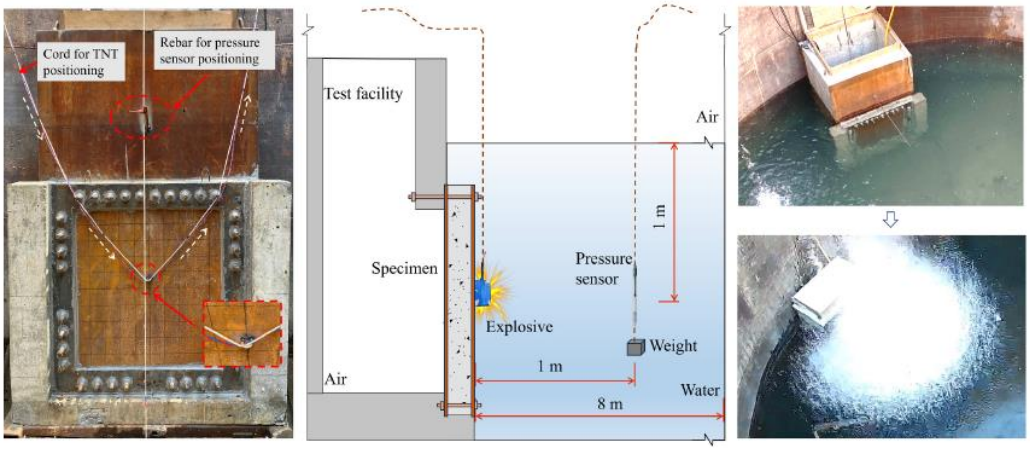

Figure 2.27. Illustration of the underwater contact charges test setup (Chen et al., 2024)

They subsequently presented a validated 3D numerical model in LS-DYNA using structured ALE formulations for the fluid and Lagrangian formulations for the steel and concrete structures. The concrete was idealised using K&C model with automatic generated parameters and DIF parameters applied from Hao et al. (2014). Keywork *MAT_ADD_EROSION was employed for numerical stability with an erosion criterion using the principal tensile strain of 0.4. The steel was idealised with *MAT_PLASTIC_KINEMATIC applied with Cowper-Symonds model using coefficients of C=6844 s-1 and p = 3.9. The water employed *MAT_NULL material with Gruneisen EOS, while the air adopted similar material and EOS assignments to published research. Similarly, the TNT employed *MAT_HIGH_EXPLOSIVE_BURN and JWL EOS parameters from Dobratz (1981). The concrete adopted a mesh size of 7.5 mm grid obtained from a mesh convergence study. The simulation results are shown in Figure 2.28. They reported that the results from the simulation matched the test data and were able to replicate the failure modes and damage patterns well. Through the numerical simulations, the damage on the panels was classified into three distinct stages, the front end of the plate suffers from local deformation owing to the shock waves generated by the contact charges. Next, the concrete core was compressed into a plastic damage phase and finally when the energy was transmitted to the back steel plate it deformed causing a global deformation of the panel with the damaged section. They also reported that the plastic damage of the concrete was the main energy dissipation mechanism in this underwater contact explosion scenario, the rear plate acted as a confinement to the concrete allowing the spalled concrete to be contained providing plastic energy dissipation of the concrete.

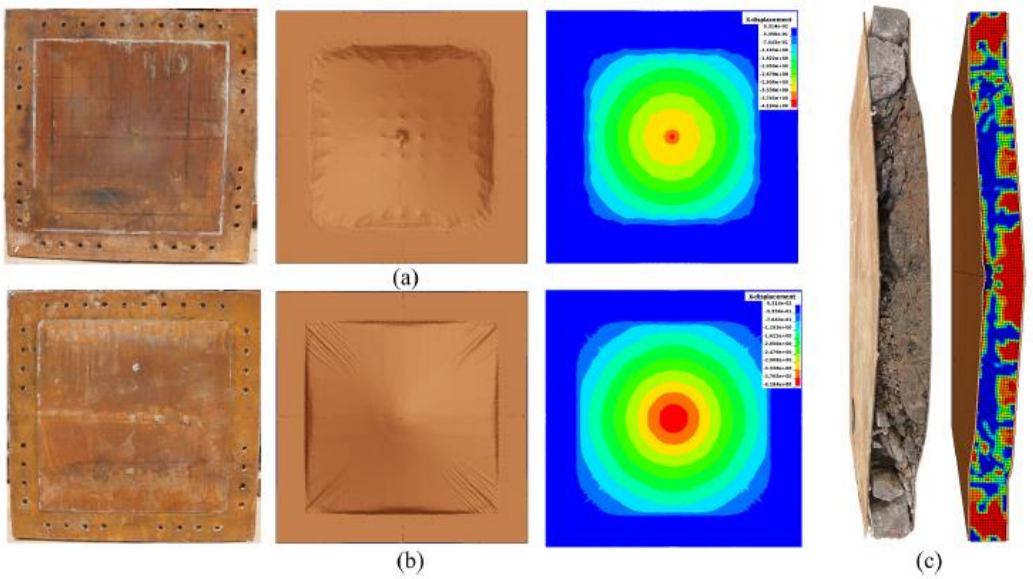

Figure 2.28. Comparison of post-test damage against simulation results (Chen et al., 2024)

Most of the numerical studies presented on the response of the steel concrete composite panels to explosive environments were performed using finite element method and with software LS-DYNA. The key numerical techniques employed to model the structural and charge materials can be summarized in Table 2.1 below. Two main material models for concrete were primarily used to simulate concrete under extreme blast and impact loading scenarios, the K&C and the RHT. Simulations involving impact and penetration of the concrete, typically adopt the RHT concrete material model, while K&C model was commonly used in blast loading environment.

Table 2.1. Summary of numerical methods used for the study of structures subjected to combined blast and fragment effects and steel composite panels to explosive effects.

Study	Panel type / Explosive loading type / Scaled distance (m/kg1/3)	Concrete Material model / Steel Material Model and DIF	Blast Load / Fragmentation Application
Leppanen (2005)	RC Blocks / 1.3Kg TNT with Ball Bearings @ Z = 0.5 to 0.86	RHT / -	ConWep based Alogrithum / Rigid Discrete Fragments
Nystrom & Gylltoft (2009)	RC wall panel / 110Kg TNT Cased Charge @ Z = 1	RHT / -	ConWep based Alogrithum / Rigid Discrete Fragments
Lan & Morrill (2016)	RC Slabs / Cased charge @ Z = 0.91 to 1.3	K&C / -	ConWep based Alogrithum / Only Loading Impulse of Fragments
Del Linz (2016)	RC Slab / 8.9Kg TNT with Ball Bearings @ Z = 1	K&C / -	ConWep based Alogrithum / Discrete Fragments with JC Material model
Del Linz (2021)	RC Slab / Cased Charge @ Z < 1.2	RHT / JC	ConWep based Alogrithum / SPH with TNT with ALE and JWL EOS
Li et al. (2020)	RC slab / 850g TNT Cased Charge @ Z = 1.69 to 3.7	RHT / JC	ConWep based Alogrithum / SPH with TNT with ALE and JWL EOS
Kang (2012)	SCC Sandwich Panels / 100 Kg TNT Bare Charge @ Z = 1.08	K&C / Nil	ConWep based Alogrithum / Nil
Khan 2019	SCC Sandwich Panels / 15kg TNT Cased Charge @ Z = 3.2	RHT / JC- Gruneisen EOS	ConWep based Alogrithum / Discrete Fragments with JC Material model
Zhao et al. (2021)	SCC Sandwich Panels / 280g TNT Contact Charges	K&C / JC-Gruneisen EOS	JWL EOS / Nil
Yu et al (2023)	SCC Sandwich panels / 4kg TNT Bare charge @ Z = 0.4 to 0.6	K&C with compaction EOS / Piecewise Linear Plasticity - Cowper-Symonds	JWL EOS Dobartz (1981) / Nil
Yu et al (2024)	Corrugated SCC panels / 0.2Kg - 1Kg TNT Contact Charges	RHT / Plastic Kinematic with Cowper-Symonds	JWL EOS Dobartz (1981) / Nil
Zhu et al. (2024)	Composite slab (single steel plate) / 0.34kg TNT Contact Charges	K&C with Erosion / Plastic Kinematic with Cowper-Symonds	JWL EOS by Lee et al., (1973) / Nil
Chen et al. (2024)	SCC sandwich panels / 50g – 0.2kg TNT Underwater Contact Charges	K&C with DIF Hao et al. (2014) / Plastic Kinematic with Cowper-Symonds	JWL EOS by Dobartz (1981) / Nil

Most studies on steel-concrete composite panels have predominantly focused on their performance under bare charge detonations, providing insights into their behaviour in such explosive environments.

2.10. Flexible Structures for Blast Protection

Increasingly, the use of flexible structures for blast resistance has been gaining popularity due to their light-weight properties and wide range of application. These structures are made of a variety of flexible materials such as liquids, polymeric porous materials, fibre fabrics and foam materials. Various composite arrangement of the materials such as sandwich, auxetic and graded structures are utilized to achieve resistance to explosive environments. Most of these flexible structures have displayed proven resistance against blast loading in small-scaled tests. For near field blast tests that generated blast and fragment loadings, the use of sandwich composite structures has been the most effective due to the flexibility to incorporate different material strengths against the fragment impact and the blast wave loading. Cai et al. (2021) performed small-scaled test subjecting multi-layered aluminium core and ultra-high molecular weight polyethylene (UHMWPE) to blast and fragment loading at Z=0.26 m/kg$^{1/3}$. The charge used 55 g TNT and preformed fragments which weighted 0.77 g each was attached to the base of the explosive to generate the fragment loading. They reported that the dominant failure modes were perforation and plugging failure in the front face plate and foam core layers. The UHMWPE failed in scorching, delamination and fibre fractures. The panels without UHMWPE experienced large deformations with petalling and cracking failure on its back face plate. The use of the UHMWPE in the bottom layer in a sandwich layout prevented petalling and cracking failure. In addition, it acts as an effective energy absorption layer reducing the back plate deformation. While the performance of the materials is validated in small scale, details such as connection failure cannot be represented, there is still a need for large scale test to further validate the performance (Zhou et al., 2023). Zhang et al. (2022) reported on a study involving corrugated sandwich panels that are filled with aluminium foam, subjected to blast and fragment loading at a scaled distance of 0.26 m/kg$^{1/3}$ to 0.78 m/kg$^{1/3}$. The charge was formed using 55 g TNT and preformed fragments which weighted 0.77 g each was attached to the base of the explosive to generate fragment loading. They reported that the foam filled panels experienced perforation failure from the fragment impact through the entire panel. The addition of the foam material in the sandwich core reduced marginally the bending deformation and perforation failure of the back face plate. They concluded that the aluminium foam was not an effective filler material to improve the resistance under blast and fragment loading.

2.11. Conclusion

The literature review identified a gap in research on SCC panels that are subjected to close-in explosive effects from cased charges below 1 m/kg$^{1/3}$ scaled distance. To address this, field blast tests were conducted on SCC panels to simultaneous blast loading and fragment impact from cased charges at 0.39 m/kg$^{1/3}$ to 0.78 m/kg$^{1/3}$ scaled distances. As part of the test program, a charge characterization test was also conducted to determine the blast overpressure and fragment loading profiles. After which, a series of numerical studies were performed using physics-based finite element analytical techniques to model the damage modes and dynamic behaviour of SCC panels that were exposed to the concurrent blast loading and fragment impact from a cased charge at a close-in detonation.

3. EXPERIMENTAL PROGRAM

3.1. Experimental test program

The test program was executed in three phases. The first phase involves characterizing the explosive environment generated from a cased charge to assess the fragment properties and the blast pressure attributes. The next phase includes conducting a scaled blast test to evaluate the dynamic behaviour of the SCC panels that are exposed to the simultaneous blast loading and fragment impact. The final phase involves quasi-static 3-point load tests to evaluate the resistance functions and residual strength functions of SCC panels under various damage conditions.

For the field blast and quasi-static load tests, five SCC panels were evaluated following the test matrix outlined in Table 3.1. In the field blast tests, there were four SCC test specimens; three of the panels were single-span slabs exposed to simultaneous blast loading and fragment impact at varying stand-off distances. The fourth panel was positioned on the ground, experiencing only fragment impact damage. The quasi-static load test was initially performed on a pristine panel acting as a control. Subsequently, the test was conducted on the third and fourth panels from the field blast tests to assess the reduction in residual resistance due to damage from the different loading conditions.

Table 3.1. Summary of the test program

Test panel	Distance from charge, R (m)	Z ($m/kg^{1/3}$)	Support conditions	Blast test loading type	Quasi-static 3-poin load test
Panel 1	1 m	0.78	Suspended	Blast and fragment loading	No
Panel 2	0.75 m	0.58	Suspended	Blast and fragment loading	No
Panel 3	0.5 m	0.39	Suspended	Blast and fragment loading	Yes
Panel 4	0.5 m	0.39	Non-suspended (Panel placed on ground)	Fragment damage only	Yes
Panel 5	Nil	Nil	Nil	Nil	Yes

The SCC panels consist of the assembly of a 1 m x 2.2 m steel box panel as shown in Figure 3.1. This was done by first arranging four equally spaced U-channel beams in parallel and subsequently enclosing by four 3 mm thick steel plates, forming the top, bottom, and two end plates to create a fully enclosed structure. 3 mm thick fillet welds were used to frame the steel plates to the U-channels. To join the top plate to the beams

forming a closed box, 22 evenly spaced slotted holes (each approximately 50 mm long and 15 mm wide) were cut on the plate over the stiffener beams, allowing for external welding. Before securing the end plate, concrete was filled into each panel section to form the concrete core. Once set, the end plate was welded on externally to the steel frame, completing the SCC panel assembly.

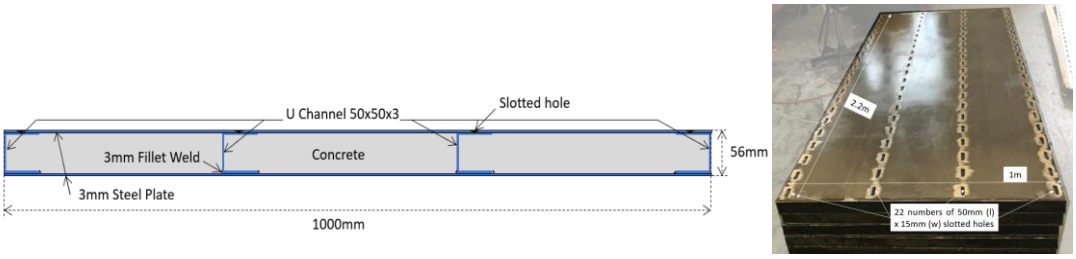

Figure 3.1. Schematic of SCC panel (left) and photo of SCC panel (right).

The concrete core used C35/45 concrete specified to EN 206-1 and designed to Eurocode 2 standards. Standard cube tests were performed on the same batch of concrete that was used for filling the SCC panels. The average cube strength tested was 45 MPa, corresponding to a cylindrical strength estimated at 35 MPa. S355 structural steel was used for the SCC panels' steel plates that had a lab tested yield strength of 378 MPa, while the channel beams were made of S235 structural steel. The Young's modulus for concrete and steel components was determined based on Eurocodes 2 and 3, respectively (CEN, 2010). Table 3.2 provides a summary of the material properties.

Table 3.2. Summary of properties for panel members

Member	Material characteristic Strength	Young's Modulus, E
S355 Steel Plates	fy = 378 MPa	200 GPa
S235 U Channel	fy = 235 MPa	200 GPa
C35/45 Concrete	fck = 35 MPa	34 GPa

3.1.1. Phase 1 Field Tests

3.1.1.1. Characterization Test Setup

Plastic explosive Sprängdeg m/46 (86% PETN and 14% mineral oil) with mass of 1.83 kg was used for the charge. The mass was equivalent to a TNT charge weighing 2.12 kg, based on a TNT conversion factor of 1.16 which was reported by Elfving (1995). A 2.81 kg cylindrical hollow steel tube with a predrilled hole for the detonation of the charge at its centre was used for casing the charge. The cylinder used 4 mm thick mild steel, with a length of 600 mm and external diameter of 58 mm. To achieve uniform fragmentation upon detonation, the steel casing was pre-scored internally. Around the circumference of the case, 19 distinct diamond patterns were cut, while 35 sections were cut along its

longitudinal axis. Hence, during fragmentation of the case, alternate rows yielding 35 fragments and 34 fragments + 2 half fragments are expected. The details of the scoring pattern of the steel cylinder are shown in Figure 3.2. Two characterization tests were conducted to examine fragment characteristics and blast pressure. The charge was set above the ground in an instrumented arena test configuration as shown in Figure 3.3. Pencil probe-type pressure sensors were setup at the same elevation of the charge and placed 2.075 m and 3.060 m away to record incident overpressures generated. A steel plate in a form of an approximate 50 x 50mm angle section was provided between the charge and sensors to function as a shielding plate against fragment impact.

Furthermore, witness plates and high-speed cameras were instrumented to record the speed of the fragments as shown in Figure 3.4. Witness plates were positioned at 3 m from the charge, coupled with video analytics, the time of detonation and the first fragment perforation through the witness plates would be recorded facilitating the calculation of the fragment's average velocity over 3 m. Lastly, to characterize the mass of the fragments produced, soft recovery devices in a form of water tanks were provided for fragment collection.

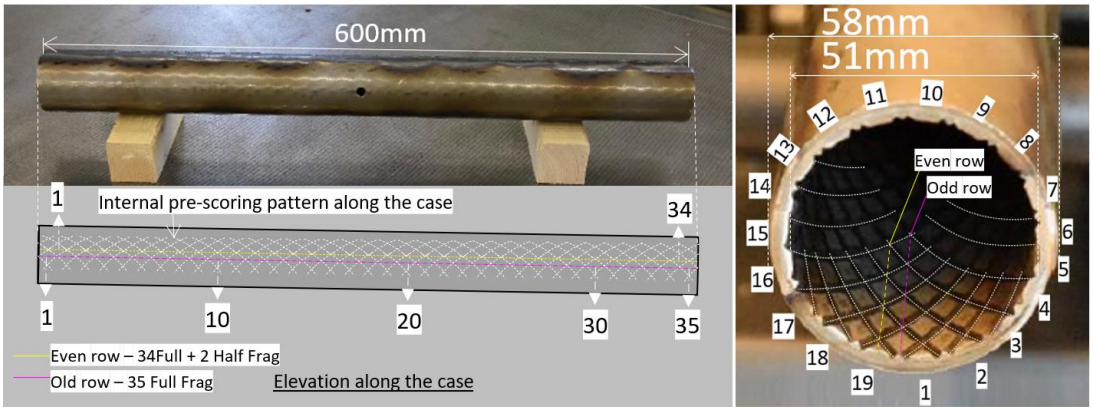

Figure 3.2. Illustration of scoring patterns on case (left) and on the internal of the case(right)

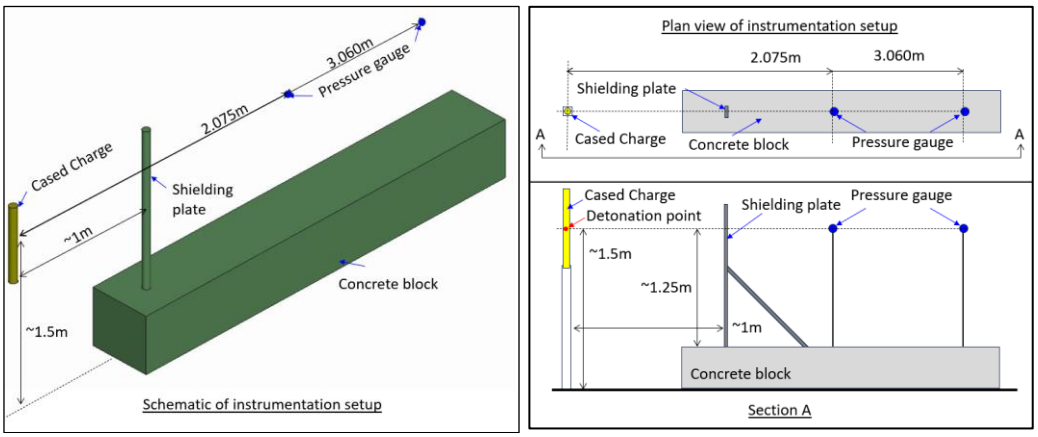

Figure 3.3. Diagram of the pressure gauges instrumentation setup

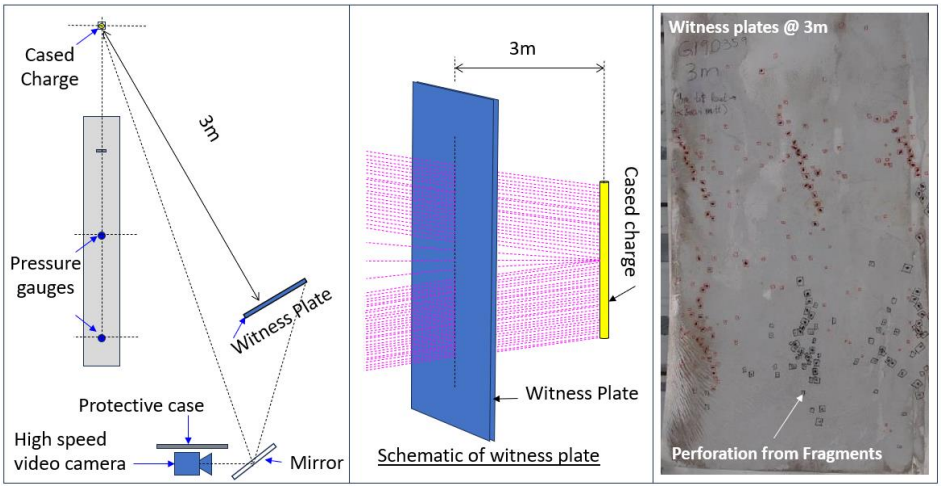

Figure 3.4. Diagram of the witness plate setup

3.1.1.2. Charge Characterization Results

The test results for the fragment characterisation are presented in Table 3.3. The recovered fragments had an average mass of 2.177 g and an average equivalent diameter of 8.1 mm the fragments recovered had with a low standard deviation of 0.076 g indicating the success of producing uniform fragments. Analysis of the video from the cameras revealed that the quickest fragment launched had an average velocity of 1667 m/s that was recorded over 3 m. The pressure gauge recordings from the tests are presented in Figure 3.5, Figure 3.6 and summarized in Table 3.4. Pressure gauge measurements were compared with incident pressure calculations from ConWep (Hyde, 1992), which calculates blast pressure based on the semi-empirical methods proposed by Kingery and Bulmash (1984), with the TNT charge weight of 2.12 kg. The calculated pressures from ConWep were approximately 35% lower than from the experimental tests, likely due to the use of a slender cylindrical charge in the experiment as compared to the spherical charge assumption used in ConWep, which is consistent with findings by Knock & Davies (2013). Additionally, the TNT conversion factor that was adopted from Elfving (1995) was derived based on impulse measurements and hence may have contributed to these discrepancies.

Comparing the impulse, the calculated impulse from ConWep was up to 30% higher than the measured impulse, this is likely due to the casing effects as energy is used to fracture the case and accelerate the fragments during the detonation of a cased charge, resulting in a lower blast impulse, aligning with observations by Nyström (2013).

Table 3.3. Fragment characteristics summary

Average velocity recorded, (m/s)	Average Mass recorded (g)	Standard deviation of mass of fragments recorded (g)
1667	2.177	0.076

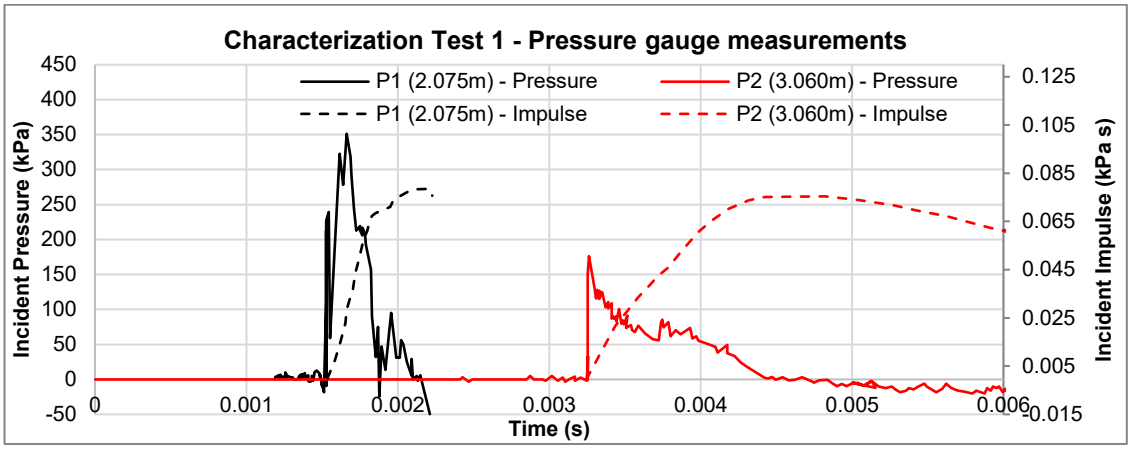

Figure 3.5. Pressure gauge results from Characterization test 1

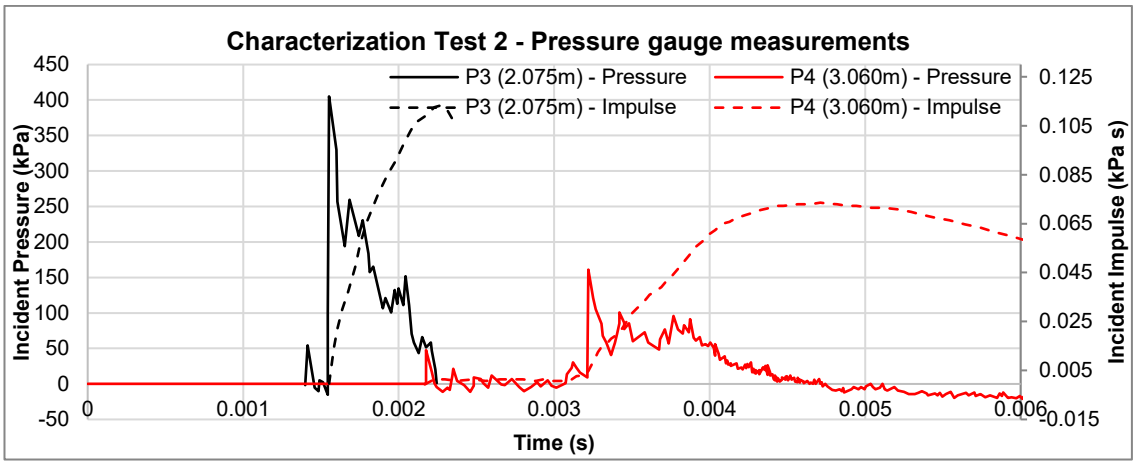

Figure 3.6. Pressure gauge results from Characterization test 2

Table 3.4. Summary of results from the characterization tests

	Guage @ 2.075m			Guage @ 3.06		
	ConWep	Test 1	Test 2	ConWep	Test 1	Test 2
Arrival time (ms)	1.681	1.532 (-9%)	1.536 (-9%)	3.424	3.258 (-5%)	3.204 (-6%)
Incident blast pressure (kPa)	315	350 (+11%)	410 (+30%)	132	177 (+34%)	162 (+23%)
Incident blast Impulse (Pa×s)	144	79* (-45%)	113 (-22%)	101	75.6 (-25%)	73.1 (-28%)

*Error in instrumentation

(% difference to ConWep)

3.1.2. Phase 2 – Field Blast Tests

3.1.2.1. Test Setup

The field blast test consists of SCC panels that are setup in a suspended form and non-suspended form described previously in Table 3.1 is illustrated in Figure 3.7. Panels 1 to 3 spanned 2 m and were supported on simple joints consisting of steel roller bars along their short edges. The charge was set vertically above the panels, with a standoff distance (R) from 1 m to 0.5 m (Z = 0.78 m/kg$^{1/3}$ and 0.39 m/kg$^{1/3}$). To investigate the dynamic flexural response of the panels, five equally spaced laser gauges were positioned beneath the centre of the panel. Additionally, the surface of the panel had metallic foils sheets that are electrically conducted when punctured, used to record the arrival time of the incident blast wave or detect fragment when pierced whichever arrives first. These sheets consist of 2 metallic foils that was separated by a middle non-conducting layer that forms a closed-circuit electrical signal when torn or punctured.

Test Panel 4 investigated the damage from high-velocity fragment impact to the panel's residual capacity. The panel was rest flushed on a concrete pavement to eliminate flexural response with the charge suspended at 0.5 m above the panel. To simulate the maximum damage, the panel's mid-span was targeted with the maximum fragment density. As the detonation point is in the middle of the cylinder, two clusters of fragments diverging symmetrically from its centre is produced upon detonation. The charge was offset such that one cluster of fragments would impact the centre of the panel, while steel plates shielded the remaining panel.

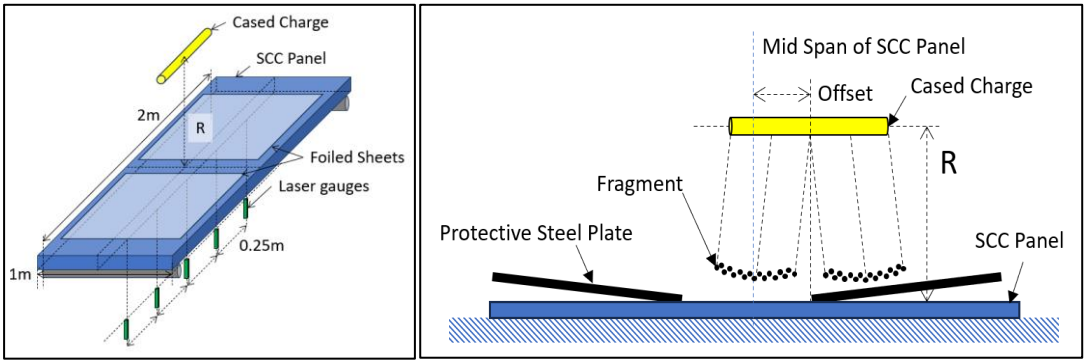

Figure 3.7. Suspended panel setup for blast tests (left) and not suspended panel setup (right)

3.1.2.2. Field Blast Test Results

Images of the post-test panels are shown in Figure 3.8 and Figure 3.9. The recorded deflections at the middle of the three panels from the laser gauges are illustrated in Figure 3.10 and the maximum values with their corresponding time are summarized in Table 3.5.

As the panels were not restrained on the support, there was noticeable post-test movements of the panel due to the rebound forces. The original location of the panel could not be established and hence the final permanent mid-span deformations were not measured.

All three panels exhibited an almost linear response for the initial 2.5 msec, with the magnitude and slope of the response increasing with a smaller stand-off distance. This suggests a shear plugging phase, likely caused by the shock wave from the reflected blast pressure and fragment impact into the restrained concrete core. This behaviour aligns with findings from Del Linz (2021), who performed numerical studies investigating the dynamic response behaviour of RC structures that were exposed simultaneously to blast loading and fragment impact. Subsequently, with the damage sustained, the structure continued to deform dynamically. There was a significant increase in the maximum deflection at mid-span when the stand-off of the charge was reduced. When Z was reduced from 0.78 m/kg$^{1/3}$ to 0.58 m/kg$^{1/3}$, the resultant deformation experienced a 30% increased while a further reduction to 0.39 m/kg$^{1/3}$ resulted in 155% increase, reaching 153 mm. This deflection corresponded to a maximum rotation of approximately 9 degrees, approaching the 12 degrees failure criterion for steel plated structures that is outlined in UFC-3-340-02. Comparing the structural periods which can be interpreted from the time which the maximum deflection occurs, the period was similar for tests at 0.78 m/kg$^{1/3}$ and 0.58 m/kg$^{1/3}$. However, when the stand-off was reduced to Z=0.39 m/kg$^{1/3}$, the period nearly doubled to 21 ms. This suggests a significant alteration in the panel's natural frequency, likely due to increased fragment density and resulting damage. Further investigations are required to fully understand these effects.

Despite experiencing significant deformation, the panels retained their structural integrity. Apart from localized compression buckling of the top and side plates, the panels primarily exhibited a flexural failure mode, demonstrating their effectiveness against the extreme loading. The panel's bottom plate developed a distinct fold across its entire mid-span, indicating the formation of a plastic hinge. Inspection of the rear face of Panel 3 revealed a relatively uniform and smooth steel surface, with no visible localized bulging or plugging failure, suggesting that localized damage did not significantly affect the overall structural response. The severity of localized plate buckling on the top steel plates varied across the tests and generally increased with panel deflection. Panel 1 exhibited minor localized bulging of the steel plates, indicating plate buckling and partial

delamination from the concrete infill. Panel 2 displayed similar behaviour, but with more pronounced bulging. The deformed shape of the delaminated plates in both Panels 1 and 2 followed a smooth, curved profile with no sharp kinks. In contrast, Panel 3's top plate exhibited a distinct pitch at mid-span, indicating not only localized compression buckling but also plastic hinge formation in the delaminated plate. Since no mechanical connectors were used at the steel-concrete interface, compressive in-plane axial forces in the top steel plate led to buckling under flexural bending. Due to the large deformation, sections of the plates tore along their welded connections to the U-channels.

The recorded arrival times of the blast wave, determined through the closed-circuit initiation of the foil sheets, were compared with expected arrival times predicted by ConWep. At standoff distances of 0.75 m and 1 m (Z = 0.78 m/kg$^{1/3}$ to 0.58 m/kg$^{1/3}$) the measured and predicted times were closely aligned, with discrepancies of approximately 1%. However, at the closer standoff distance of 0.5 m (Z = 0.39 m/kg$^{1/3}$), the difference increased to about 30%. This growing disparity at smaller scaled distances can likely be attributed to the shape effect of the cylindrical charge, which deviates from the spherical charge assumption used in ConWep calculations. The recorded time of arrival values is summarized in Table 3.6.

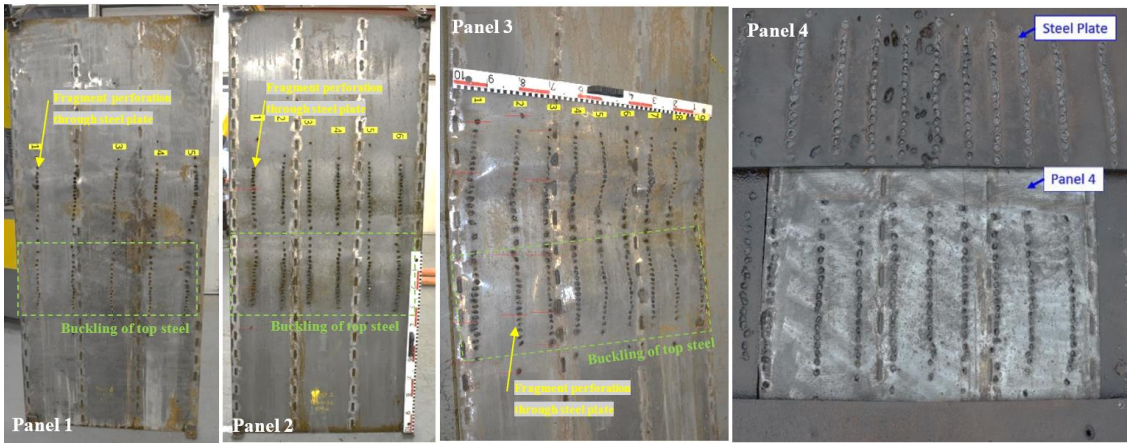

Figure 3.8. Post-test images of the front impact surface of Panel 1 (left), Panel 2 (middle left), Panel 3 (middle right) and Panel 4 (right)

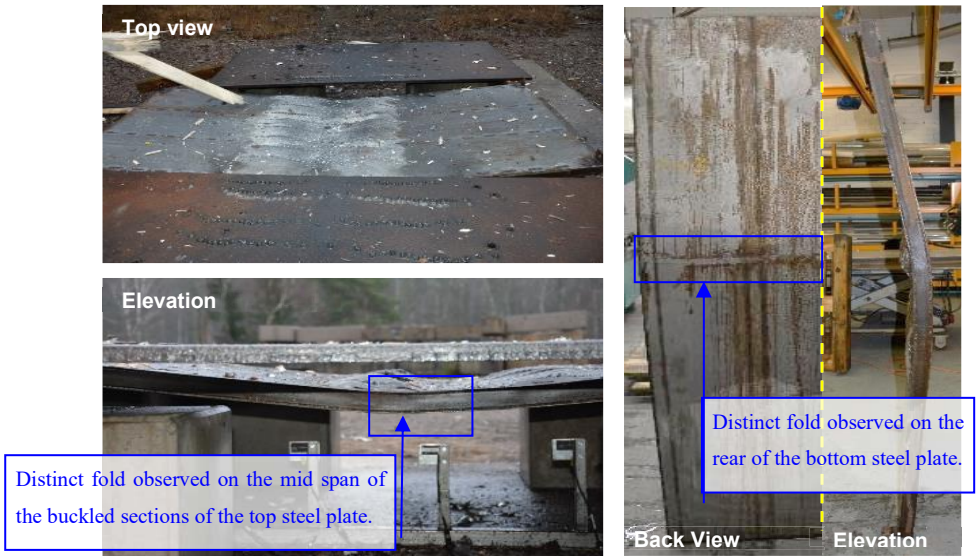

Figure 3.9. Post-test photo of Panel 3 top view (top left), elevation view (Bottom left), back view and corresponding elevation view (right)

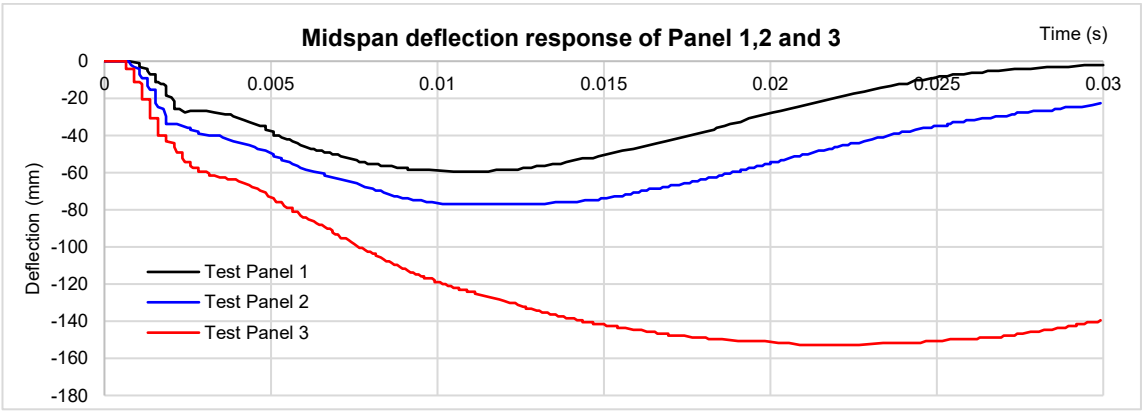

Figure 3.10. Results of midspan deflection response from field blast tests

Table 3.5. Summary of the structural response from the test panels

Test panel	Distance from charge, R (m)	Z ($m/kg^{1/3}$)	Measured mid-span deflection (mm)	Max end support rotation (deg)	Time at max deflection (msec)
1	1m	Z = 0.78	60	3.4	11
2	0.75m	Z = 0.58	78	4.5	11
3	0.5m	Z = 0.39	153	8.7	21

Table 3.6. Summary of measured time of arrival of blast wave

Test panel	Distance from charge, R (m)	Z ($m/kg^{1/3}$)	Measured time of arrival (msec)		Average time of arrival (msec)	ConWep, Time of arrival (msec)
			Foil 1	Foil 2		
1	1m	Z = 0.78	0.416	0.436	0.426	0.430 (-0.9%)
2	0.75m	Z = 0.58	0.284	0.292	0.288	0.257 (12.1%)

3	0.5m	Z = 0.39	0.172	0.168	0.170	0.131 (29.8%)

(% Difference compared to field blast tests)

Fragment impacts on the test panels perforated the top steel plate and penetration into the concrete core; however, none of the fragments fully perforated any of the panels in all tests. Distinctive holes formed by individual fragment penetrations were observed on the top steel plate, allowing for an accurate count of all fragments. Due to the pre-scoring of the casing, the fragments struck the test panels in well-defined rows. Panels 1, 2, and 3 were impacted by 5, 6, and 9 rows of fragments, respectively, corresponding to the pre-score patterns around the casing's circumference. Each row contained either 35 or 36 fragments (34 full fragments and 2 half fragments), consistent with the pre-scoring pattern along the longitudinal axis of the charge, as detailed in Section 3.1.1.1. Panel 4, designed to assess fragment-induced damage, was impacted by 9 rows of fragment clusters at its mid-span as intended. Despite fragment penetration into the concrete core, neither the top steel plate nor the overall SCC panel exhibited visible deformation, indicating that blast effects were successfully mitigated. In all tests, fragments from each row were fully accounted for through post-test inspection of puncture counts on the test panels. The overview of the total mass and total number of fragments that impacted each panel is summarized in Table 3.7. The fragment throw trajectory along the longitudinal axis was distinctly clustered into two symmetrical groups centred around the detonation point, creating a region where fragment impacts were sporadic. The average fragment throw distance (l_f), on the panel was determined based on the measured distance from the first to the last fragment along each row, the average spacing between adjacent fragment rows (l_{ar}) and the resultant fragment density which is defined as the total mass of fragments impacting the panel divided by the fragment impact zone, as illustrated in Figure 3.11, are presented in Table 3.8.

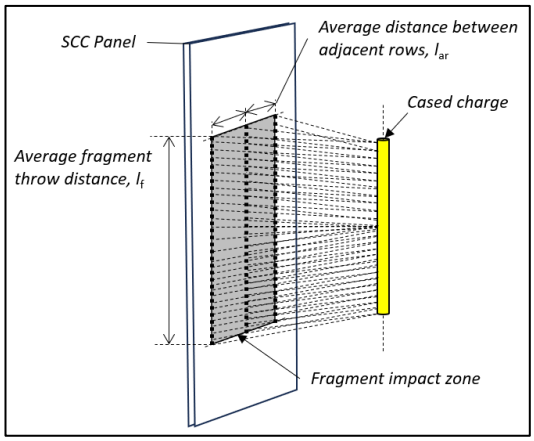

Figure 3.11. Illustration of fragment impact measurements

Table 3.7. Total mass and number of fragments which impacted the panel

Test panel	Distance from charge, R (m)	Z (m/kg$^{1/3}$)	Number of rows	Number of fragments impacting panel	Total mass of fragments (g)
1	1m	Z = 0.78	5	177	381
2	0.75m	Z = 0.58	6	213	457
3	0.5m	Z = 0.39	9	319	685
4	0.5m	Z = 0.39	9	166	343
5	Nil	Nil	Nil	Nil	Nil

Table 3.8. Summary of the fragment impact pattern and mass density

Test panel	Distance from charge, R (m)	Z (m/kg$^{1/3}$)	l_f (m)	l_{ar} (m)	Fragment mass Density (kg/m^2)
1	1m	Z = 0.78	0.868	0.198	0.55
2	0.75m	Z = 0.58	0.807	0.149	0.76
3	0.5m	Z = 0.39	0.725	0.105	1.12

To assess the extent of concrete damage in the panels, the top plate of the panel was cut open to expose the damaged concrete core. In regions of concentrated fragment impact, large craters were observed, with adjacent concrete becoming loose upon physical disturbance. The removal of these loose concrete chunks allowed for an estimation of the maximum penetration depth, though the disturbance caused by the removal process limited precise measurement.

In Panel 1, some fragments reached the bottom steel plate but did not dent the rear steel plate, indicating that they had fully perforated the concrete but lost sufficient energy before reaching the steel plate. A similar observation was made for Panel 2, where most fragments reached the bottom steel plate without denting it, confirming full perforation through the concrete core. In both cases, perforation was concentrated in regions along the fragment rows with the highest impact density.

Crater formations from multiple fragment impacts merged along the rows, forming an extended crater along the penetration path. This effect was more pronounced in Panel 2,

where the fragment rows were positioned closer together, leading to the merging of craters from two adjacent rows into a single expanded spalled surface. Despite the significant penetration and cratering, no fragments fully perforated through any of the test panels. Panel 3 retained for the quasi-static test and therefore not opened to examine the concrete damage, nevertheless, inspection of the rear face of Panel 3 revealed a relatively uniform and smooth steel surface, with no visible localized bulging or indentations, suggesting that the fragments did not have much energy after penetrating the concrete section. The estimated maximum penetration depth for each panel is presented in Table 3.9. The exposed concrete core from Panels 1 and 2 is illustrated in Figure 3.12 and Figure 3.13, respectively. The steel-concrete composite panels demonstrated strong performance, maintaining structural integrity despite sustaining significant damage from high-density fragment impact and extreme deformation under a close-in cased charge explosion.

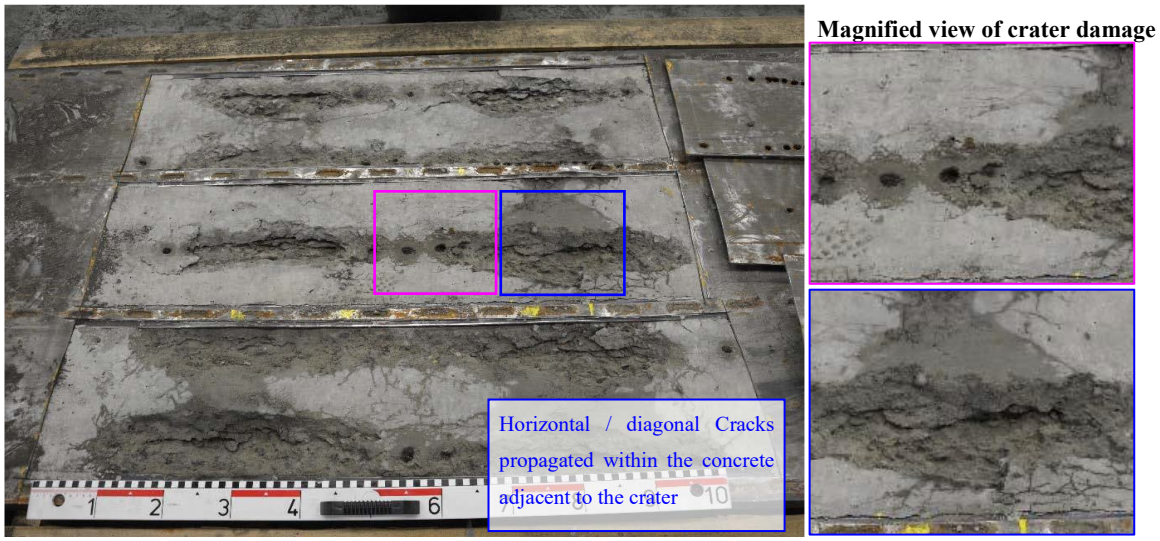

Figure 3.12. Photo of exposed concrete from Panel 1

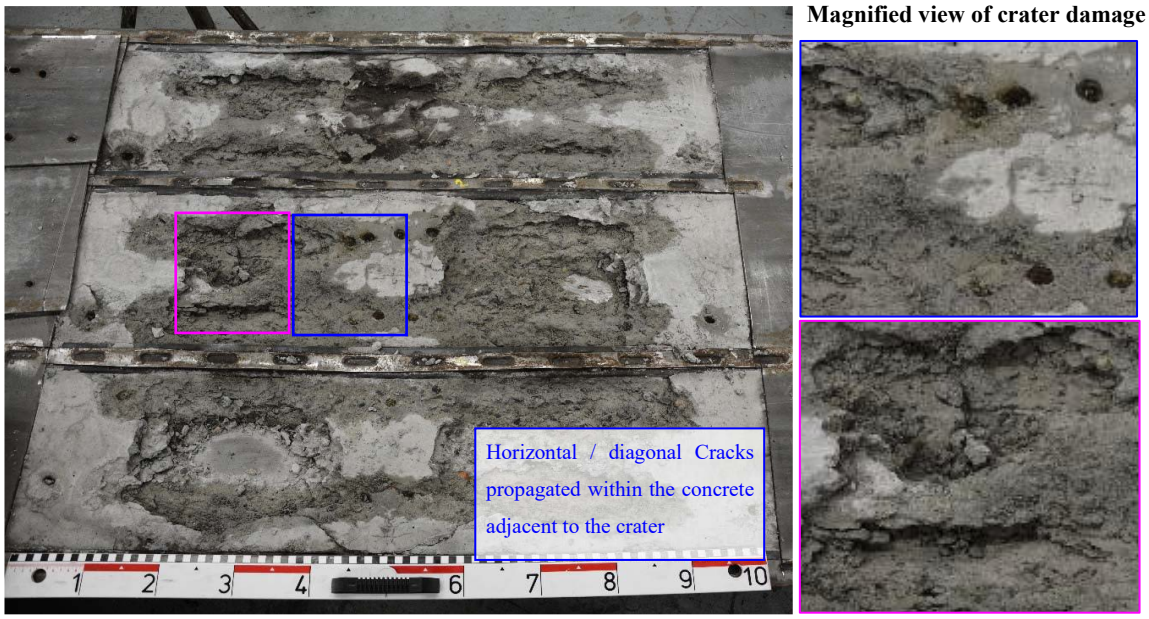

Figure 3.13. Photo of exposed concrete from Panel 2

Table 3.9. Summary of the maximum penetration depth from test panels

Test panel	Distance from charge, R (m) / Z (m/kg$^{1/3}$)	Estimated maximum penetration depth (mm)	Remarks
1	1m (Z = 0.78)	~53	Some fragments reached the rear steel plate without denting it
2	0.75m (Z = 0.58)	~53	Multiple fragments reached the rear steel plate without denting it
3	0.5m (Z = 0.39)	Not inspected	No visible dents or holes in the outer face of the rear steel plate

3.1.3. Phase 3 – Quasi-Static Point Load Tests

3.1.3.1. Test Setup

The quasi-static three-point loading test utilized a hydraulic displacement-controlled system, powered by an external pump driving the hydraulic piston. The panels were simply supported on rollers spaced 2000 mm apart, with the load applied at midspan across the full panel width using a 100 mm wide steel beam. To ensure even load distribution and minimize stress concentrations, a fibreboard sheet matching the beam's dimensions was placed between the beam and the panel. The details of the quasi-static test setup and fibreboard interface are illustrated in Figure 3.14.

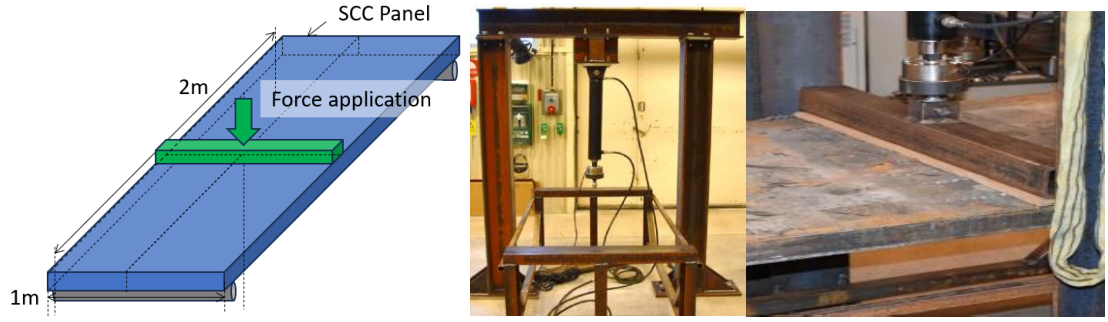

Figure 3.14. Illustration of the quasi-static load test (left), photo of hydraulic displacement system (centre) and load application through a steel beam and fibreboard strip (right)

3.1.3.2. Quasi-Static Test Results

The load-displacement curves of the panels exhibited an initial linear increase, indicating an elastic response. This was followed by a hardening phase characterized by a curvilinear displacement response, reaching a peak at the ultimate load. Subsequently, the panels entered a softening phase, where they sustained a consistent load over significant displacement before failure, demonstrating their ductility and toughness. The results of the quasi-static load test are presented in Figure 3.15. The maximum load and equivalent elastic stiffness (measured at approximately 70% of the maximum load) are summarized in Table 3.10. A comparative analysis between Panel 5 (pristine) and Panel 4 (fragment-damaged) revealed a 32% reduction in the maximum load and a 9% decrease in stiffness, indicating significant structural degradation due to high-velocity fragment impact. The reduction in strength and stiffness is likely attributed to the firstly, puncturing of the steel plates from multiple fragment impacts, compromising the top plate's structural integrity and increasing its susceptibility to local buckling once stresses exceeded the elastic regime. Secondly, the damage to the concrete core reduced its load-bearing capacity and stiffness.

Interestingly, Panel 4 exhibited failure at 220 mm displacement, as compared to 149 mm for the pristine panel, suggesting that the fragment-damaged panel retained a prolonged plastic phase. Similar findings have been reported by Nordström & Forsén (1970) and Grisaro et al. (2017), where fragment-damaged reinforced concrete slabs demonstrated higher ductility than their undamaged counterparts. Nordström & Forsén (1970) hypothesized that cracking from fragment damage facilitated strain distribution in the reinforcement at multiple locations rather than concentrating stress solely beneath the applied load. Likewise, in Test Panel 4, fragment-induced damage to the top steel plate and concrete core likely resulted in an asymmetric stress distribution under static loading. Instead of stress concentration at the midspan, stress was spread over a larger area across

the panel's span during the three-point bending test, enhancing its ability to absorb energy and undergo greater deformation. Panel 3, which experienced simultaneous blast and fragment loading in the field test, retained remarkable residual capacity despite sustaining damage and extreme deformation. Its maximum load capacity and stiffness were approximately half that of the pristine panel, further demonstrating the SCC panel's resilience and ability to maintain structural integrity under extreme conditions.

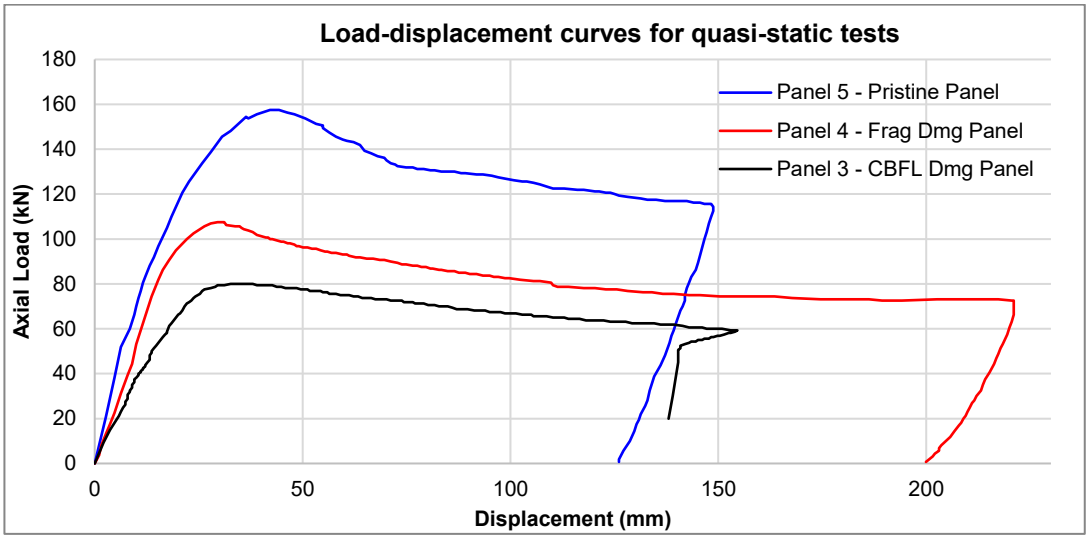

Figure 3.15. Load displacement curves results for test Panels 3, 4 and 5.

Table 3.10. Max load of the various articles from quasi static tests

Test article	Max load (kN)	Reduction from Pristine	Experiment Stiffness (kN/mm)	Reduction from Pristine
Panel 5: Pristine	157.4	-	5.88	-
Panel 4: Fragment damage	107.6	-32%	5.36	-9%
Panel 3: Combined blast and fragment loading	79.9	-49%	3.29	-44%

3.2. Evaluation of Experimental Results

This section presents the evaluation of experimental results from all phases of the test program.

3.2.1. Evaluation of Phase 1 Experimental Results

The evaluation of the charge characterization tests focuses on the fragment velocity.

3.2.1.1. Fragment Velocity Analysis

The fragment velocity measurements from the experiment were evaluated by comparing the experimentally measured average velocity with the calculated average velocity. The calculated velocity was determined as the average of the initial velocity of the fragment upon leaving the charge and the striking velocity at the witness panel.

The initial fragment velocity was estimated using Gurney's (1943) equations for a cylindrical case, based on an equivalent TNT charge of 2.12 kg. The striking velocity was determined using equations from UFC 3-340-02 (DOD, 2008), which account for the velocity decay due to air resistance. Gurney's equation for uniform cylindrical case is presented in Equation (3.1), where V_0 is the initial fragment velocity (m/s), $\sqrt{2E_G}$ is the Gurney Energy constant = 2438 m/s for TNT charges, C is the mass of high explosive (kg) and M_c is mass of casing (kg).

$$V_0 = \sqrt{2E_G} \cdot \sqrt{\frac{C/M_c}{1+\frac{1}{2}C/M_c}} \tag{3.1}$$

The resultant striking velocity from UFC 3-340-02 is presented in Equation (3.2), where V_s is the striking velocity, α= 0.004 oz$^{1/3}$/ft for primary random mild steel fragments, R is the distance from centre of detonation = 9.84 ft and W_f is the fragment weight = 0.0768 oz (equivalent to 2.1 g).

$$\frac{V_s}{V_0} = e^{-\alpha\frac{R}{{W_f}^{1/3}}} \tag{3.2}$$

The calculated velocities are summarized in Table 3.11. The results indicate that the adopted methodology provided an accurate prediction of the average fragment velocities, with discrepancies of less than 4%.

Table 3.11. Summary of fragment velocity from characterization test

C (kg)	Calculated V_0 (m/s)	Calculated V_S (m/s)	Calculated average velocity, (m/s)	Experimental average velocity	Difference from Experimental velocity
2.12kg	1803	1643	1723	1667	3.4%

The estimated time of arrival of the fragments was compared to the blast wave arrival times from both the field blast tests and charge characterization tests, as presented in Table 3.12. At close-in scaled distances, the blast wave is expected to reach the panel before the fragments, aligning with findings from Nystrom (2009). Additionally, the time difference between the blast wave and fragment impact is minimal, approximately 0.1 msec, indicating that the fragments strike during the decay phase of the blast wave. However, at greater stand-off distances exceeding 1.6 m/kg$^{1/3}$, as observed in the charge characterization tests, fragments are expected to arrive before the blast wave. In such cases, structural damage from fragment impact must be considered before analysing blast effects. The results further show that as the scaled distance increases, the time difference between fragment and blast wave arrival also increases.

Table 3.12. Summary of time of arrival analysis between the fragments and blast wave

Test	Distance from charge, R (m) / Z (m/kg$^{1/3}$)	Experimental arrival time of incident blast wave (msec)	Calculated arrival time of fragment (msec)	Arrival time difference between the blast wave and fragments (msec)
Charge Characterization Tests 1 and 2	3.060m (Z = 2.38)	3.231*	1.74	-1.49
	2.075m (Z = 1.61)	1.534*	1.14	-0.394
Blast Test Panel 1	1m (Z = 0.78)	0.426	0.563	0.137
Blast Test Panel 2	0.75m (Z = 0.58)	0.288	0.421	0.133
Blast Test Panel 3	0.5m (Z = 0.39)	0.170	0.279	0.109

*Average experimental results

3.2.2. Evaluation of Phase 2 Field Blast Test Results

The evaluation of the field blast test results focuses on the fragment penetration and impact patterns.

3.2.2.1. Fragment Perforation Analysis

The observed damage on the exposed panels (Panels 1 and 2) was compared to penetration analysis conducted using UFC 3-340-02. In multilayered structure penetration

analysis, it is generally assumed that there is no interaction between different material layers, and each layer's penetration behaviour is evaluated independently. The fragment's trajectory is tracked through each layer, determining whether it perforates the material. If perforation occurs, the fragment exits with a residual velocity, which then serves as the striking velocity for the subsequent layer (Krauthammer, 2008). The UFC 3-340-02 (DOD, 2008) manual provides a standardized bullet shape for primary fragments with a cylindrical portion with diameter *d* (in) and a hemispherical portion with radius *r* (in), as illustrated in Figure 3.16. The diameter *d* is calculated from the calibre density from Equation (3.3), where W_f is the fragment weight (oz).

$$d = \left(\frac{W_f}{2.976}\right)^{\frac{1}{3}} \tag{3.3}$$

The penetration depth of standard primary mild steel fragments into mild steel plates X_s (in) is calculated from Equation (3.4), where V_s is the striking velocity (kfps).

$$X_s = 0.21 {W_f}^{0.33} {V_s}^{1.22} \tag{3.4}$$

The residual velocity of the fragment after perforation of steel plate V_{rs} is calculated from Equation (3.5), where V_x is the critical perforation velocity; *t* is the thickness of the steel plate (in). The critical perforation velocity V_x is obtained by equating the depth of penetration X_s to the thickness of the steel plate t_s in Equation (3.4), the corresponding value of the striking velocity is the critical perforation velocity.

$$V_{rs} = V_s[1 - (\frac{V_x}{V_s})^2]^{\frac{1}{2}}/(1 + \frac{t_s}{d}) \tag{3.5}$$

In the analysis of fragment penetration into the concrete layer, the residual velocity of the fragment after passing through the preceding steel layer V_{rs} is considered as the striking velocity on the concrete layer V_{sc}. The first step is to determine whether the fragment perforates the given section thickness. If the analysis confirms that the section is sufficient to stop the fragment (i.e., no perforation), the penetration depth is calculated under the assumption of a massive concrete slab. However, if the fragment is expected to perforate the concrete layer, its residual velocity is computed and used for the analysis of subsequent layers. The depth of penetration into concrete X_f is calculated from Equation (3.7), where X'_f is the penetration depth from an armor piercing fragment that is calculated from Equation (3.6a) or Equation (3.6b) and f'_c is the concrete compressive strength (psi).

For $X'_f < 2d$

$$X'_f = 1.92 \times 10^{-3} {W_f}^{0.37} {V_{sc}}^{0.9} \tag{3.6a}$$

For $X'_f > 2d$

$$X'_f = 1.32 \times 10^{-6} W_f^{0.4} V_{sc}^{1.8} + 0.695 W_f^{0.33} \quad (3.6b)$$

$$X_f = 0.7 X'_f \left(\frac{4000}{f'_c}\right)^{1/2} \quad (3.7)$$

The thickness of concrete required against perforation is calculated from Equation (3.8), where t_{pf} is the thickness of concrete required against perforation.

$$t_{pf} = 1.13 X_f d^{0.1} + 1.311 d \quad (3.8)$$

The residual velocity of the fragment after it perforates the concrete section V_{rc} is calculated from Equation (3.9a) or Equation (3.9b), where t_c is the thickness of the concrete. The process of calculating the penetration on the bottom plate as required is repeated with Equation (3.5) by treating the residual velocity from the concrete as the striking velocity on the steel plate.

For $X_f < 2d$

$$V_{rc} = V_{sc}\left[1 - \left(\frac{t_c}{t_{pf}}\right)^2\right]^{0.555} \quad (3.9a)$$

For $X_f > 2d$

$$V_{rc} = V_{sc}\left[1 - \left(\frac{t_c}{t_{pf}}\right)\right]^{0.555} \quad (3.9b)$$

The results of the fragment penetration analysis are presented in Table 3.13. There is a significant discrepancy between the measured and calculated fragment penetration depths. Most notably, the individual fragment analysis did not predict perforation through the concrete section, despite consistent observations of such perforation in the post-test inspections of Panels 1 and 2. This discrepancy highlights the synergistic effect of multiple fragment impacts, which amplifies the damage potential on concrete beyond what is predicted by single-fragment models.

Additionally, the results highlight the advantage of having the rear steel plate that confines the concrete core. Theoretically, if a fragment perforates the concrete, it should retain a substantial residual velocity, potentially causing penetration damage to the rear steel plate. However, test results showed that while fragments reached the rear plate, they did not cause any visible denting, regardless of the scaled distance. This suggests that the perforated concrete, when confined by the rear steel plate, retains significant residual capacity to resist further fragment penetration.

Table 3.13. Summary of maximum penetration depth from test panels

Test panel	Maximum experimental penetration depth (mm)	Calculated X_f (mm)	Calculated T_{pf} of the concrete section (mm)
1,2	53	32.0	40.3mm < 50mm

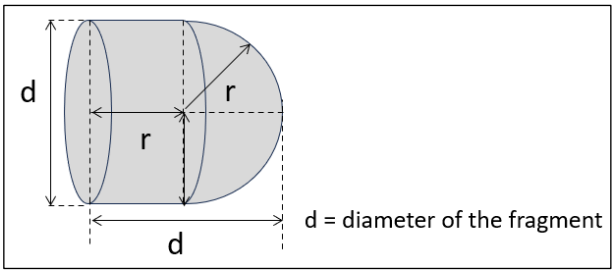

Figure 3.16. Shape of standard primary fragments

3.2.2.2. Fragment Impact Pattern Analysis

When the cylindrical charge is detonated at its centre along the longitudinal axis, the resulting explosion propels fragments outward from each half of the casing, launching them away from the detonation point. The trajectory of the fragment launch along the charge is described geometrically by Taylor's angle θ (Taylor, 1941), presented in Equation (3.10), where D is the detonation velocity = 7680 m/s for m/46 plastic explosive (Helte et al., 2006) and V_0 is the initial velocity of the fragment = 1803 m/s.

$$Sin\ \theta = \frac{V_0}{2D} \tag{3.10}$$

The fragment throw distance along the longitudinal axis of the charge l_f is calculated by Equation (3.11), where l_c is the length of the case, R is the distance between the charge and the panel.

$$l_f = l_c + 2R \tan\theta \tag{3.11}$$

Across the charge section, the pre-scoring of the casing influences the fragment launch pattern. With the case scored at 19 sections around its circumference, the separation angle between adjacent odd and even fragment rows were calculated to be approximately 9.47 degrees from the centre of the charge, as illustrated in Figure 3.17. Based on the separation angle, the average distance between the adjacent rows of fragment impact l_{ar} is calculated in Equation (3.12) where N_{frg} is the number of rows of fragment impacted on the panel.

$$l_{ar} = \tan\left(\frac{9.47*(N_{frg}-1)}{2}\right) * R * 2 \,/\, (N_{frg}-1) \tag{3.12}$$

For a generic cased charge, the total mass of fragments impacting the panel is derived using a geometric line-of-sight assumption, extending from the centre of the casing to the

edge of the panel (Grisaro et al., 2018), as shown in Figure 3.17. The angle of incidence ($\theta'/2$) from the centre of the casing to the edge of the panel is calculated in Equation (3.13) where B is the width of the panel. The total fragment mass M_f is calculated in Equation (3.14) where M_C is the mass of casing.

$$\frac{\theta'}{2} = tan^{-1}\frac{\frac{B}{2}}{R} \tag{3.13}$$

$$M_f = \frac{\left(\frac{\theta'}{2}\right)}{\pi} M_C \tag{3.14}$$

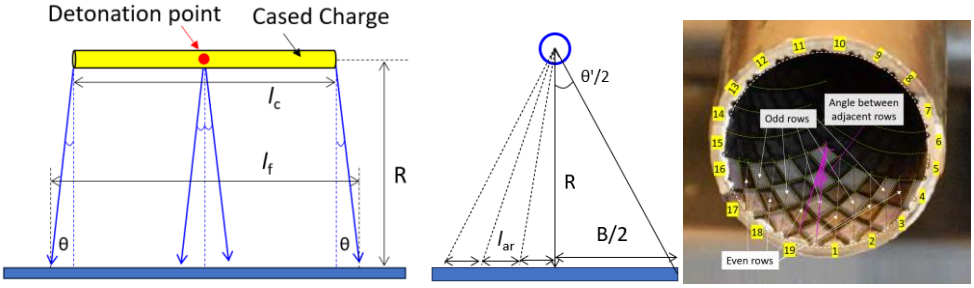

Figure 3.17. Illustration of geometrical approach for fragment mass calculation

The results of the fragment throw analysis and fragment impact mass analysis are presented in

Table 3.14 and Table 3.15, respectively. It is noted that the proposed approach for quantifying the fragment throw distance and the distances between fragment rows yields results within 1% and 14%, respectively, of the experimental values. This indicates that the proposed geometrical method estimates the total fragment mass impacting the SCC panels with an accuracy of within 13% of the experimental values.

Table 3.14. Summary of fragment impact pattern analysis

Test pane l	Experimenta l l_f (m)	Calculated l_f (m)	Difference	Experimenta l l_{ar} (m)	Calculated l_{ar} (m)	Difference
1	0.868	0.836	-3.7%	0.198	0.172	-13.6%
2	0.807	0.777	-3.7%	0.149	0.132	-11.7%
3	0.725	0.718	-1.0%	0.105	0.097	-7.7%

Table 3.15. Summary of fragment mass analysis

Test panel	Calculated Fragment mass (g)	Experimental Fragment mass (g)	Difference
1	415	381	8.9%
2	526	457	15.0%
3	703	685	2.4%

3.2.3. Evaluation of Phase 3 Quasi-Static Point Load Test Results

The flexural behaviour of the SCC panel was calculated and compared to quasi-static test results from the pristine panels. The section analysis was performed using an equivalent section approach based on McKinley and Boswell (2002), which assumes: 1) the section remains plane under bending, and 2) concrete below the neutral axis is assumed to have cracked and thus has no tensile strength. The idealization of the equivalent section and stress block for the SCC, used in the elastic section analysis, is shown in Figure 3.18.

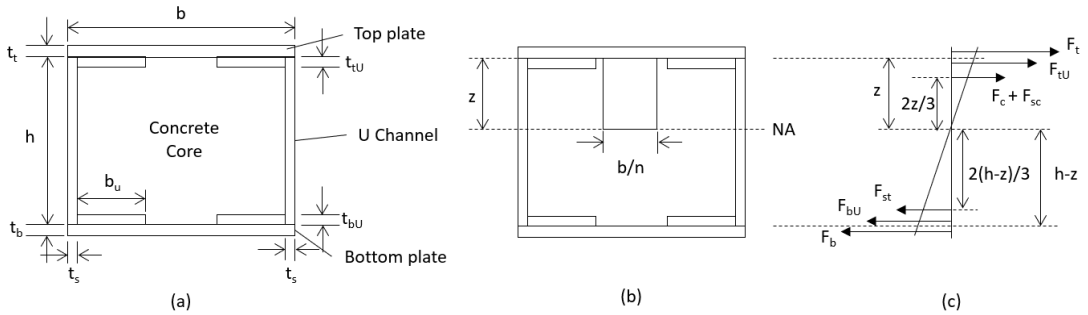

Figure 3.18. Schematic of (a) section of panel, (b) idealised equivalent section and (c) idealization of stresses for SCC Panel

The position of the neutral axis can be determined using traditional reinforced concrete theories, with modifications to account for changes in geometry. To derive the elastic moments, it is assumed that the stress in the side plates varies linearly across the elastic neutral axis. The elastic moment capacity is calculated by coupling the forces about at the compressive force generated from the concrete section and side plates (F_C+F_{SC}) as presented in Equation (3.15), where f_t is the stress in the top plate, f_{tU} is the stress in the top plate from the U channel, f_{st} is the stress in the side plate from the U channel, f_b is the stress in the bottom plate, f_{bU} is the stress in the bottom plate from the U channel and z is the neutral axis of the section.

$$M_{el} = f_t b t_t \left(\frac{z}{3} + \frac{t_t}{2}\right) + f_{tU} 2 b_U t_{tU} \left(\frac{z}{3} - \frac{t_{tU}}{2}\right) + 0.5 f_{st} 2 t_s (h - z) \frac{2h}{3} + f_b b t_b \left(h - \frac{z}{3} + \frac{t_b}{2}\right) + f_{bU} 2 b_U t_{bU} (h - \frac{z}{3} - \frac{t_{bU}}{2}) \quad (3.15)$$

The section analysis of the panels adopts a similar approach to concrete design of beams that are under-reinforced (McKinley and Boswell, 2002) such that the bottom plate would yield first ($f_b = f_y$), where f_y is the yield stress in the bottom plate, and the tensile stress in the top plate at yield f_t can be derived from f_y. It is assumed that the maximum tensile stress in the side plate has the same magnitude as the stress in the bottom plate

($f_{st} = f_b = f_t$), hence, the section's elastic moment can be translated in Equation (3.16), where and f_{yU} is the yield stress in the U channel's bottom plate.

$$M_{el} = f_y(\frac{2z+t_t}{2h-2z+t_b})bt_t\left(\frac{z}{3}+\frac{t_t}{2}\right) + f_{yU}(\frac{2z-t_{tU}}{2h-2z-t_{bU}})2b_U t_{tU}\left(\frac{z}{3}-\frac{t_{tU}}{2}\right) +$$

$$0.5f_{yU}2t_s(h-z)\frac{2h}{3} + f_y bt_b\left(h-\frac{z}{3}+\frac{t_b}{2}\right) + f_{yU}2b_U t_{bU}(h-\frac{z}{3}-\frac{t_{bU}}{2}) \quad (3.16)$$

The plastic section analysis adopts methodology by Kang (2012), when the section is loaded further, the section will respond plastically, and the neutral axis will rise closer to the top plate reducing the concrete's strength contribution to the moment capacity until it becomes negligible when the neutral axis reaches the top plate. Without consideration of the concrete core, the section's plastic moment can be described by Equation (3.17).

$$M_{pl} = f_y bt_t\left(\frac{t_t}{2}+\frac{h}{2}\right) + f_y 2t_s\frac{h^2}{4} + f_y bt_b(\frac{t_b}{2}+\frac{h}{2}) \quad (3.17)$$

The maximum load capacity of the panel is calculated based on the ultimate strength, f_u of the respective steel grades and corresponding ultimate strain, ε_u from Eurocode 3 (CEN, 2009). The calculated section behaviour is presented in Table 3.16 and superimposed with the load displacement curves in Figure 3.19. The comparison of the elastic stiffness and ultimate load is summarized in Table 3.17.

The test results from Panel 5 (pristine) and the analytical section analysis indicated that the load curves reached both the elastic and plastic yield loads as predicted. The elastic stiffness was closely matched to the measured initial stiffness, with a difference of only 15%. Around the analytical plastic yield point, the panel transitioned from a hardening phase to the eventual attainment of maximum load. It was observed that the predicted plastic limits were generally lower as compared to the experimental results, indicating that the methodology is conservative. Comparing the calculated maximum load values which is derived based on the ultimate strength and strain with the experimental results, the resistance curve of the panel beyond the plastic capacity is quite different and shows the limitations of the use of the analytical solution to represent the SCC panels beyond its plastic capacities.

The analytical solution predicted a steady increase of the load beyond plastic capacity to a max loading of 175kN with a corresponding deflection of 107mm calculated based on the ultimate strain. While the experimental test showed the panel achieved a maximum load of 157kN shortly after plastic capacity was reached at a deflection of about 44mm. Following the peak load in the experiment, the panel softened and maintained its strength through the plastic phase until failure occurred at a displacement of approximately 149

mm. The softening behaviour witnessed in the experimental test is likely caused by local compression buckling of the top steel plates. While the failure deflection in the experiment is larger and hence more conservative than that predicted by the analytical model, it is recommended that the plastic strength is used instead of the ultimate strength in the analytical representation of the SCC panel.

Analysing the resistance curve beyond the plastic phase of the panel, the average ultimate load was calculated by taking the weighted average from the elastic yield load (around 21 mm displacement) to the failure load at the final displacement of 149 mm. Despite a gradual decay in load during the plastic phase, the average ultimate load was approximately 2% higher than the plastic point loads calculated. It can be concluded that the proposed section analysis methodology is appropriate to estimate the section's elastic and plastic capacities.

However, it should be noted that the methodology proposed is applicable only for SCC panels without any interface connectors between the steel and concrete sections like the panels tested in the experiment.

Table 3.16. Calculated section properties of SCC panel

Section Properties	
Elastic moment capacity, M_{el} (kNm)	62
Elastic Point Load at Midspan, P_{el} (kN)	123
Elastic displacement at midspan, Δ_{el} (mm)	18.2
Elastic Stiffness (kN/mm)	6.79
Plastic moment capacity, M_{pl} (kNm)	65
Plastic Point Load at Midspan, P_{pl} (kN)	130
Plastic displacement at midspan, Δ_{pl} (mm)	21.6
Maximum (ultimate) Load, P_u (kN)	175
Displacement at midspan at maximum load, Δ_u (mm)	107.4

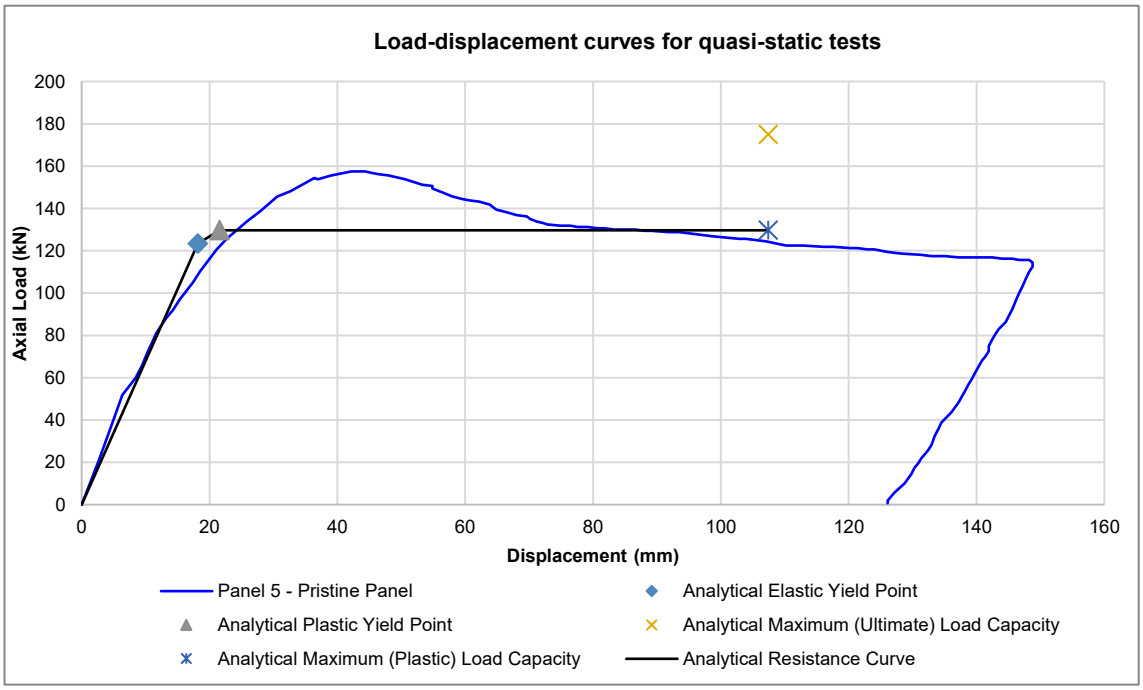

Figure 3.19. Results of load displacement resistance and analytical solutions for Panel 5.

Table 3.17. Summary of key parameters between analytical and experimental data

	Panel 5 – Pristine Panel	Analytical solution	Difference
Maximum load (kN)	157	175	11%
Elastic Stiffness (kN/mm)	5.88	6.79	15%
Average ultimate load (kN)	133	130 (Plastic point load)	2%

The flexural capacity of the damaged panels was not analysed due to the failure of panel driven by local compression buckling of the top plates that were punctured by the multiple fragment impacts, compromising the top plate's structural integrity and increasing its susceptibility to local buckling once stresses exceeded the elastic regime. As such, the fundamental assumption from McKinley and Boswell (2002), that the section remains plane under bending is not valid and an improved methodology is recommended to be studied to appropriately quantify the panel resistance with the damage by the fragments.

3.3. Summary

The behaviour of steel-concrete composite (SCC) panels subjected to concurrent blast and fragments loading was explored to assess its synergistic loading effects of on the structural response at close-in scaled distances. An experimental program which

comprised 3 phases; 1) charge characterization tests, 2) field blast tests, and 3) quasi-static tests, was conducted to meet this objective. The experimental results were quantified analytically and the findings based on these experimental studies can be summarised as follows:

1. The experimental results from the field blast test exhibited significant structural deformation of the panels. Post-test analysis revealed that the panels were not only damaged by the blast wave, but remarkable damage was caused by the high-density fragment penetration. Despite significant damage to the concrete core and the extreme deformation experienced, the steel concrete composite panels maintained their structural integrity and proved their performance in explosive environments generated from cased charges at close-in standoff distances.
2. The experimental results from the field blast test exhibited significant increase in the deflection when the scaled distance from the cased charge reduced. This was evident at scaled distance 0.39m/kg$^{1/3}$ where the longer structural response time indicated that the natural frequency of the panel was altered by the damage in the panel. Additionally, the residual capacity derived from quasi-static load tests exhibited remarkable reduction in the panel's section capacity due to the fragment damage. This indicated the significance of the synergistic effects from the simultaneous loading from blast and fragments at close-in scaled distance from cased charges, which would need to be studied further.
3. The results from quasi-static test on the SCC panels indicated that there was stiffness and strength degradation on the SCC panels that were damaged owing to the blast and fragment impact at close-in scaled ranges. The primary failure occurred through compressive buckling failure at the top steel plates, mainly due to the lack of interface connectors between the steel plates and concrete infill, causing delamination of the steel plates rendering it more susceptible to local buckling failure once stresses went beyond elastic regime.
4. The results from the fragment impact patterns and mass analysis were quantified well by analytical methods. However, the results from the penetration analysis from a single fragment as compared to multiple simultaneous fragment impact in the experiment was significantly different. Most notably, the concrete was not expected to perforate in a single fragment analysis, however, in the experiment fragments were found at the face of the rear steel plate indicating the concrete

section was perforated. In addition, the craters from multiple fragment impact merged to form a large crater. The damage of concrete from the multiple fragment impact needs to be studied further.

The findings of this study are limited to steel concrete composite panels subjected to cased explosive charges at close-in loading regimes at the closest stand-off distance of $0.39 m/kg^{1/3}$, with maximum fragment density of $1.12 kg/m^2$ and maximum single fragment mass of 2.1g. Since the mass of the fragments were pre-defined through pre-scoring of the case, alternative case configurations could be performed in future studies to understand the impact of heavier fragment clusters on the response on these steel concrete composite panels

4. NUMERICAL STUDIES

This section presents a numerical study conducted using physics-based finite element analysis to model the damage modes and dynamic behaviour of SCC panels exposed to concurrent blast loading and fragment impact from a cased charge at close-in detonation distances, based on the experimental results reported. The post-blast quasi-static test was not studied due to the large computational resource required to simulate the coupled model to an adequate response time for the panel to come to a rest.

4.1. Numerical Simulations for Charge Characterization Test

When a cased charge is detonated, energy is lost due to casing effects, which result from the fragmentation of the casing and the subsequent launching of fragments (Nyström, 2013). A common approach to quantify the resulting blast parameters, accounting for the energy loss, is to relate them to the blast effects generated by a bare charge using an equivalent bare charge mass (C_{EB}) (Crowley, 2006). To characterize the blast loading from a cased charge, numerical simulations were performed using formulations that applied Multi-Material Arbitrary Lagrangian-Eulerian (MM-ALE) methods on LS-DYNA. A 2D axisymmetric Eulerian mesh, consisting of a fixed air domain filled with the cylindrical TNT charge, was employed. The model utilized a 3 m x 4 m 2D axisymmetric plane mesh to replicate the charge characterization tests, as shown in Figure 4.1. The axisymmetric plane was defined along the longitudinal axis at the centre of the cylindrical charge. The bottom edge of the model was set as a reflecting boundary, located 1.25 m below the geometric centre of the cased charge, corresponding to the top of the concrete block in the experimental setup. The other two edges were assigned non-reflecting boundaries, representing the air interfaces. Pressure gauges were positioned at 2.075 m and 3.060 m from the charge, consistent with the experimental tests, to record the incident blast pressures. The TNT charge was incorporated into the air mesh using the *INITIAL_VOLUME_FRACTION_GEOMETRY keyword, applied to the corresponding MM-ALE regions.

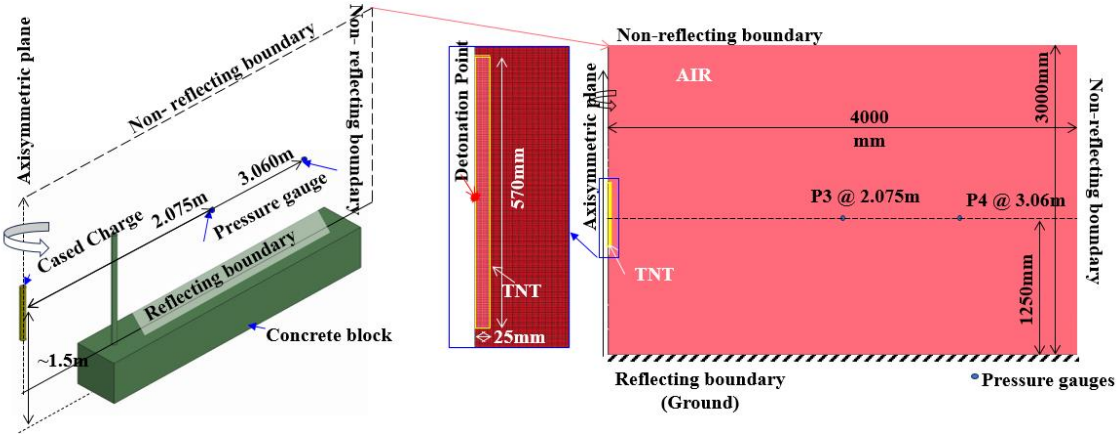

Figure 4.1. Setup of 2D axisymmetric model of the TNT cylinder charge

The ideal gas equation of state (EOS) is adopted to model the air. The relation between air density, pressure and internal energy is presented in Equation (4.1):

$$P = (\gamma - 1)\frac{\rho}{\rho_0}E \tag{4.1}$$

where P, ρ, E and γ are the pressure, density, internal energy per unit mass and adiabatic index (γ = 1.4 for air). The EOS for TNT charge was taken according to the Jones-Wilkens-Lee (JWL) equations defines pressure is presented in Equation (4.2):

$$P = A\left(1 - \frac{\omega}{R_1 V}\right)e^{-R_1 V} + B\left(1 - \frac{\omega}{R_2 V}\right)e^{-R_2 V} + \frac{\omega E}{V'} \tag{4.2}$$

where P is the pressure, A, B, E0, R1, R2 and ω are empirical constants by Dobratz (1981) were used as a baseline, presented in Table 4.1.

Table 4.1. Summary of JWL Parameters

JWL Parameter	A (GPa)	B (GPa)	R_1	R_2	ω	E_0 (GPa)
	371.25	3.231	4.15	0.95	0.30	7.0

A mesh sensitivity analysis was conducted to identify the optimal mesh size for the simulation. Uniform mesh sizes of 1 mm, 2 mm, and 5 mm were tested, corresponding to 25, 12, and 5 elements across the radius of the charge, respectively. The incident pressure and impulse at distances of 0.5 m and 1 m from the charge are shown in Figure 4.2, with the analysis results presented in Table 4.2. The peak pressure and impulse results for the 2 smallest meshes (1 and 2 mm) differed by less than 5%, while the 5 mm mesh showed a greater discrepancy, exceeding 5%. Based on this, the 2 mm mesh size was deemed sufficiently accurate and was selected for subsequent simulations. The final model used a mesh size of 2 mm, resulting in 3 million elements.

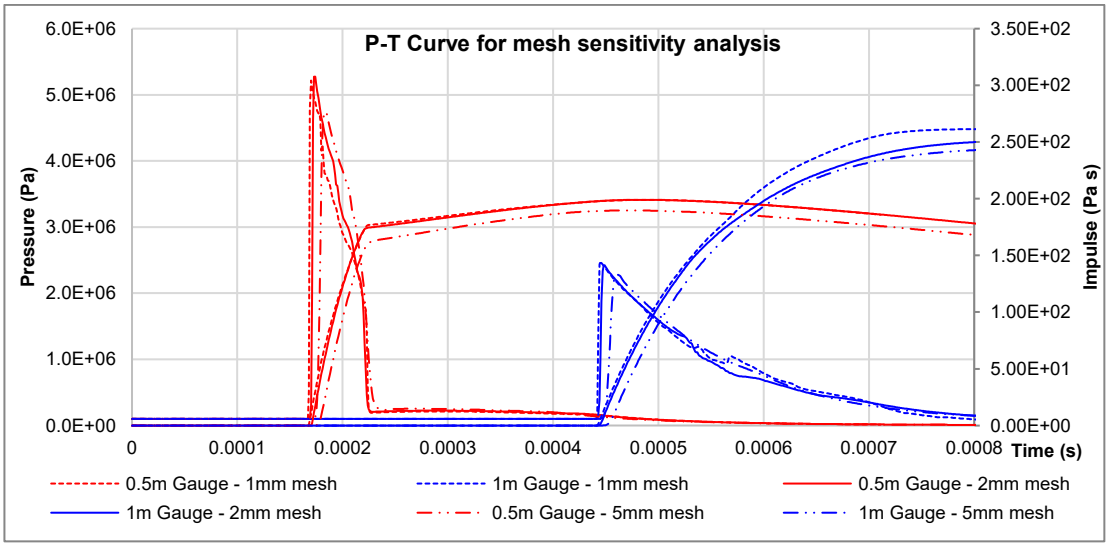

Figure 4.2 P-T curve results from 1mm, 2mm and 5mm mesh sizes

Table 4.2. Summary pressure readings from mesh sensitivity analysis

Mesh size (mm)	Gauge @ 0.5m				Gauge @ 1m			
	Pressure (kPa)	Diff (%)	Impulse (Pa s)	Diff (%)	Pressure (kPa)	Diff (%)	Impulse (Pa s)	Diff (%)
1mm	5217	-	199	-	2488	-	256	-
2mm	5274	1.1%	199	0.0%	2422	-2.7%	280	9.3%
5mm	4742	-9.1%	190	4.7%	2282	-8.3%	286	11.7%

Owing to the unconventional configuration of the cased charge, which featured a pre-scored case and was detonated without endcaps, conventional methods for calculating the equivalent bare charge mass (C_{EB}), such as those from Fisher (1953) and Hutchinson (2009), were not applicable. Instead, the equivalent bare charge mass was determined through a series of numerical iterations. These iterations involved reducing the mass of the TNT charge from its baseline value of 2.12 kg, while preserving its aspect ratio, until the pressure and impulse measurements from the charge characterization tests were matched. The resulting equivalent bare charge mass, C_{EB} = 1.83 kg TNT, was modelled as a cylindrical form with a length of 570 mm and a radius of 25 mm. This value was then used to model the blast effects from the cased charge. The characteristics of the incident blast wave, as derived from test records and simulation results, are compared and presented in Figure 4.3 and the key parameters of the blast wave recorded are summarized in Table 4.3. When comparing the peak pressures, the difference in the simulation results

was less than 3% at 2.075 m, but increased to a range of 23% to 30% at 3.06 m. This difference may be attributed to the use of an equivalent TNT charge to model the explosive instead of modelling the actual m/46 charge, the TNT equivalency factor was adopted based on matching the impulse intensities and not the peak pressure, explaining the difference in matching the pressures at the different gauges. In terms of impulse, the simulation results closely matched the experimental tests, with a difference of less than 7% across all gauges. This validates the use of the equivalent bare charge mass of 1.83 kg TNT, the proposed mesh size, and the JWL parameters adopted for the simulations.

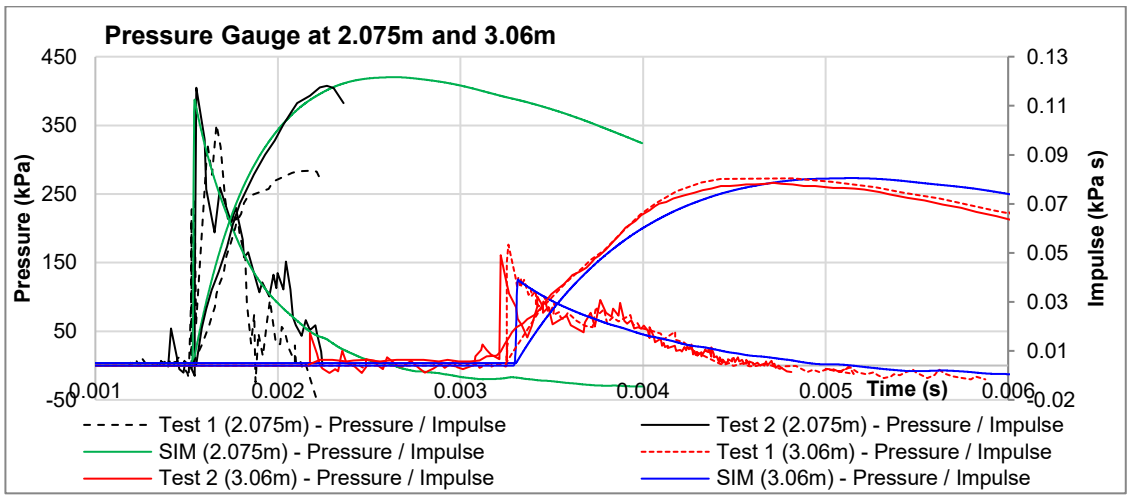

Figure 4.3. Pressure time histories from simulations against characterization tests at 2.075m and 3.06m

Table 4.3. Summary of blast profile analysis from simulation

	Gauge at 2.075m			Gauge at 3.06m		
	Peak Pressure (kPa)	Impulse (kPa s)	Time of arrival (msec)	Peak Pressure (kPa)	Impulse (kPa s)	Time of arrival (msec)
Test 1	-	-	-	176	0.0736	3.25
Test 2	407	0.113	1.54	162	0.0754	3.22
Simulation	394 [-3.3%]	0.121 [6.5%]	1.54 (0.6%) [0.3%]	131 (-34%) [-23%]	0.0752 (2.2%) [-0.3%]	3.28 (0.9%) [1.8%]

(% Difference compared to Characterisation test 1)
[% Difference compared to Characterisation test 2]

To further verify the 2D simulation models against the charge characterization test, a 3D quarter-scale model was constructed using the same modelling methodology. The 3D model consisted of a 2.5 m (width) x 4 m (length) x 4 m (height) rectangular air mesh, modelled using a Structured Arbitrary Lagrangian-Eulerian (SALE) mesh and filled with TNT, using the same JWL parameters and *INITIAL_VOLUME_FILL keyword. The

model included two symmetric boundaries along the TNT-filled interfaces, with a reflective boundary at the bottom to represent the ground. The remaining surfaces were free non-reflecting boundaries. The distance to the reflective boundary was 1.25 m from the centre of the charge. Four pressure gauges were placed along the centre of the charge at distances of 0.5 m, 1 m, 2.075 m, and 3.06 m. The setup of the 3D quarter-scale model is shown in Figure 4.4. A mesh size of 2 mm x 2 mm x 2 mm was applied for most of the model, with the mesh gradually increasing in size towards the Z-non-reflecting boundary.

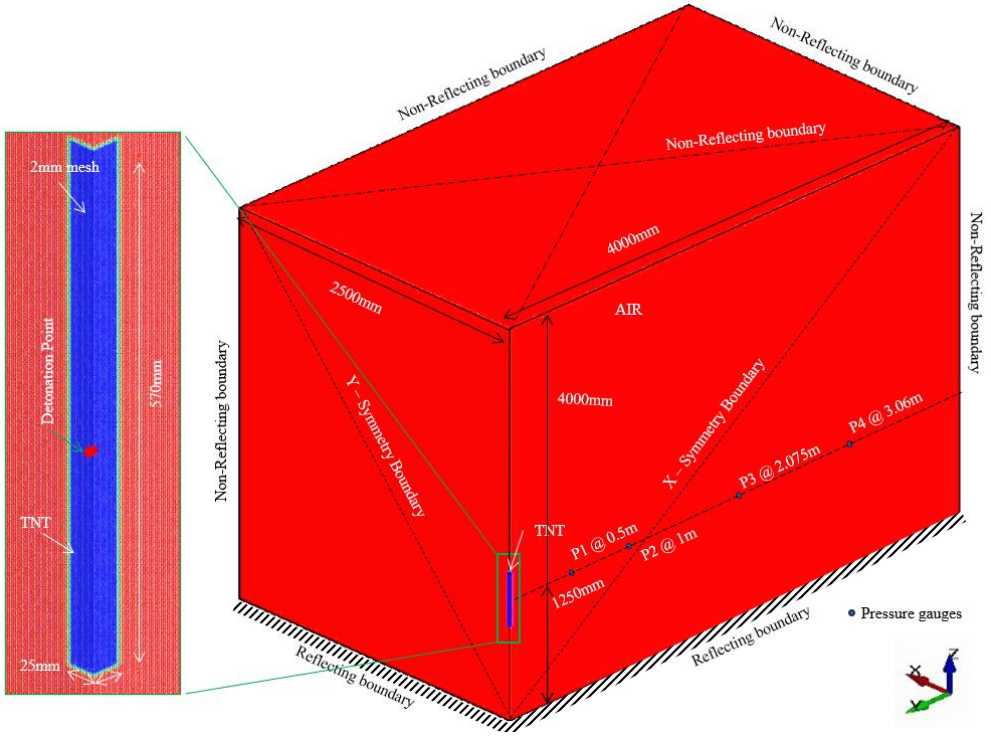

Figure 4.4. Setup of 3D quarter scale model of the TNT cylinder charge using SALE mesh

The pressure gauge results from the 2-Dimensional axisymmetric analysis and 3-Dimensional quarter-scale simulation, with the pressure gauge results recorded, are shown in Figure 4.5. The reflecting boundary surface causes interactions between the reflected and incident waves, creating the Mach front. Since both pressure gauges are located above the Mach front, potential interference between the incident wave front and reflected waves was assessed. The propagation of the incident and reflected waves to pressure gauge P3 through the 2D and 3D simulations at times t = 0.0015 s and t = 0.0045 s is shown in Figure 4.6. The 2D simulation results indicate that the incident wave reaches pressure gauges P3 and P4 (at 2.075 m and 3.06 m) at approximately 1.5 msec and 3.2 msec, respectively, followed by a smooth decay to the negative phase. The reflected wave is observed to arrive around 4.5 msec at pressure gauge P3 and 6.1 msec at pressure gauge

P4. In both cases, the reflected wave arrives after the positive phase of the incident wave. This behaviour was also observed in the 3D simulations. Therefore, it can be concluded that the reflecting boundary does not affect the positive phase of the incident pressure readings.

A summary of the comparison between the pressure gauge readings from the 2D and 3D models is presented in Table 4.4. When comparing the peak pressures, impulses, and arrival times of the incident waves, the results were found to be comparable, with differences of less than 15%. The simulation results were then compared with the experimental data, as shown in Table 4.5. The pressure-time results from the 2D axisymmetric model provided a closer match to the experimental data, with accurate predictions of the arrival times of both the incident and reflected waves. Additionally, the peak pressure magnitudes were closer to the experimental results. Furthermore, the 2D simulation demonstrated superior computational efficiency as compared to the 3D model. Hence, it was selected for use in subsequent analyses.

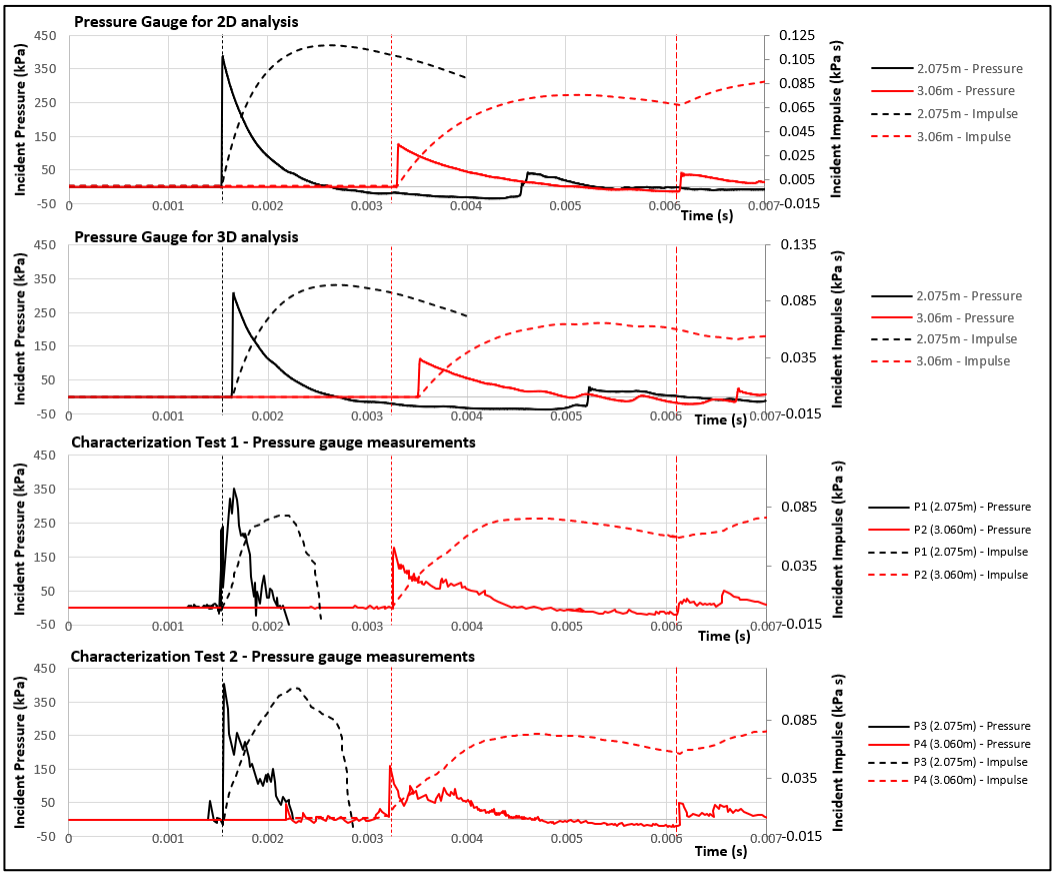

Figure 4.5 Comparison between the 2D, 3D and experimental pressure gauge results

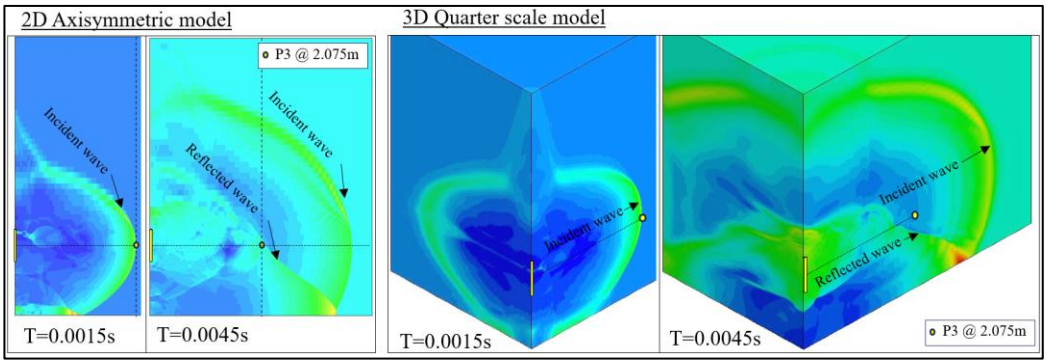

Figure 4.6. Illustration blast wave propagation through 2D (left) and 3D (right) simulations

Table 4.4. Comparison of blast profiles of 2D and 3D simulations

	Gauge at 2.075m			Gauge at 3.06m			
	Peak Pressure (kPa)	Impulse (kPa s)	Arrival time of incident wave (msec)	Peak Pressure (kPa)	Impulse (kPa s)	Arrival time of incident wave (msec)	Arrival time of reflected wave (msec)
2D Simulation	356	0.116	1.6	118	0.075	3.4	6.1
3D Simulation	307 (-13%)	0.099 (-14%)	1.6 (1%)	111 (-6%)	0.065 (13%)	3.5 (3%)	6.7 (10%)

(% Difference compared to 2D tests)

Table 4.5. Comparison of blast profiles from 2D and 3D simulations with the experimental tests

	Gauge at 2.075m		Gauge at 3.06m		
	Max Peak Pressure (kPa)	Average arrival time of incident wave (msec)	Max Peak Pressure (kPa)	Average arrival time of incident wave (msec)	Average arrival time of reflected wave (msec)
Characterisation Tests	407	1.5	176	3.2	6.1
2D Simulation	356 (-12%)	1.6 (6%)	118 (-32%)	3.4 (6%)	6.1 (1%)
3D Simulation	307 (-24%)	1.6 (6%)	111 (-36%)	3.5 (9%)	6.7 (9%)

(% Difference compared to Characterisation tests)

4.1.1. Sensitivity Study for JWL Parameters

A sensitivity study was conducted to investigate the influence of the JWL parameters to the blast wave generated. A total of three sets of TNT JWL parameters as reviewed by Poon et al. (2014) were studied in this analysis summarised in Table 4.6, denoted as TNT-1 by Lee et al., (1973), TNT-2 by Dobratz, (1981) and TNT-3 Souers et al., (1994). Both TNT-1 and TNT-2 JWL parameters are used as a default parameter selection in

AUTODYN software, TNT-2 is relatively newer out of the two parameters, and it is a common parameter used by other researchers (Schwer, L. E., 2016). TNT-2 was also used in the baseline study to determine the mass of the equivalent bare charge mass for blast effects.

Table 4.6. Summary of JWL Parameters

JWL Parameter	TNT-1	TNT-2	TNT-3
A (GPa)	373.75	371.25	454.86
B (GPa)	3.747	3.231	10.119
R_1	4.15	4.15	4.5
R_2	0.90	0.95	1.5
ω	0.35	0.30	0.25
E_0 (GPa)	6.0	7.0	7.8

Numerical simulations of the charge were performed with the three different TNT JWL parameters. The peak pressure, time of arrival (TOA) of blast wave and impulse from the characterization test were compared with the simulation results as shown in Figure 4.7 and summarized in Table 4.7. The simulation results from TNT-2 JWL parameters gave the closest match to the pressure gauge data from the experiment. The pressure readings at 2 m and 3 m matched with less than 5% and 20%, respectively. While the impulse readings at 2 m and 3 m matched with less than 7% difference. Similarly, the time of arrival of the blast wave matched the experimental results with less than 2% difference. Simulations from TNT-2 and TNT-3 yielded similar results, simulation results from TNT-3 yielded marginally higher pressures and quicker time of arrival as compared to those from TNT-2. The difference is more apparent at 3 m than at 2 m, notably, simulations with TNT-3 overestimated the impulse readings at 3 m by about 10%. Simulations using TNT-1 JWL parameters yielded the most difference, the magnitudes of pressure and impulse overpressure profile were noticeably lower at both pressure gauges, the time of arrival of the blast wave is also slower. Additionally, the time of arrival from the simulations was also compared to those measured from the experiments at 0.5 m to 1 m standoff distance, as shown in Figure 4.8 and summarized in Table 4.8. Similarly, TNT-2 and TNT-3 parameters returned very close estimates to the TOA measured from the experiments, with differences of less than 5%. Hence, it can be concluded that TNT-2 JWL parameters best represented the pressure profiles obtained from the charge characterization tests.

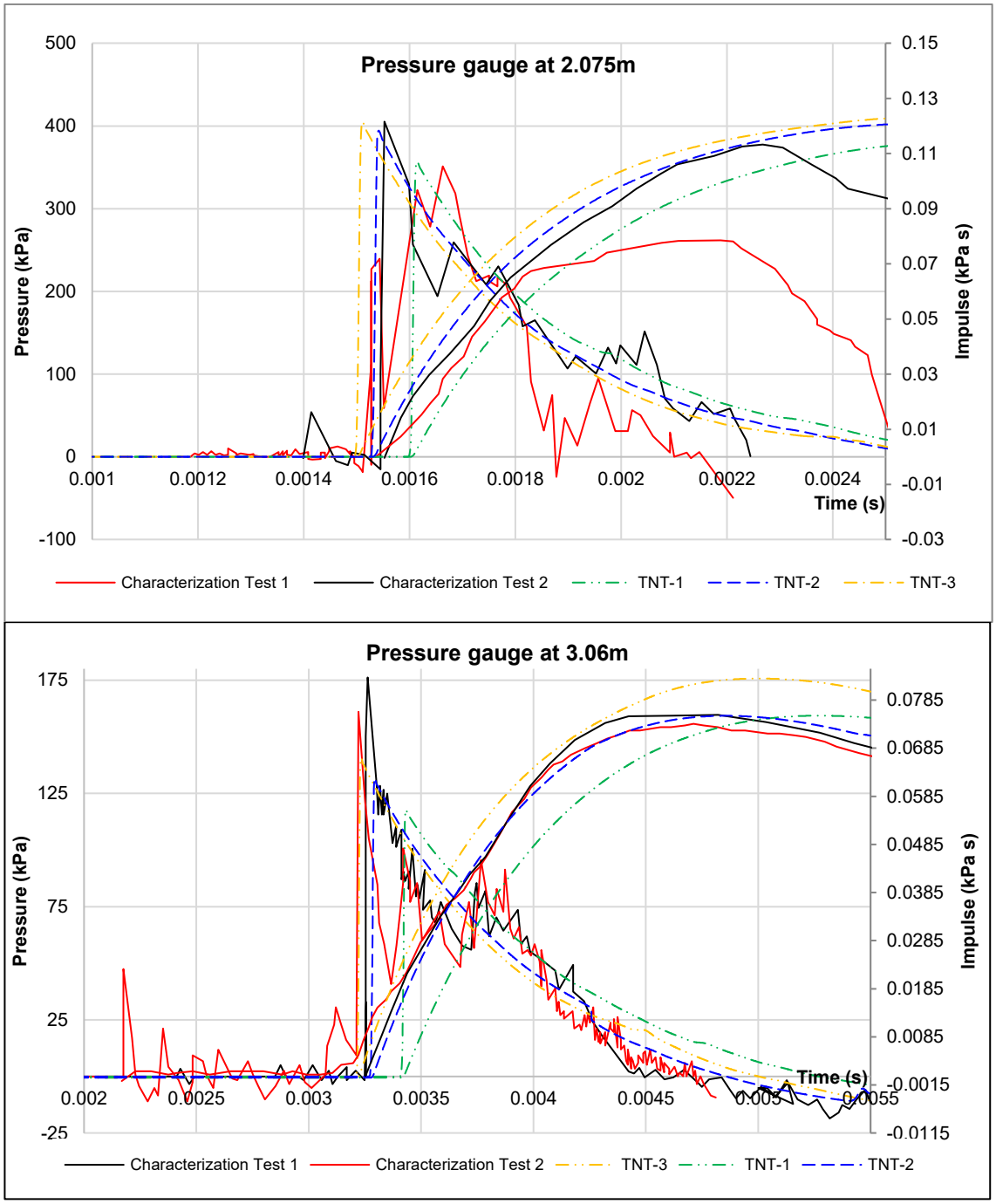

Figure 4.7. P-T curves from TNT-2 simulations against characterization tests at 2.075m (top) and 3.06m (bottom)

Table 4.7. Summary of blast profile analysis from TNT-1, TNT-2, TNT-3 simulations

	Gauge at 2.075m			Gauge at 3m		
	Peak Pressure (kPa)	Impulse (kPa s)	Time of arrival (msec)	Peak Pressure (kPa)	Impulse (kPa s)	Time of arrival (msec)
Chac Test 1	351	0.0785*	1.53	176	0.0736	3.25
Chac Test 2	407	0.113	1.54	162	0.0754	3.22
TNT-1	356	0.117	1.61	118	0.0830	3.42

	(2%) [-13%]	(33%) [3%]	(-5%) [-4%]	(-49%) [-38%]	(2.3%) [0.3%]	(-5%) [-5.8%]
TNT-2	394 (11%) [-3.3%]	0.121 (35%) [6.5%]	1.54 (0.6%) [0.3%]	131 (-34%) [-23%]	0.0752 (2.2%) [-0.3%]	3.28 (0.9%) [1.8%]
TNT-3	405 (13%) [-0.7%]	0.123 (36%) [8%]	1.51 (-1.3%) [-2.3%]	141 (-25%) [-15%]	0.0830 (11%) [9.1%]	3.23 (-0.6%) [0.3%]

*Likely error in instrumentation
(% Difference compared to Characterisation test 1)
[% Difference compared to Characterisation test 2]

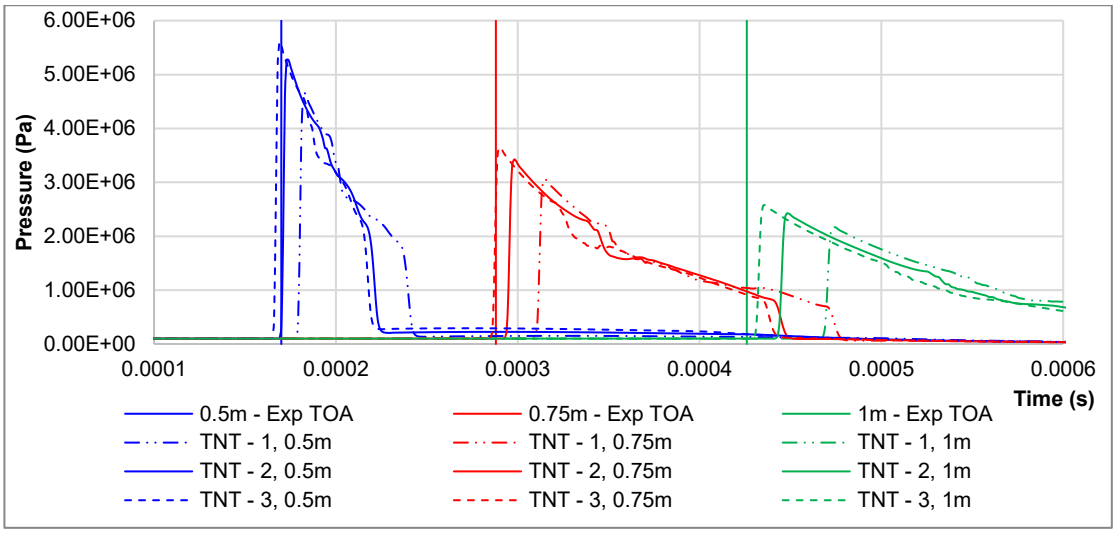

Figure 4.8. Illustration of time of arrival against P-T curves from various TNT JWL parameter.

Table 4.8. Summary of TOA analysis with simulations from various TNT JWL parameters

Test panel	Distance from charge, R (m)	Experimental TOA (msec)	TNT-1 (msec)	TNT-2 (msec)	TNT-3 (msec)
1	1m	0.426	0.469 (10.1%)	0.442 (3.8%)	0.431 (1.2%)
2	0.75m	0.288	0.311 (8.0%)	0.294 (2.1%)	0.286 (-0.7%)
3	0.5m	0.170	0.179 (5.3%)	0.169 (-0.6%)	0.164 (-3.5%)

(% Difference compared to experimental TOA)

4.1.2. Comparison Cylindrical Charges Against Spherical Charges

Modern design codes such as UFC 3-340-02 (DOD, 2008) provide design charts for the determination of blast overpressures based on scaled distance input and the selection of spherical or hemispherical TNT charge assumption. These design charts are based on characterized air blast parameters generated by TNT explosions for both spherical and hemispherical air burst through semi-empirical methods by Kingery-Bulmash (1984). In contrast, for a cylindrical charge, the blast waves propagate out from the tubular and end faces of the cylinder, causing reflections and bridging waves when the two wave fronts

meet, potentially increasing the peak overpressure along the radial axis of the charge (Knock, 2013). This effect is expected to be amplified with the charge's high L/D ratio of about 11.5.

The calibrated numerical models for the cylindrical charge were compared against incident overpressure profile generated from ConWep, with a spherical air blast assumption and the same charge weight of 1.83 kg, at the distance of 0.5 m (Z = 0.39 m/kg$^{1/3}$), 0.75 m (Z = 0.58 m/kg$^{1/3}$) and 1 m (Z = 0.78 m/kg$^{1/3}$). The simulation results of the blast profile are shown in Figure 4.9 and the difference is summarized in Table 4.9. The incident blast profiles of the cylindrical charge at close-in scaled distances generally possess a larger magnitude, but with slower initial propagation speed than the spherical charges from ConWep, and the comparison of blast wave from a cylindrical and spherical charge at 0.29 msec is illustrated in Figure 4.10. The overpressure profiles of the cylindrical charges showed larger peak pressure and impulse, with difference up to 74% and 40%, respectively, as compared to the spherical charges. The disparity in the peak pressure was minimal at 0.5 m but increased with the standoff distance, peaking at 74% at 1 m standoff distance. Meanwhile, differences in the impulse fluctuated at about 20%-40%, peaking at a standoff distance of 0.75 m. The difference in the time of arrival of the blast wave from the cylindrical charge was most pronounced at a standoff distance of 0.5 m, exhibiting a difference of 24%. However, this disparity diminished as the standoff distance increased, eventually tapering down to only a 0.9% difference.

To investigate the trend at far field, the blast overpressure profile was studied and compared at 2 m (Z = 1.64 m/kg$^{1/3}$) and 3 m (Z = 2.45 m/kg$^{1/3}$), as listed in Table 4.10. The overpressure profile of the cylindrical charges generally possesses a larger peak pressure magnitude, albeit with a smaller impulse, and exhibited consistently faster propagated than the spherical charges from ConWep. The difference between the peak pressures reduced with standoff distance from 30% at 2 m standoff to 12 % at 3 m standoff distance, indicating a quicker decay. Similar trends were present in the impulse analysis, the difference increased from -10% at 2 m to -18% at 3 m standoff distance.

It can be concluded that the shape effect of the charge is most significant at close-in scaled distances. The peak pressures and impulses are noticeably underestimated by equivalent spherical charges. This effect can be significant in the analysis of structural response due to the amplification of the magnitudes of the overpressure profiles from the consideration of reflected waves. At far field conditions, the equivalent spherical charge provides a

conservative estimate of the blast impulse. However, it is important to acknowledge that this estimation may tend to underestimate the peak pressure.

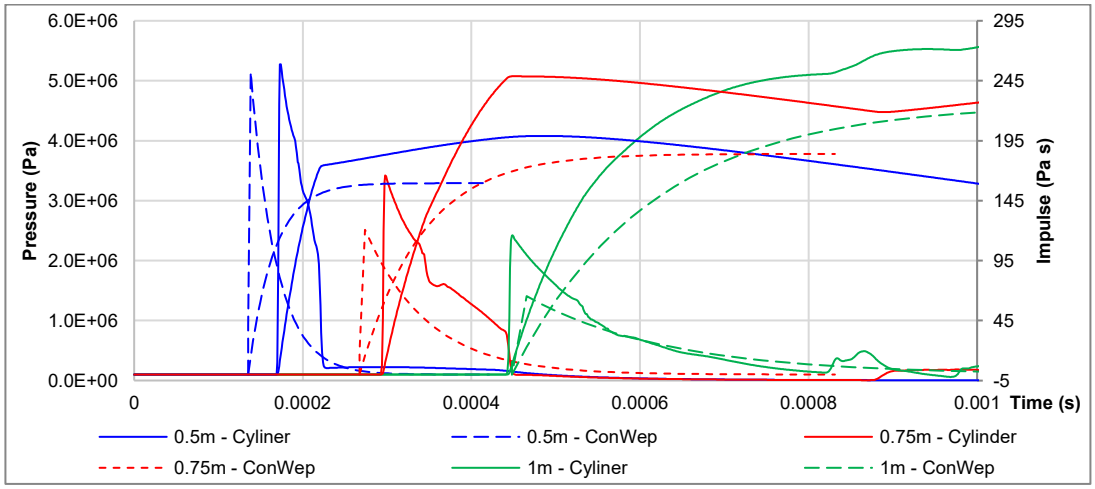

Figure 4.9. Pressure time history comparison between cylindrical charge and ConWep analysis

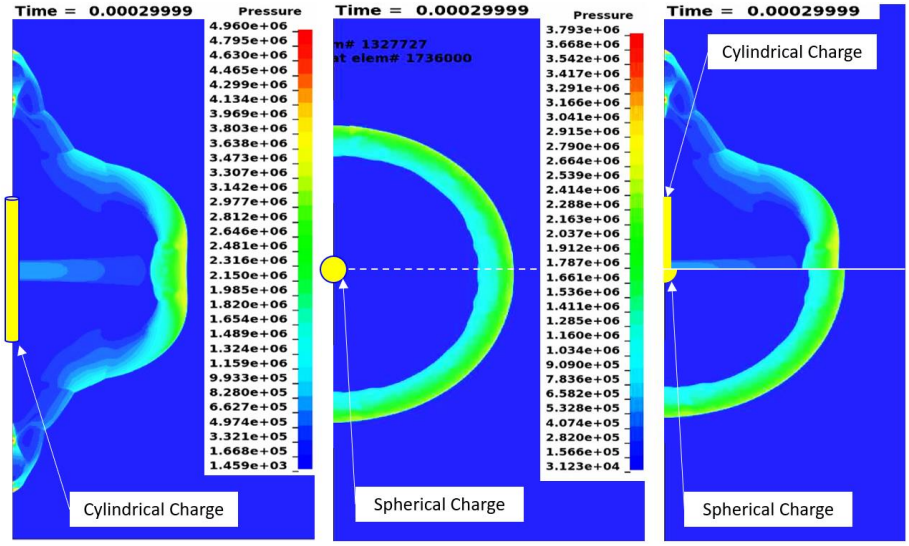

Figure 4.10. Blast propagation at 0.29msec of a cylindrical charge (left), spherical charge (middle) and comparison between cylindrical and spherical charge (right)

Table 4.9. Summary of blast profile analysis from ConWep and cylindrical charge at 1m to 0.5m

Blast profile	Gauge at 0.5m (Z = 0.39 m/kg$^{1/3}$)			Gauge at 0.75m (Z = 0.58 m/kg$^{1/3}$)			Gauge at 1m (Z = 0.78 m/kg$^{1/3}$)		
	Peak Pressure (kPa)	Impulse (Pa s)	Time of arrival (msec)	Peak Pressure (kPa)	Impulse (Pa s)	Time of arrival (msec)	Peak Pressure (kPa)	Impulse (kPa s)	Time of arrival (msec)
ConWep	5100	166	0.139	2512	184	0.274	1391	237	0.450
Cylinder	5274 (3.4 %)	216 (30%)	0.172 (24%)	3421 (36%)	254 (38%)	0.296 (8.0%)	2422 (74%)	280 (18 %)	0.44 (-0.9%)

(% Difference compared to ConWep analysis)

Table 4.10. Summary of blast profile from ConWep against cylindrical charge at 2m and 3m

Blast profile	Gauge at 2m (Z = 1.62 m/kg$^{1/3}$)			Gauge at 3m (Z = 2.38 m/kg$^{1/3}$)		
	Peak Pressure (kPa)	Impulse (Pa s)	Time of arrival (msec)	Peak Pressure (kPa)	Impulse (kPa s)	Time of arrival (msec)
ConWep	303	134	1.646	117.9	91	3.574
Cylinder	394 (30.3%)	121 (-9.6%)	1.54 (-6.4%)	131.8 (11.8%)	75 (-17.6%)	3.28 (-8.2%)

(% Difference compared to ConWep analysis)

4.2. Numerical Simulations for the Field Blast Test

This section discusses the numerical studies conducted to simulate the field blast test which subjected the SCC Panels to simultaneous blast and fragment loading.

4.2.1. Modelling of the SCC Panel

Lagrangian formulations were employed for the model of the SCC panels with uniform solid hexahedral elements for both the concrete and steel plates. A variety of material models have been developed for reinforced concrete in hydrocodes to replicate the dynamic responses and damage modes of the members loaded at high strain rates such as high velocity impact and explosive blast loading. As discussed in the literature review, the two common material models used by researchers for concrete under high strain rate loading conditions are the K&C revision 3 and RHT concrete material models. Since there is a need to deal with both blast loading and fragment impact penetration scenarios, the simulation of the SCC panels subjected to the simultaneous blast and fragment loading was performed using both the K&C revision 3 and RHT concrete model to evaluate the most appropriate model for concrete under these loading circumstances.

The K&C revision 3 concrete model considers the effect of stain such as strain hardening and softening behaviour as well as strain rate effects of concrete that is widely used in simulating concrete structures in a blast loading environment. Three separate strength surfaces define the K&C material model: initial yield strength surface, the maximum strength surface and the residual strength surface to define the elastic, plastic and softening behaviour (Malvar, Crawford et al., 1997). The K&C revision 3 model utilized for the reinforced concrete largely used default parameters generated by a compressive strength input of 35 MPa. The key parameters of the material model are listed in Table 4.11. Dynamic material properties accounting for strain rate effects were included using equations proposed by Wu et al. (2014). Element erosion techniques are employed by the inclusion of a material erosion card *MAT_ADD_EROSION to replicate the damage of concrete subjected to the combined loads. The element erosion criterion is significantly

influenced by the mesh sizes and will significantly affect the fragment penetration results. As it is not the intention of the study to precisely replicate the fragment penetration behaviour, rather to accurately replicate the resulting structural response from the combined loads, the erosion criteria were chosen to be as high as practically possible to avoid excessive mass loss while within a reasonable computational time. The erosion criterion of maximum principal strain (MXEPS) = 0.9 was adopted to remove the heavily deformed elements for stability of the numerical model (Chen et al. 2024).

Table 4.11. Key input parameters for K&C material model

ρ_0 (kg/m^3)	f_c (MPa)	γ	ft(MPa)
2400	35	0.19	3.2

Like the K&C material model, the RHT material model for concrete can accurately replicate shock propagation in concrete due to the formulation of non-linear and porous equation of states (EOS). The use of the RHT material model to approach high velocity projectile impact and blast loading on concrete was reviewed by Riedel (2009). The model uses three strength curves to represent the concrete which is influenced by the yield, maximum and residual damage capacity. These capacities are determined by the hydrostatic pressure, strain rates and stress triaxiality, which are a function of the lode angle of the loading. The three strength curves are interpolated by considering the material plasticity and the continuum damage evolution. Owing to the near simultaneous application of the combined loads, the propagation of the shock and progression of damage is critical. The RHT material was used with automatic parameters generation for concrete with f_c = 35 MPa. Since the RHT material model possess an integrated damage model, the default eroding plastic strain (EPSF) = 2 was adopted (Borrvall, 2011).

Both the steel plate and U channel beams were modelled using piecewise linear plasticity (MAT_024), adopting an elastic-plastic material behaviour with a nominal plateau slope through the hardening phase. The strain hardening modulus was taken as 1% of the modulus of elasticity as allowed in EN 1993-1-5 (CEN, 2009) and effects of strain rates on the dynamic material properties were included using Cowper-Symonds with effective deviatoric strain rate where C = 40 and P =5 (Chen et al., 2019).

A summary of the material properties of the steel plates and U channel is presented in Table 4.12. Within the panel structure, the C Channel stiffener beams were connected

rigidly to the bottom steel plate where the beam was welded to the plate, at the top of the panel, due to the provision of slotted holes for the welded connections, the rigid connections were defined only where the slotted holes were provided. For the steel and concrete materials, since there were no interface mechanical connections, the interface was modelled with keyword *AUTOMATIC_SURFACE_TO_SURFACE contacts with coefficient of friction of 0.35 between the steel and concrete selected based on the lower bound values of interface friction coefficients studied by Guo et al. (2020).

Table 4.12. Steel plate and U channel steel properties

*MAT_PIECEWISE_LINEAR_PLASTICITY						
Steel Members	σ_y (MPa)	ρ_0 (kg/m^3)	E (MPa)	υ	E_{tan} (MPa)	Failure ε
Steel plates	355	7800	210	0.29	2.1	0.3
U channel beams	235					

The mesh size adopted for the SCC panel is a critical parameter that would influence the simulation results of the fragment penetration and subsequent structural response. Hence, a mesh sensitivity study was performed through simulation of a single fragment penetration into the SCC panel to determine the appropriate mesh size for the analysis. For this study the RHT material model with default recommended eroding plastic strain = 2 was used. For the fragments impacting the SCC panels, Zukas et al. (2020) recommended a minimum of three continuum elements across critical dimensions such as the radius of the impactor for Lagrangian calculations. From the charge characterization tests, the fragment impactor had an average mass of 2.177 g and an average equivalent diameter of 8.1 mm. The shapes of the fragments were not reported, hence for simplification, they were idealised as a discrete sphere with a diameter of about 8.2mm to replicate the actual mass, constructed by solid hexahedral elements employing a mesh size of about 1.5 mm. The fragments conservatively adopted a rigid body assumption using material *MAT_RIGID with elastic mild steel properties to ensure that the energy possessed by the fragments are fully transferred the panel. The contact between the fragments, steel and concrete was achieved using *CONTACT_ERODING_SURFACE_TO_SURFACE to simulate the impact and associated penetration of the fragments on the panel. Lastly, the fragment was assigned to be an initial velocity of 1803 m/s, as calculated by Gurney's equation in the previous section, by keyword *INITIAL_VELOCITY_RIGID_BODY. The mesh sensitivity study of the panel was conducted with 3 mm, 1.5 mm and 1 mm. The results demonstrated that

the penetration depth converged at 1.5 mm mesh, as shown in Figure 4.11. When the mesh was reduced from 3 mm to 1.5 mm, the penetration increased by about 35%, however, when the mesh size was further reduced to 1 mm, the penetration depth increased by only about 8%. Considering the need to balance computational resource and accuracy, the mesh size of 1.5 mm was chosen to model the SCC panel.

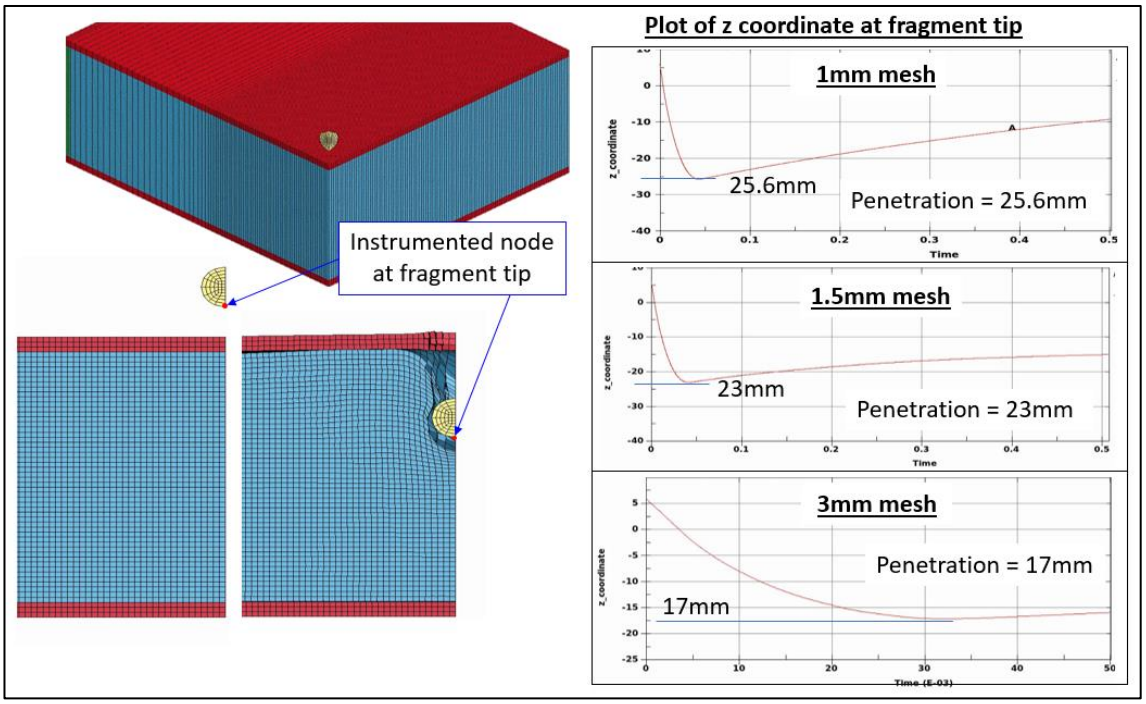

Figure 4.11. Illustration of fragment penetration analysis in mesh sensitivity study

The SCC panel adopted a quarter model with symmetrical conditions on the two reflected sides of the panel is presented in Figure 4.12. The SCC panel consists of 9.8 million elements with a constant square mesh with size of 1.5mm, across the thickness of the steel plate and concrete sections, there were 2 and 33 elements respectively.

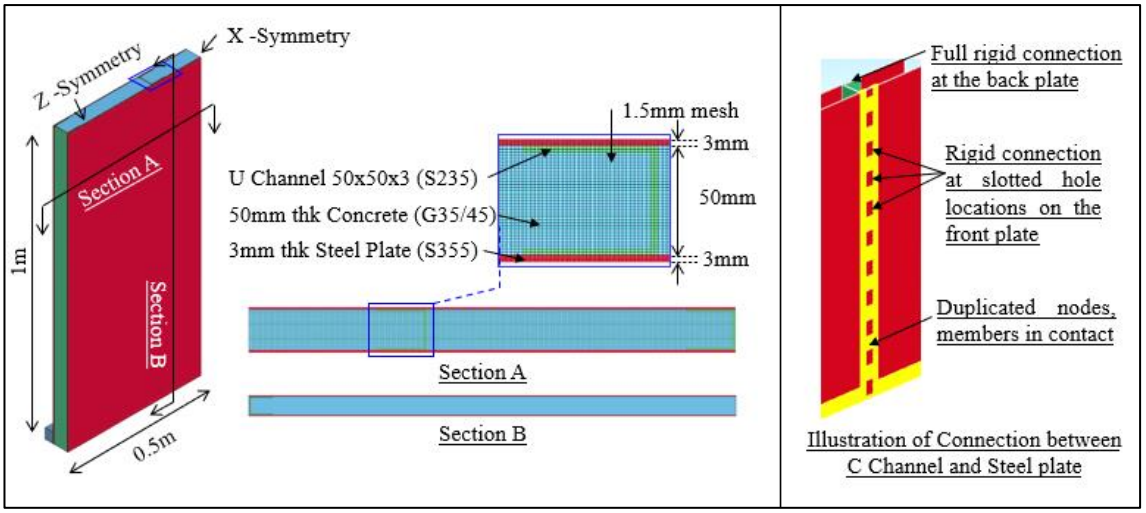

Figure 4.12. Illustration of composite panel model

4.2.2. Fluid Structure Interaction between the SCC Panel and Air Blast

The numerical study first analysed the SCC panels subjected to blast loads from a 570 mm long cylindrical bare charge with a radius of 25 mm that comprised of 1.83 kg of TNT, using the calibrated model parameters from Section 4.1. The Structured Arbitrary Lagrangian Eulerian (SALE) mesh adopting 2 mm regular square mesh was used for the air and TNT charge (the same as the characterization tests). Keyword *CONSTRAINED_LAGRANGE_IN_SOLID was used for fluid structural interaction, as shown in Figure 4.13. The maximum resultant reflected blast pressure extracted from a gauge at the centre of the panel is presented in Figure 4.14 and key parameters from the reflected blast wave are summarized in Table 4.13. The results showed that the arrival times of the blast wave from the simulation at all three tests matched the measured times from the experiment well with a difference of less than 3%.

The results of the structural analysis of the SCC panels to the blast loads modelled with SALE and deflection curves recorded from the experiments are presented in Figure 4.15 and the key parameters of the structural deformation are summarized in Table 4.14. The simulation results indicated that the structural response was under-predicted by up to 64% against the experimental measurements. This study confirms that the consideration of blast loads alone in close-in threat scenarios with cased charge is insufficient, emphasizing the need to include fragment loads in the analysis.

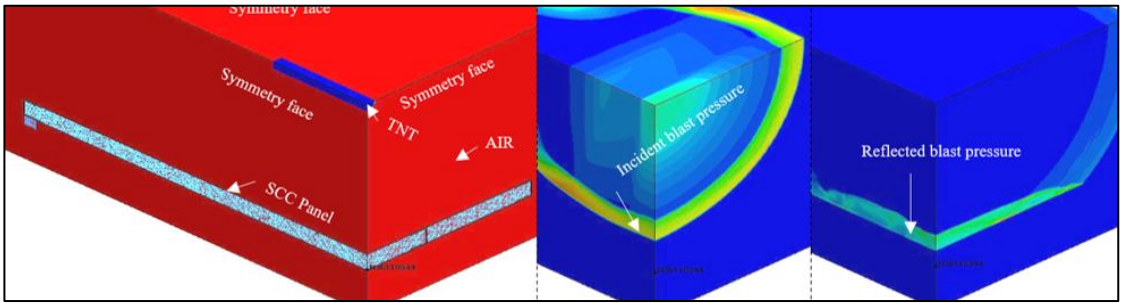

Figure 4.13. Illustration of fluid structure interaction between SALE with Lagrange mesh

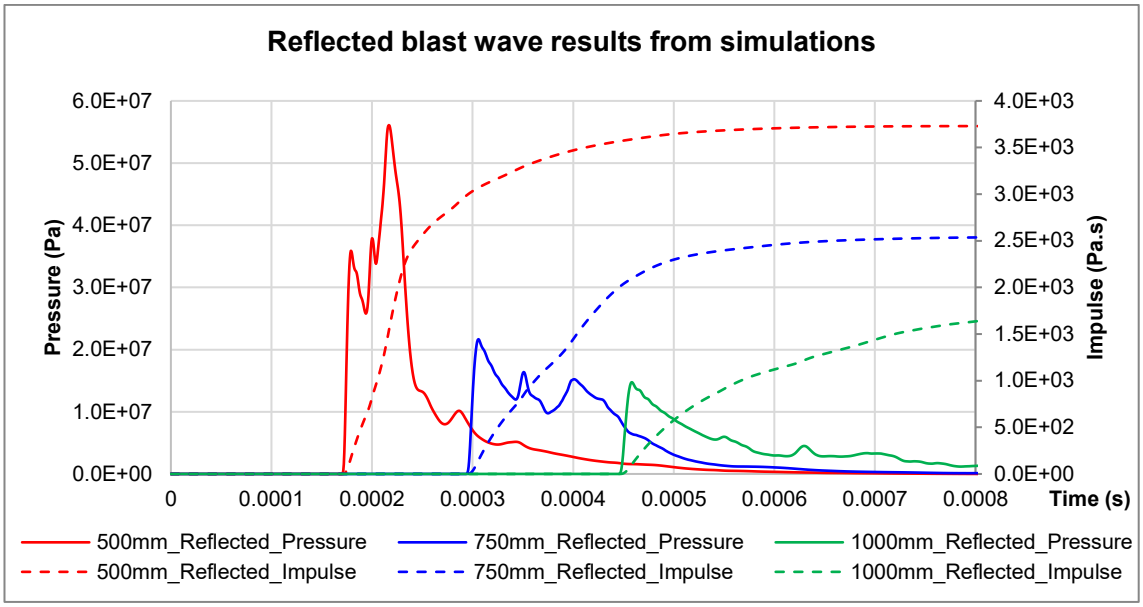

Figure 4.14. Reflected blast wave pressure time history from simulations

Table 4.13. Summary of structural response from experiments against simulations subjected to cylindrical charges

Test panel	Distance from charge, R (m) / Z (m/kg$^{1/3}$)	Arrival time of reflected blast pressure (msec)			Peak Reflected pressure (kPa)	Peak Reflected Impulse (Pa.s)
		Exp	Sim	Difference		
1	1m (Z = 0.78)	0.426	0.437	2.6%	14.7	1756
2	0.75m (Z = 0.58)	0.288	0.293	1.7%	21.6	2550
3	0.5m (Z = 0.39)	0.170	0.170	0.0%	56.1	3730

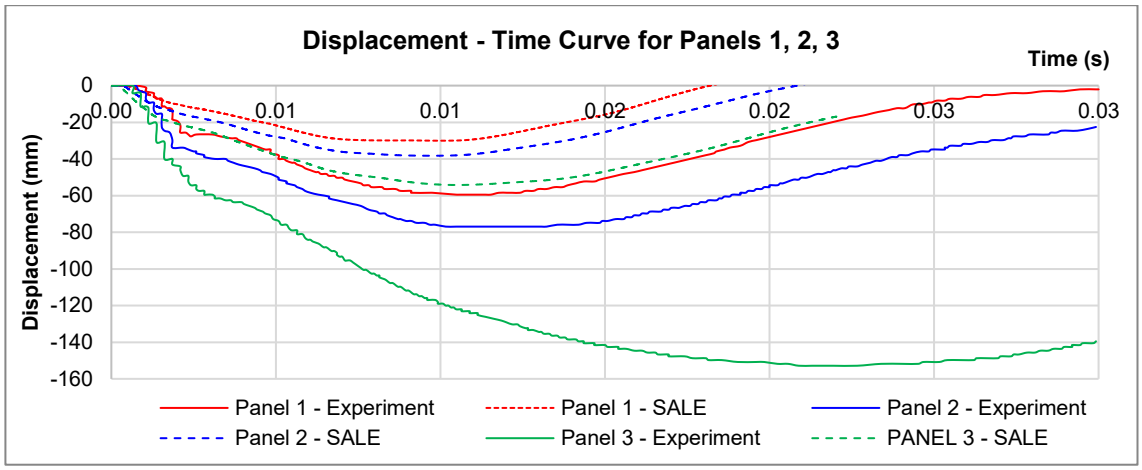

Figure 4.15. Structural response to cylindrical charge from SALE mesh against experimental results

Table 4.14. Summary of structural response from experiments against simulations with cylindrical charges

Test panel	Distance from charge, R (m) / Z (m/kg$^{1/3}$)	Max mid-span deflection (mm)			Time at max deflection (msec)		
		Exp	Sim	Diff	Exp	Sim	Diff
1	1m (Z = 0.78)	60	30	-50%	11	9	-18%

2	0.75m (Z = 0.58)	78	38	-51%	11	9	-18%
3	0.5m (Z = 0.39)	153	55	-64%	21	11	-33%

4.2.3. Numerical Model for Concurrent Blast and Fragment Impact Loading

A fully coupled model was constructed to replicate the concurrent loading from the blast and fragment impact like the experimental test. A half model is adapted for this simulation to avoid boundary complications due to the "erosion contacts" used to model fragment penetration into the panel. To simulate the blast loads, a different approach was taken to optimize computational efficiency. From the coupled SALE model presented in the previous section, 50 discrete pressure gauges were instrumented in 100 mm square grids just above the panel to record the reflected pressure on the panel from the bare cylindrical charge. Subsequently, the surface of the panel is assigned into 50 discrete segments. Majority of the segments on the panel assumed a 100 mm x 100 mm square arrangement, while the segments along the edges adopted a rectangular arrangement to ensure continuity to the boundaries. The individual blast load profile is subsequently applied to each segment based on their corresponding locations with the keyword *LOAD_SEGMENT_SET, as shown in Figure 4.16.

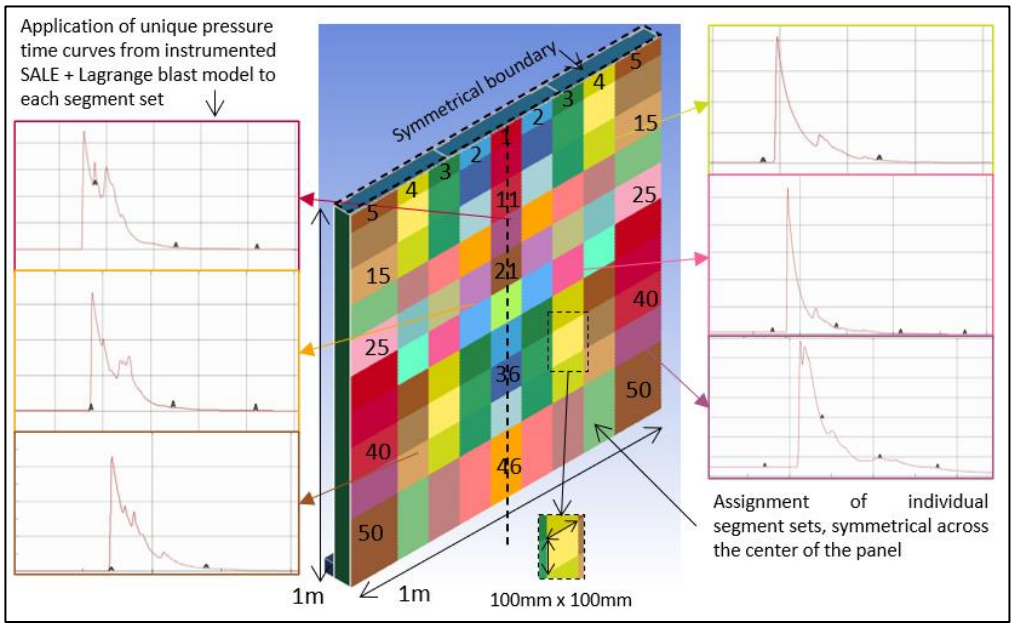

Figure 4.16: Illustration of blast load application on the SCC panel

Next, to simulate the fragment impact, similar approach was taken as the mesh sensitivity analysis. Each fragment was idealized as a discrete sphere constructed by solid hexahedral elements employing a mesh size of about 1.5 mm with Lagrangian formulations and was idealised as rigid bodies using *MAT_RIGID with mild steel elastic properties. The contact between the fragments, steel and concrete was achieved using

*CONTACT_ERODING_SURFACE_TO_SURFACE to simulate the hypervelocity impact of the fragments on the panel. To reproduce the actual mass of the fragment from the experiments, each fragment sphere had a diameter of about 8.2 mm. To replicate the fragment impact pattern in the simulations, the fragments were arranged in discrete rows of 5 to 9 depending on the stand-off distance. Each row consists of 17 full fragments and 1 half fragment based on the half symmetric model adopted. The model was simplified to assume a single initial velocity for all fragments within the model applied by using *INITIAL_VELOCITY_RIGID_BODY, due to the complexity of validating the velocity distribution of the fragments along the length of the charge. To replicate the loading sequence of the fragments with the blast loads, the initial velocity assigned was the average velocity of the fragment travelling from the case to the panel. The average velocity, V_A, was derived by the taking the average of the launch velocity from the charge and the striking velocity on the panels. As presented in the previous section on fragment velocity analysis, Equations from Gurney (1943) were used to calculate the initial fragment velocity. Subsequently, equations from UFC 3-340-02 (DOD, 2008) were referenced to calculate the fragment velocity reduction with distance due to air drag to obtain the striking velocity. The calculated average velocities for the 3 tests are shown in Table 4.15. As the charge was in proximity, the differences in the magnitudes of the striking and average velocities were marginal with the largest difference of about 1.5%, confirming that the use of the average velocity as the initial fragment velocity was appropriate.

Table 4.15. Calculated fragment velocity for the Tests 1, 2 and 3.

Test panel	Distance from charge, R (m) / Z ($m/kg^{1/3}$)	Calculate d V_0 (m/s)	Calculate d V_S (m/s)	Calculated V_A, (m/s)	Difference between V_A and V_S, (m/s)
1	1m (Z = 0.78)	1805	1750	1777	1.5%
2	0.75m (Z = 0.58)	1805	1764	1784	1.1%
3	0.5m (Z = 0.39)	1805	1777	1791	0.8%

Across the section of the charge, the radial launch of each row of fragments was replicated by the assignment of a launch angle based on the separation of 9.47 degree between adjacent fragment rows reported. Along the length of the charge, the fragment launch trajectory and velocity variation were not considered, similarly due to the complexity of the verifying the velocity distribution and the resultant launch trajectory. Instead, before the fragments were launched, they were arranged along each row to be equally spaced across the fragment impact zone to reproduce similar fragment impact patterns from the

experimental tests. Each row of fragments would be assigned as the same velocity based on the launch trajectory detailed above. The fragment impact zone was along the length of the charge from the experimental test; 0.868 m, 0.807 m and 0.725 m for Test Panels 1, 2 and 3, respectively, were adopted. An illustration of the fragment idealization and launch conditions is shown in Figure 4.17.

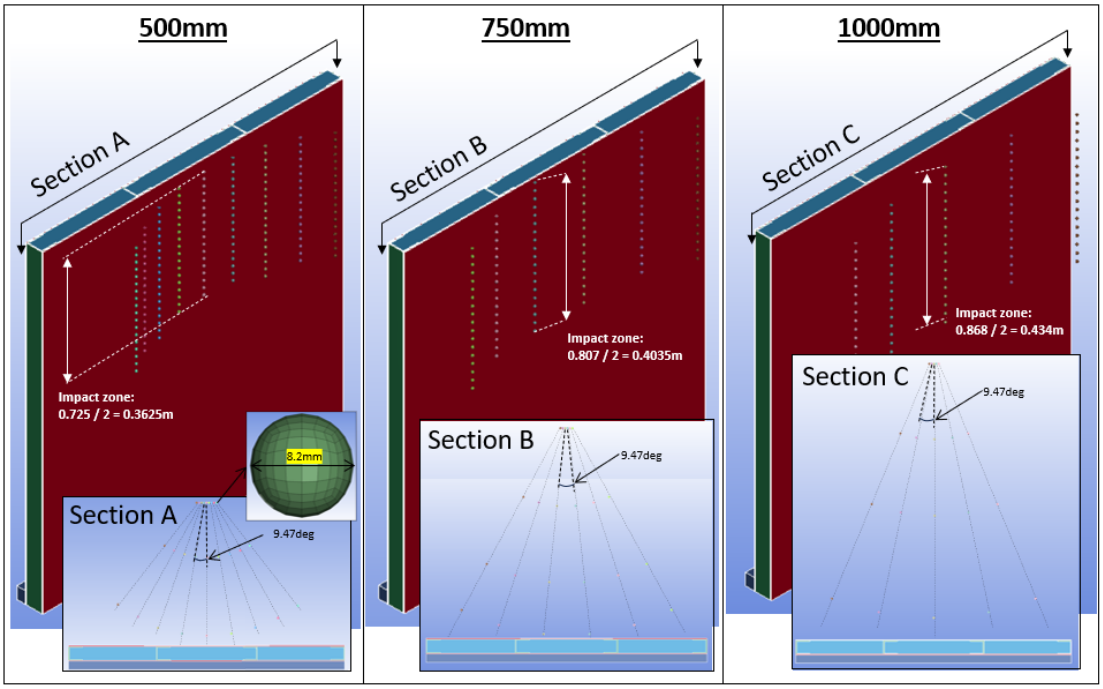

Figure 4.17: Illustration of fragment idealization and launch conditions adopted

The SCC panel largely adopted the same modelling principles as presented in Section 4.2.1. The mesh size, material models of the steel and contact descriptions were followed. As discussed, both K&C and RHT concrete material models are popular material models used for concrete under high strain rate loading conditions such as in a blast environment and fragment penetration scenarios. In this study, there is a need to deal with both blast loading and fragment impact penetration scenarios, hence, the simulations were conducted with both K&C revision 3 and RHT material model to evaluate the most appropriate model for concrete that is subjected to the simultaneous blast loading and fragment impact.

Due to the large computational resource required to simulate the penetration behaviour, the simulation was conducted in 2 phases using the Restart function in LS-DYNA. The full simulation was first executed for 2 msec to allow for sufficient time for the fragment impact and full energy transfer until the fragments approach rest. Subsequently, the restart analysis was executed to remove the fragments and respective contacts from the model to speed up computation of the subsequent structural response.

The simulation results of the midspan deformation response are shown in Figure 4.18 and the maximum deformations are summarised in Table 4.16. The K&C and RHT models both returned similar results at 1000 mm. However, when the stand-off distance was reduced to 750 mm, the K&C model predicted the deformations better at 10% difference compared with the RHT models that are at 20% difference. When the stand-off distance was the closest at 500 mm, the K&C model however under predicted the structural response by about 10%, while the RHT model replicated the deformation well with less than 2% differences. The failure patterns of the SCC panel similarly showed local compression buckling failure of the top plates for both models, as shown in Figure 4.19. Analysing the buckling failure geometry of the top steel plate, the K&C model showed a stronger symmetrical diagonal buckling pattern explaining the smaller structural deformation to the RHT models. While the RHT models showed consistent buckling near the mid span, which compared better to the experimental results. Overall, the RHT models provided a more accurate and consistent representation of the structural deformation as compared to the experimental data.

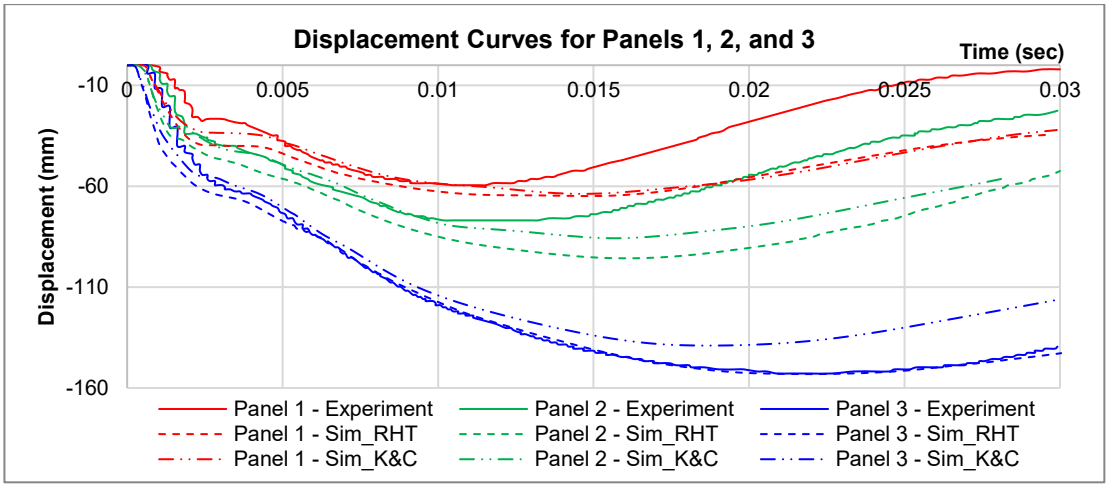

Figure 4.18. Structural response of the coupled simulation against experimental results for K&C and RHT material model

Table 4.16. Summary of the comparison of structural deformation for the simulation against the experimental results

Test panel	Distance from charge, R (m) / Z (m/kg$^{1/3}$)	Max deflection at mid-span (mm)				
		Exp	RHT - Sim	Diff	K&C -Sim	Diff
1	1m (Z = 0.78)	60	64.9	8.2%	63.8	6.3%
2	0.75m (Z = 0.58)	78	95.7	22.7%	85.8	10.0%
3	0.5m (Z = 0.39)	153	153.1	0.1%	139	-9.2%

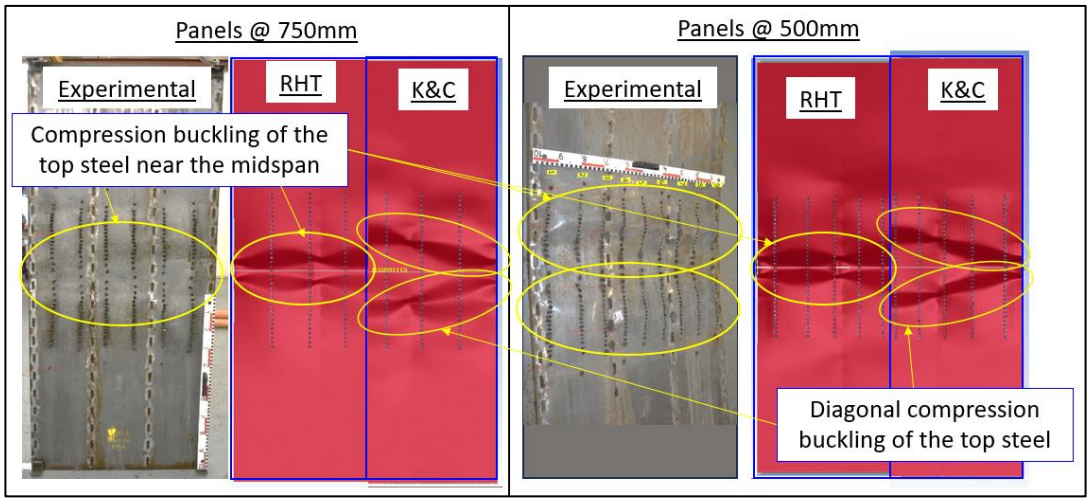

Figure 4.19: Panel failure deformations for RHT and K&C model at 750mm and 500mm

Comparing the fragment penetration into RHT and K&C models as shown in Figure 4.20, the fragment penetration behaviour of the RHT matched close to the experimental results where the fragments penetrated large sections of the concrete close to the base of the panel leaving about 10 mm section depth, while the penetration of the fragments in the K&C model was notably lesser than the experimental results, penetrating only about 16 mm into the concrete section. This difference in the fragment penetration behaviour produced a shorter penetration time in the concrete in the K&C model resulting in a shorter loading duration as can be witnessed from the impulse profile from the force contacts between the concrete and steel show that the K&C model full force transfer was within 0.05e-3 s whereas the RHT model took 3 times longer, 0.15e-3 s, to achieve the full force transfer from the fragments to the concrete.

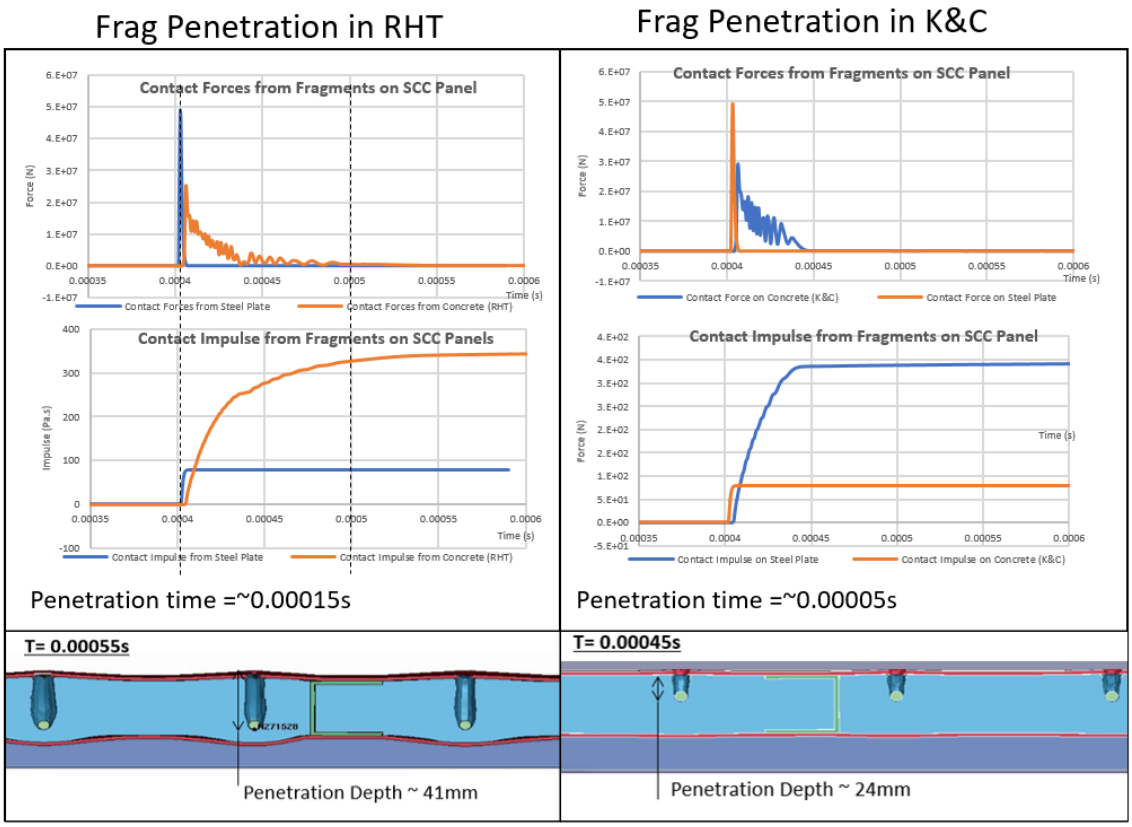

Figure 4.20: Illustration of contact forces extraction and fragment penetration behaviour for the RHT and K&C model

The results from the RHT model matched the both the structural deformation and fragment penetration behaviour to the experiments well, hence, its results were utilized for subsequent discussions on simulation results for the blast and high velocity impact penetration of the fragments on the concrete section.

4.2.4. Results and Discussion from RHT Model

The results of the maximum deflection at the mid-span of the panel from the simulations for Panels 1, 2 and are presented in Table 4.17 and the maximum deflection time histories are summarized in Figure 4.21. The results from the numerical simulations predicted the dynamic response of the panel relatively well. Like the experimental results, for the initial ~2.5 msec, the structural response from the numerical simulations showed a linear deflection curve, and subsequently, the structure experienced dynamic bending to the maximum deflection. The slope and magnitude of the initial linear deflection curve increased as the scaled distance decreased, likely due to the initial shear plugging behaviour as a result of the shock wave from the blast pressure and fragment impact to the concrete core causing the linear deformation in the rear steel plate. Analysing the

structural response, when the stand-off distance was the furthest at 0.78 kg/m$^{1/3}$, the model replicated the structural response with a difference of 3%. However, when the standoff distances were reduced, the numerical simulation consistently returned more conservative predictions of the maximum structural response with the maximum differences of about 45%. When the standoff distance was the closest at 0.39 kg/m$^{1/3}$, the structural response predicted by the simulation matched the experimental results well with a difference of about 12%, the corresponding time at the max deflection returned similar accuracy with differences about 14%. However, when the standoff distance was 0.58 kg/m$^{1/3}$, the difference of both the deflection and corresponding structural response time increased to about 45% and 55%, respectively. At this scaled distance and fragment loading density, the simulation likely overestimated the concrete damage on the panel due to the fragment impact. This phenomenon can be similarly witnessed from the analysis of the time at the max deflection, which indicates softening of the panel because of the damage resulting in a larger structural period.

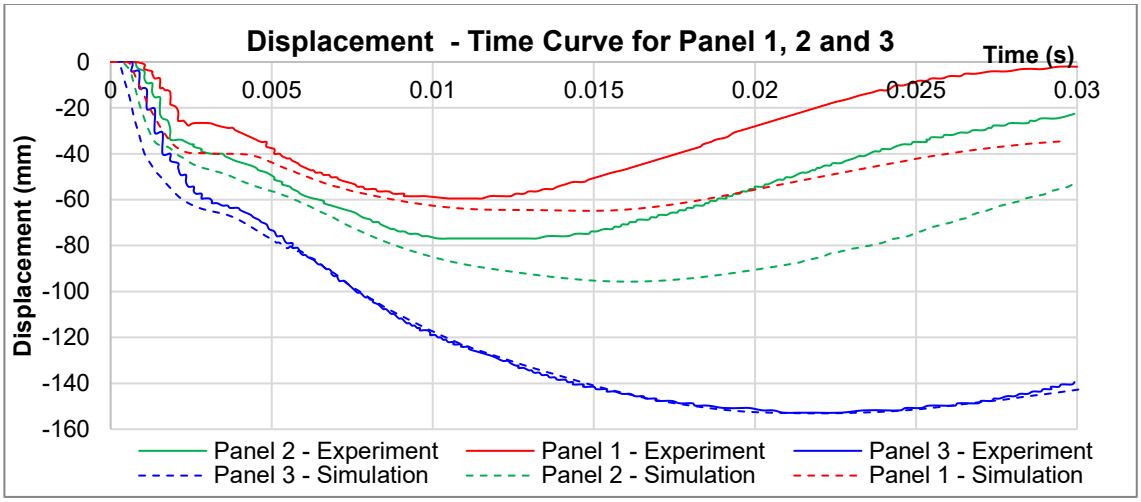

Figure 4.21: Structural response of the coupled simulation against experimental results for RHT model

Table 4.17. Summary of the comparison of structural deformation for the simulation against the experimental results

Test panel	Distance from charge, R (m) / Z (m/kg$^{1/3}$)	Max deflection at mid-span (mm)			Corresponding time (msec)		
		Experiment	Simulation	Difference	Experiment	Simulation	Difference
1	1m (Z = 0.78)	60	64.9	8.2%	11	14.8	34.5%
2	0.75m (Z = 0.58)	78	95.7	22.7%	11	16.1	46.4%
3	0.5m (Z = 0.39)	153	153.1	0.1%	22	21.9	-0.5%

Comparing the damage of the panel, the results of the simulations showed that the model can accurately replicate the failure mode of all the test panels. The comparisons of the residual damage from the simulations against the experimental results are presented in Figure 4.22, Figure 4.23 and Figure 4.24 for Panels 1, 2 and 3, respectively. All three SCC panels exhibited a distinctive plastic failure at their mid-spans, like the failure mode of a simply supported beam. The top steel plates exhibited compression local buckling failure that is symmetrical along the middle of the panel, the buckling failure extended from the mid-span across the entire fragment impact area in all three simulations, like the experimental results. Similarly, all three simulations accurately replicated the fragment penetration behaviour, the fragments perforated first steel plate was prevented by the concrete core without penetrating the bottom steel plate, proving that the RHT material model can replicate multiple fragment penetration scenarios.

For Panel 1, the simulations reproduced the damage patterns on the panel well. Both the buckling patterns of the steel plate and damage within the concrete section matched the experiments. Analysing the concrete surface, the craters formed by the multiple fragment impact and accompanying transverse cracking across the adjacent fragment rows matched the experimental results well. Across the section, the fragment penetration caused a localised heavily damaged crater around the impact zone accompanied by transverse cracks propagating across the adjacent fragment rows. Despite this, the damage of the section outside the crater is minimal.

For Panel 2, the simulations similarly predicted the buckling of steel plate facing the charge, concrete crater from the fragment impact and surface transverse cracking across adjacent rows of fragment relatively well. However, the simulation results exhibited excessive damage at the mid-span, as compared to the experimental data which showed damage concentrated in 2 clusters where bulk of the fragments impacted. This can be attributed to the idealization of the fragment loads; the fragments were modelled as rigid material bodies with no variance in velocity distribution along the row. The actual fragments were fabricated from mild steel that was expected to deform upon impact with the SCC panel, hence the rigid material used in the simulations would yield a more severe material damage from fragment impact penetration. Additionally, in the simulations, all fragments along a single row were assigned as a single speed calculated based on their

trajectory. While in the tests, the velocity of the fragments is expected to vary as a fraction of Gurney's velocity (Huang et al. 2015). Hence, the simulation is expected to overestimate the fragment's energy leading to higher momentum transfer and greater material damage from the impact. Additionally, the closer proximity of the fragment rows as compared to Panel 1 resulted in the formation of more transverse cracks across of the damage zone from the fragment impact, which exacerbated by the dynamic bending phase resulting in the fully damaged section at the middle of the panel.

Analysis of the simulation results from Panel 3 indicated similar buckling profile of the top steel across the fragment impact zone as compared to the experiments. The simulation however revealed a larger extent of the buckling of top steel plates that are close to the edge of the panels, the buckling exhibited a diagonal fold extending beyond the fragment impact zone, indicating a change in the buckling mode of the steel that may have resulted from a higher structure deformation or damage profile, as shown in Figure 4.24. The analysis of the concrete core within the panel revealed excessive damage where the fragment impacted. Due to the proximity of the fragment rows, the transverse cracks were able to propagate across each row, causing heavy damage across the entire concrete section. When compared to the experimental results, which recorded significant change in the structural period and extreme deformation implying that the panel's concrete core was significantly damaged, the damage predicted was closer to the experiment although it is expected to be more conservative owing to similar heavy damage the panels experienced resulting in a closer prediction of the structural response.

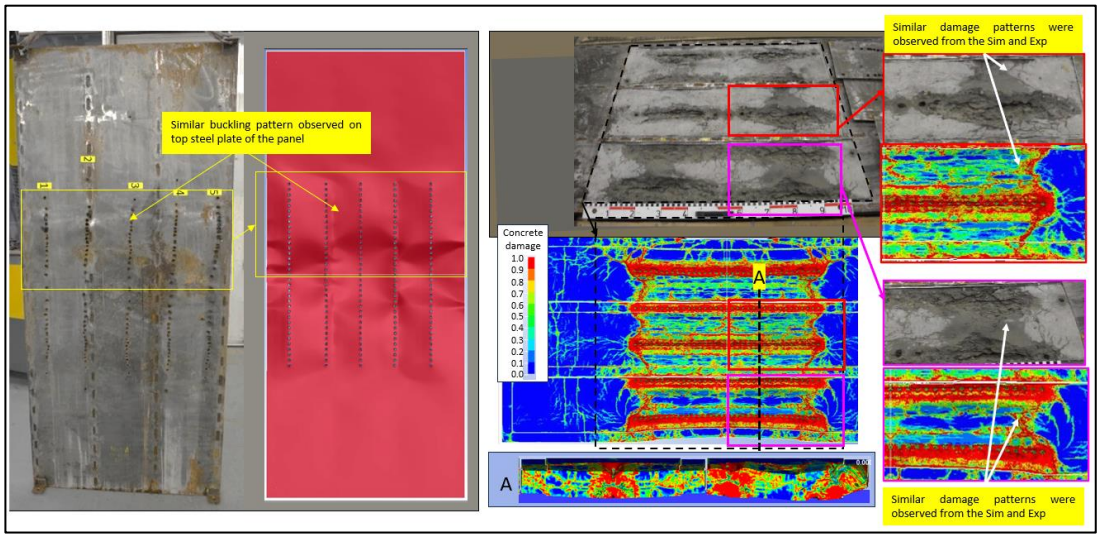

Figure 4.22: Simulated results illustrating damage comparison against post-test Panel 1 @ 1000mm

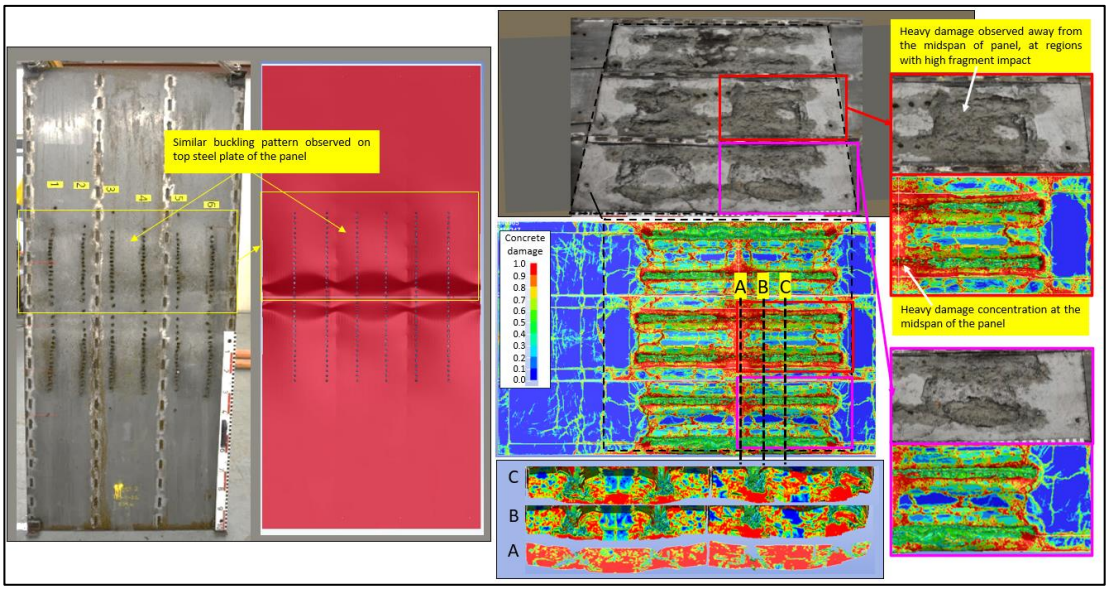

Figure 4.23: Simulated results illustrating damage comparison against post-test Panel 2 @ 750mm

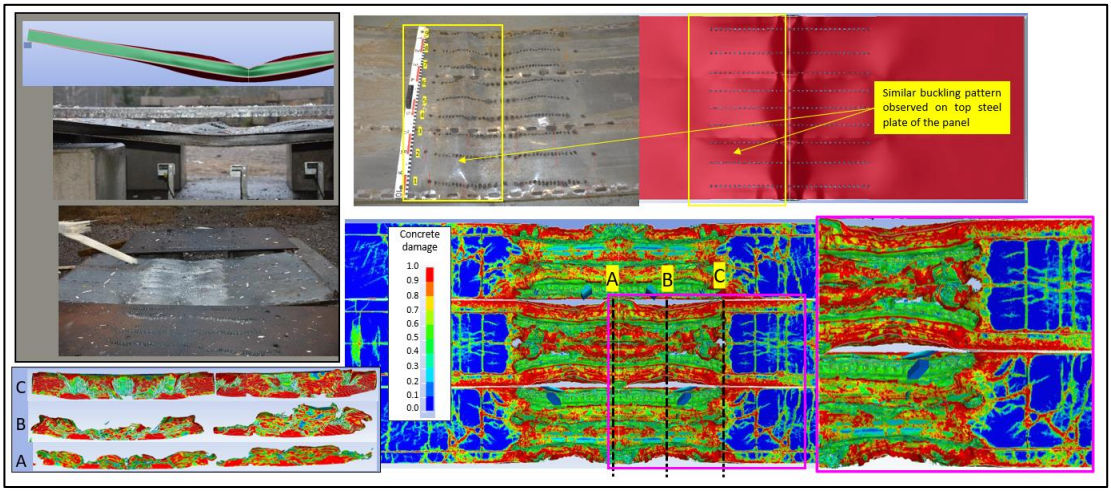

Figure 4.24: Simulated results illustrating damage comparison against post-test Panel 3 @ 500mm

Next, using Panel 2 as a reference panel, the damage evolution of the concrete across the panel at major time intervals can be divided as 1) initial fragment impact at 0.45 msec, 2) shear deformation phase at 0.85 to 1.6 msec, 3) dynamic deformation phase at 5.8 msec and 4) maximum structural deformation at 22.8 msec, as shown in Figure 4.25. During the shear plugging phase at 1.6 msec, the impact of each row of fragments caused a large damage zone across the concrete section, rendering the concrete section with heavy damage (damage index >0.9). The impact from the multiple fragments initially formed individual craters through the concrete section, as the stresses propagated through the section at about 5 msec, the craters merged across the adjacent fragments from each row

to form an elongated crater along the impact zone, causing synergistic damage resulting in an expanded crater along the entire row of fragments, similarly reported by Li et al. (2020). At the same time, large diagonal cracks formed below the impact zone indicating the formation of a spalled rear surface. Across the section, each row of fragments caused a heavily damaged zone upon impact that is about >50 mm wide, accompanied by transverse cracks propagating across the adjacent fragment rows. During the dynamic deformation phase, this damage was exacerbated resulting in almost fully damaged concrete section at its mid-span of the panel, evidenced in the section snapshot at 22.8 msec. At the impact zone, along the fragment penetration path, majority of the concrete was eroded leaving about 11 to 5 elements or about 15 mm to 7.5 mm section thickness that are heavily damaged, indicating that the section has been perforated by the fragments.

To further compare the damage evolution across the other test panels, the longitudinal section along the panel at the fragment impact zones and section across the mid-span were captured for all three test panels at the similar time intervals; 1) 1.6 msec for shear deformation, 2) 5.8 msec for dynamic deformation and 3) 22.8 msec for maximum structural deformation, the section cut along the length and width across the centre of the panel are presented in Figure 4.26 and Figure 4.27, respectively. The concrete damage patterns in Panel 2 were similarly witnessed with varying magnitude in Panels 1 and 3. The longitudinal section across the fragment impact zone from Panel 1 showed similar damage to Panel 2, both the depth of penetration and the evolution of the damage through the dynamic bending phase to the maximum deformation phase is comparable. However, the damage pattern across the section reveals more severe damage between the adjacent rows of fragments for Panel 2 as compared to Panel 1 due to their closer distance. During the dynamic bending phase, the damage can be seen propagating across the section to form a heavily damaged zone at Panel 2, whereas for Panel 1, the cross section excluding the fragment impact zone remains largely intact. Comparing against Panel 3, the longitudinal section cut shows the fragment penetrated almost through the entire section of the concrete but similarly did not penetrate the bottom steel plate. This is likely caused by the closer distance between the fragments along each row of fragments and hence greater synergy in the damage potential as discussed above. Across the section, the close distance between the adjacent fragment rows caused the damage to propagate much quicker as compared to Panel 2, the entire cross section of the panel was damaged as early

as the shear plugging phase at 1.6 msec during the dynamic bending phase at 5.8 msec, almost the entire concrete section was heavily damaged.

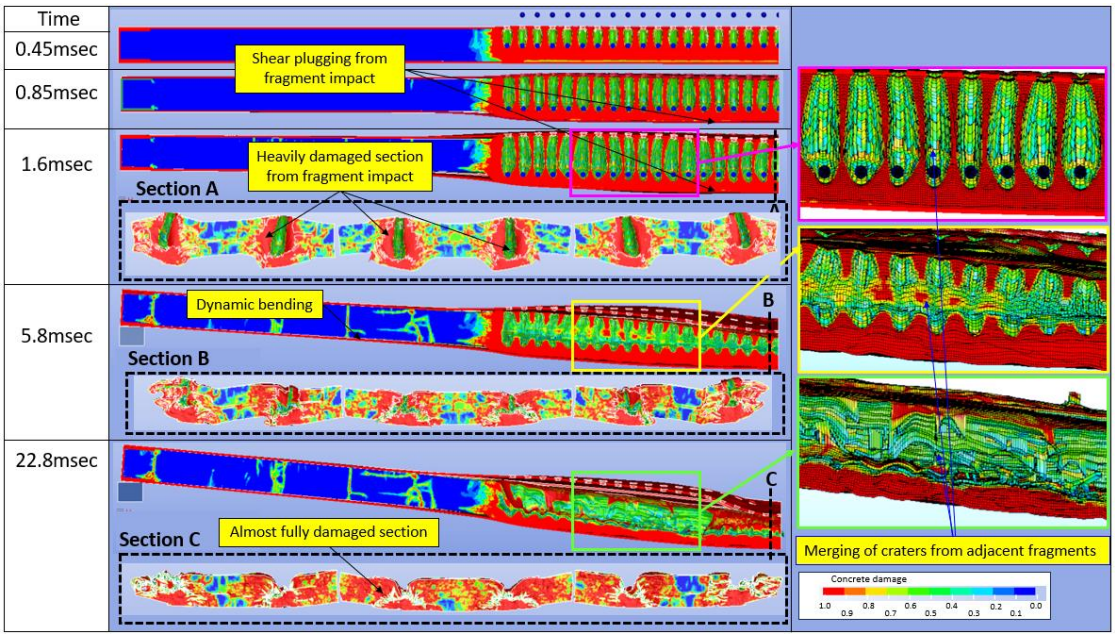

Figure 4.25: Damage modes from simulation results at various time intervals of Panel 2 at 750mm

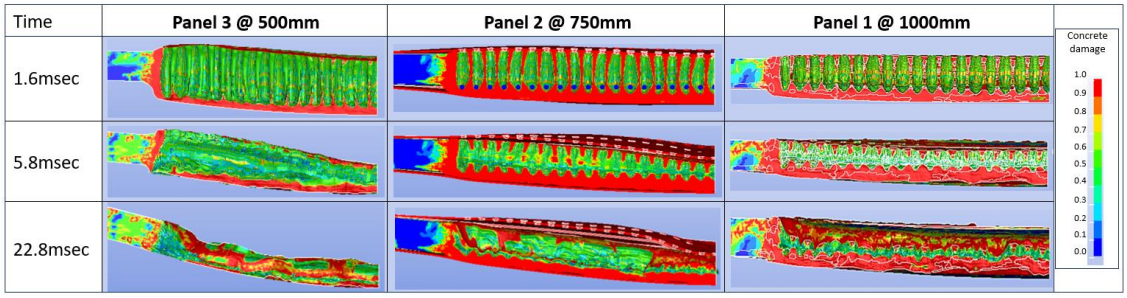

Figure 4.26. Longitudinal section across the fragment impact zone at various time intervals.

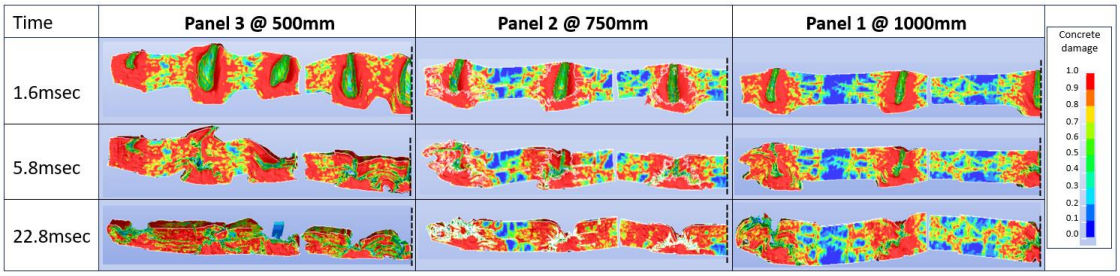

Figure 4.27. Section across the mid-span for the test panels at various time intervals

Analysing the velocity decay from a single fragment during the penetration process using results from simulation of Panel 2 revealed an exponential like deceleration profile as shown in Figure 4.28. The peak deceleration occurs at first contact with the top steel plate around 0.4 msec subsequently, when the fragment is penetrating the concrete, the

deceleration is reduced exponentially until the fragment losses most of its energy at about 1 msec. Significant deceleration occurs within the first 0.085 msec upon contact, reducing the velocity of the fragments from about 1800 m/s to about less than 100 m/s. Subsequently, the fragments experience a slow deceleration for another 0.5 msec until its velocity approaches zero. It is noted that the fragments do not come to a complete stop in the simulations as the structure would have responded and at some point, moved faster away from the fragments breaking contact between the concrete section and the fragments.

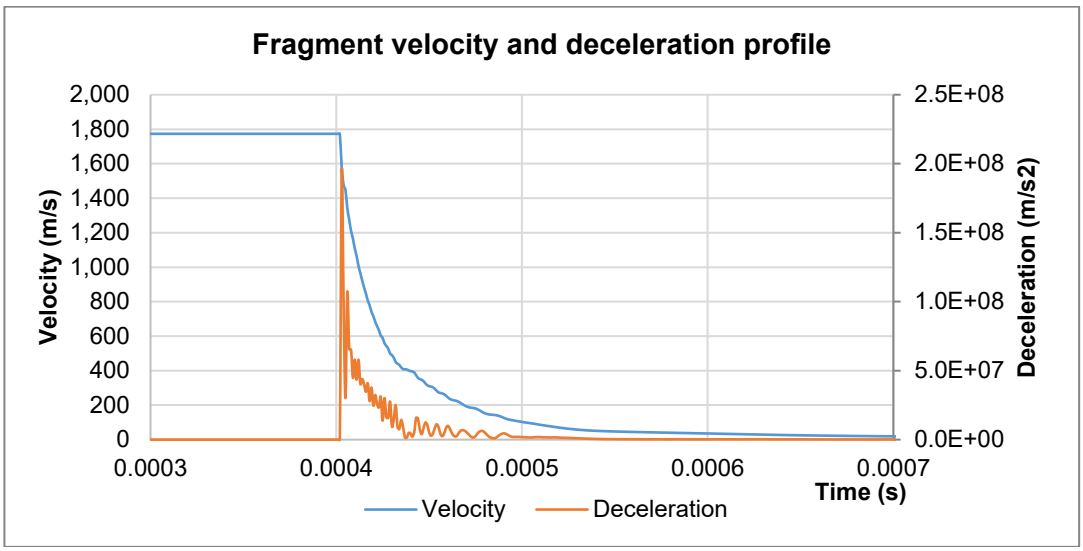

Figure 4.28: Velocity and deceleration profile of a single fragment upon impact on SCC panel

Further studies on the sequence of loading from the blast and fragments were conducted by analysing the resultant contact forces of fragments against the panel and the blast loading application. The blast profile at the both the centre and corners of the fragment impact zone is extracted and plotted with the fragment contact forces shown in Figure 4.29. The fragment loading demonstrated a more complex loading pattern, the multiple peaks witnessed in the force time history resulted from the different rows of fragments impacting the panel at slightly different time due to its launch trajectory, extending the loading time from 0.085 msec based on a single fragment to as long as 0.15 msec for the entire fragment mass. The actual fragment loading profile is expected to last for a longer duration due to the need to consider the longitudinal velocity distribution of the fragment along the charge which was omitted in this idealised model. The corresponding loading impulse is expected to be similar or less than the simulation as the fragments were modelled with the maximum velocities. Comparing the time of impact between the fragment and blast wave, at the close-in scaled distances tested, the fragments would

always arrive at the panel later than the blast wave, with a delay of about 0.1 msec consistently through the 3 simulations. The positive phase duration of the reflected blast wave can last about 0.25 to 0.35 msec, hence, the fragments are expected to strike the panel during the decay phase of the blast load. This results in a synergistic loading, highlighting the importance to consider their simultaneous loading in the analysis of these threats.

In this study, significant computational resource was required to simulate the coupled model due to the extreme mesh deformations resulting in extremely small timesteps. To simulate the post-blast quasi-static test, the simulation had to be continued significantly beyond the maximum deflection in order for the structure dissipate the residual stresses and come to a rest for the subsequent quasi-static loading simulation. Due to the limitation of computational resource this study was not conducted.

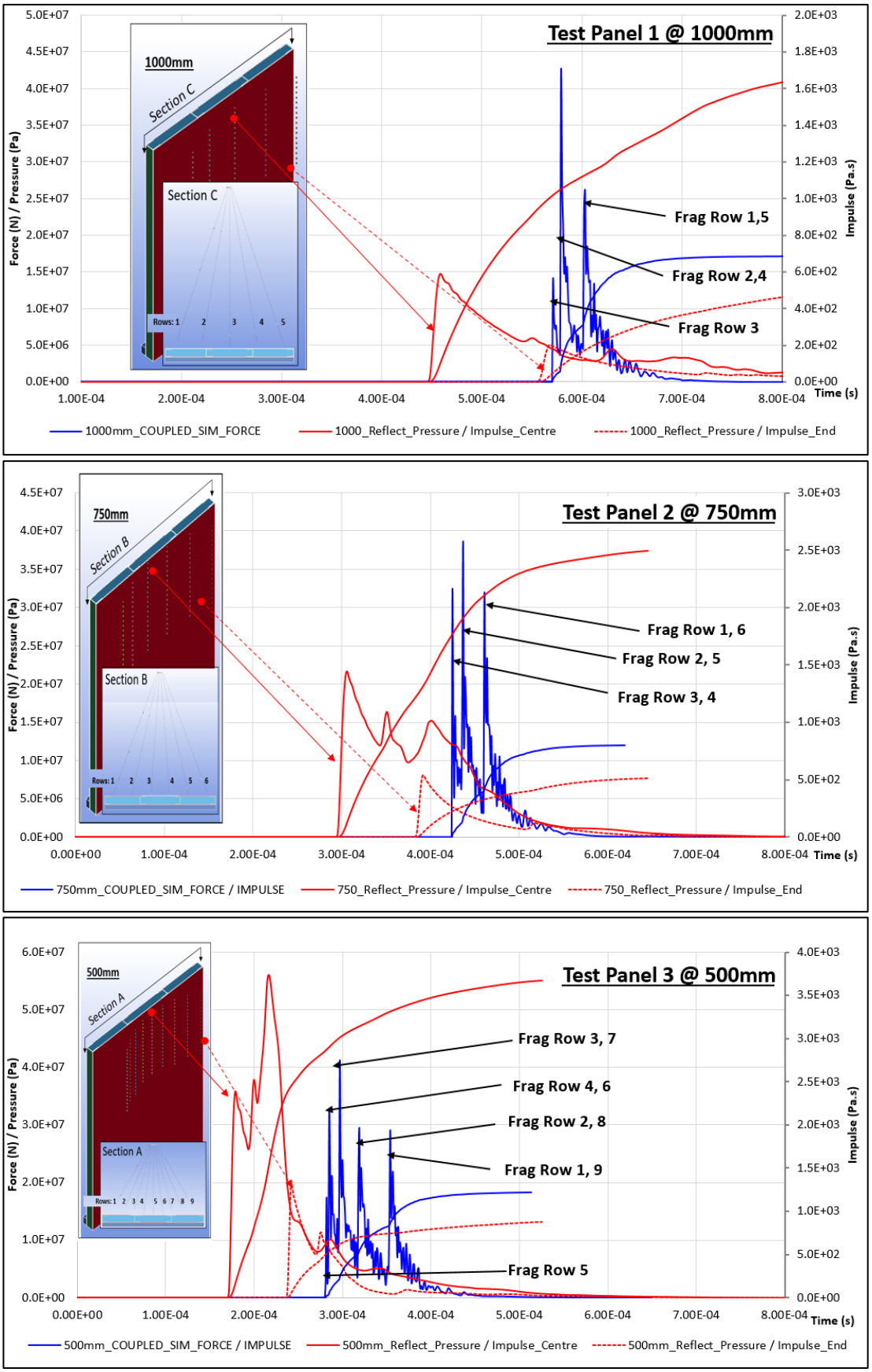

Figure 4.29: Resultant force time profile from fragment panel interface illustrating the fragment impact time against the blast application at different stand-off distances.

4.3. Simplified Numerical Model for SCC Panel Subjected to Combined Loading

The fully coupled model presented in Section 4.2.3 was able to accurately predict the fragment penetration behaviour, structural damage and maximum mid-span deformation reasonably well from the concurrent blast loading and fragment impact loading. However, large computational resource was required to compute the structural dynamic response which lasts about 30 msec simulation time in the study, owing to the extreme deformations generated from the fragment impact into the SCC panel. This has brought motivation for a methodology that simplifies the numerical analysis to estimate the maximum structural deformation of the panel during the panel's dynamic response to the combined loads. Hence, the analysis of the SCC panel to the combined loads can be performed in 2 phases, firstly, the penetration behaviour of the fragments on the panel can be investigated with the coupled model which typically requires a simulation time of less than 2 msec. Subsequently, the simplified method can be employed to investigate the maximum structural deformation from the combined loads to the necessary response time for the maximum deflection to occur, which is about 30 msec in this study. The generation of blast loads from coupled SALE and Lagrangian models is well established, hence, the focus of this study is the idealization of the fragment loads to loading impulses so they can be directly applied on panels. Based on the quasi-static point load tests and verification studies on the plastic bending resistance presented in the previous section, the section capacity of the SCC panels is mainly derived from the steel plates since the composite panels had no interface mechanical connectors between the steel and concrete. Additionally, since most fragment impact damage occurs within the concrete section, the overall dynamic response of the panel is believed to be minimally influenced by the damage in the concrete section and thus the proposed methodology ignores the fragment damage to the panel.

4.3.1. Idealization of Fragment Load

The derivation of the fragment load largely adopts the methodology proposed by Ek et al. (2009) and Grisaro et al. (2018), supplemented by the fragments impact pattern analysis quantified in the preceding Section 3.2.2. The force-time relationship of the fragment impulse is assumed as a rectangular impulse as shown in Figure 4.30 (Grisaro et al, 2018). In this study, the impact from the multiple fragment penetration is simplified as a single force impulse that is smeared uniformly across the impact surface. The peak pressure and

loading duration are conservatively derived based on the fastest fragment travelling along the shortest path. Due to the short differences in the time of arrival (< 0.1msec) refining the force-time history considering different fragment trajectories (and different time of arrival) was not studied as it was thought to have little influence on the structural response.

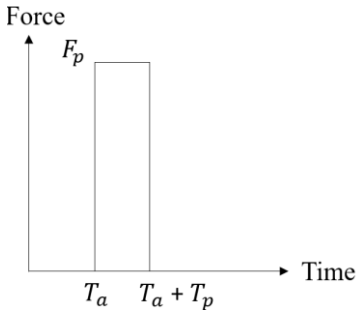

Figure 4.30. Illustration of rectangular force-time history for fragment impact

The arrival time of the fragments can be calculated from Equation (4.3), where V_o = fragment velocity (m/s) calculated by Gurney's equation presented in Equation (3.1) and R is the standoff distance of the charge to the panel. In this study arrival time was calculated based on the shortest path of the fragments.

$$T_a = \frac{R}{V_0} \tag{4.3}$$

For simplification, during the penetration process a constant deceleration of the fragment is assumed, the time the fragment takes to come to a full stop can be calculated from Equation (4.4) (Ek at al., 2009), where T_p = fragment penetration duration; x = total penetration depth which can be calculated by the sum of the penetration of the fragment in steel based on Equation (3.4) and penetration in concrete based on Equation (3.7) and V_s = striking velocity calculated from Equation (3.2).

$$T_p = \frac{2\,x}{V_s} \tag{4.4}$$

The deceleration a_f of the fragment can be determined by Equation (4.5)

$$a_f = \frac{{V_s}^2}{2x} \tag{4.5}$$

The peak force can be calculated from Equation (4.6), where M_f is the total mass of the fragments impacting the panel determined by Equation (3.14)

$$F_p = M_f\, a_f \tag{4.6}$$

The peak pressure to be applied on the panel can be determined from Equation (4.7) where fragment throw distance along the longitudinal axis of the charge l_f is calculated by Equation (3.11), where B represents the panel's width.

$$P_p = \frac{F_p}{l_f B} \tag{4.7}$$

A comparison of the fragment loads determined by the simplified methodology against the coupled simulations from Section 4.2.3 is presented in Figure 4.31 and summarised in Table 4.18. The fragment loading profile from the coupled simulations were significantly more complex with multiple peak forces, trailed by exponential decays while the simplified method described idealised the loads as rectangular impulses with a notably shorter application duration. This is primarily due to the simplification of the idealization of the fragment mass as follows; 1) assumption of a constant deceleration of the fragments upon penetration into the concrete core as described in Equation 4.4, and 2) the idealisation of the fragments as a global mass with a constant velocity as detailed in Equation 4.3, as compared to the discrete rows modelled in the coupled simulation. Despite this, the resultant force impulses applied on the panel is comparable and the rectangular loading assumption idealises a more conservative loading profile due to its shorter loading duration. The fragment impulse determined from the simplified method is slightly higher than the results extracted from the coupled simulations, with the largest difference of 16% at 750 mm. This is ascribed to the higher mass of the fragments determined from the simplified method as compared to the experimental results, as shown in Table 4.19. Hence, the simplified method proposed provides a conservative idealization of the fragment loading.

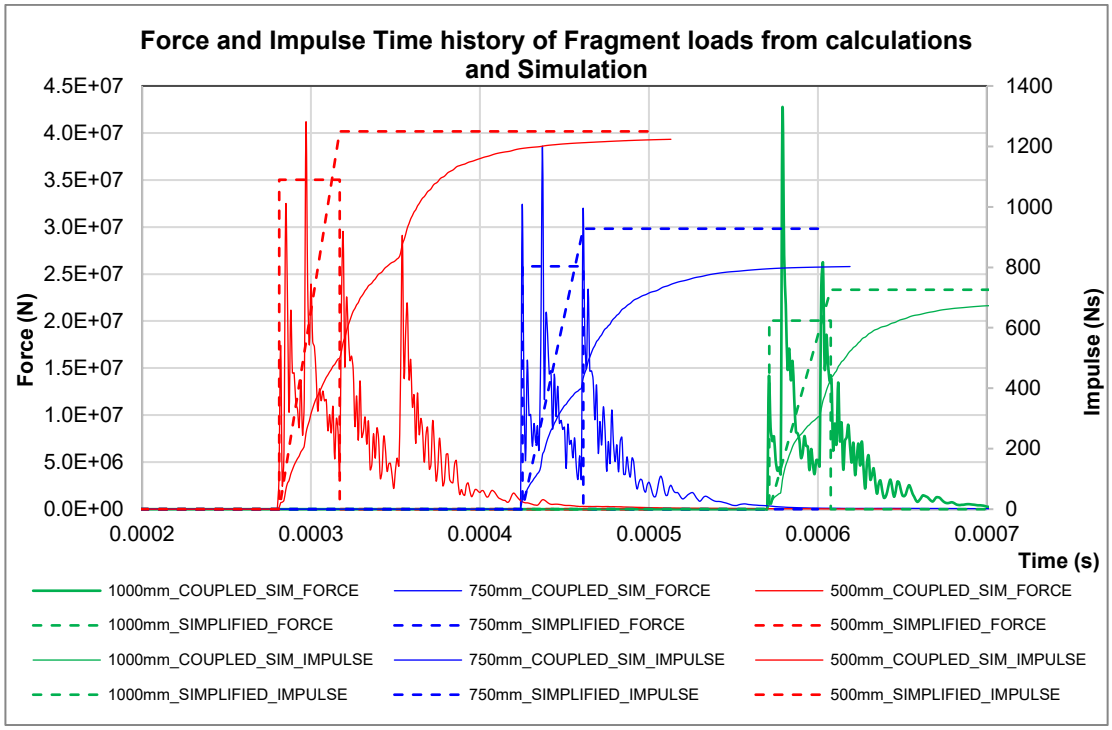

Figure 4.31: Force and impulse time history from the different simulations

Table 4.18. Comparison of Fragment impulse from the different simulations

Test panel	Distance from charge, R (m) / Z (m/kg1/3)	Fragment impulse (Ns)		Difference
		Coupled simulation	Simplified method	
1	1m (Z = 0.78)	688.4	725.9	5.4%
2	0.75m (Z = 0.58)	802.5	927.8	15.6%
3	0.5m (Z = 0.39)	1223.5	1249.8	2.1%

Table 4.19. Comparison of fragment mass from the different simulations

Test panel	Distance from charge, R (m) / Z (m/kg1/3)	Fragment mass (g)		Difference
		Coupled simulation	Simplified method	
1	1m (Z = 0.78)	380.1	414.7	9.1%
2	0.75m (Z = 0.58)	456.1	525.9	15.3%
3	0.5m (Z = 0.39)	684.2	702.5	2.7%

4.3.2. Dynamic Response to Concurrent Blast Loading and Fragment Impact

To simulate the concurrent blast loading and fragment impact on the composite panels, the fragment loading was applied as a smeared uniform load over the SCC panel with concurrent blast loading applied through the explosive modelled in the ALE environment. The idealized fragment loading is applied on the impact zone with module LOAD_SEGMENT_SET and the blast loads were simultaneously applied with the coupled SALE Lagrangian model, as presented in Section 4.2.2, as shown in Figure 4.32.

The concurrent application of the blast wave loading together with the fragment loading impulse within the fragment impact zone is displayed in Figure 4.33. In all three panels, the concurrent application of fragment load and blast wave replicates the actual loading conditions quite well at the centre of the panel, the fragment load is applied with a delay of about 0.1 msec to the blast loads. However, at the edges of the fragment impact zone, the delay of the fragment loads from the blast loads is smaller owing to the slightly larger stand-off distance for the blast wave. This delay reduces with increasing standoff distance, when the stand-off is 1000 mm, the fragment loads reached the panel about the same time as the blast wave.

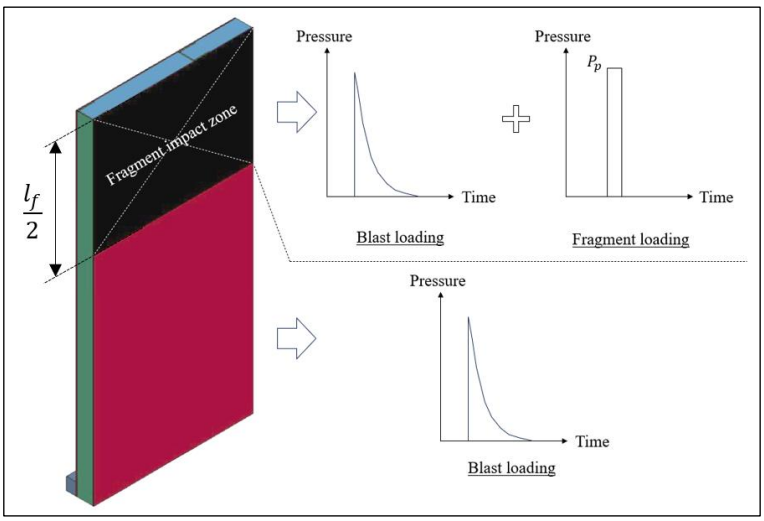

Figure 4.32. Illustration of the application of blast and fragment loads on SCC panel

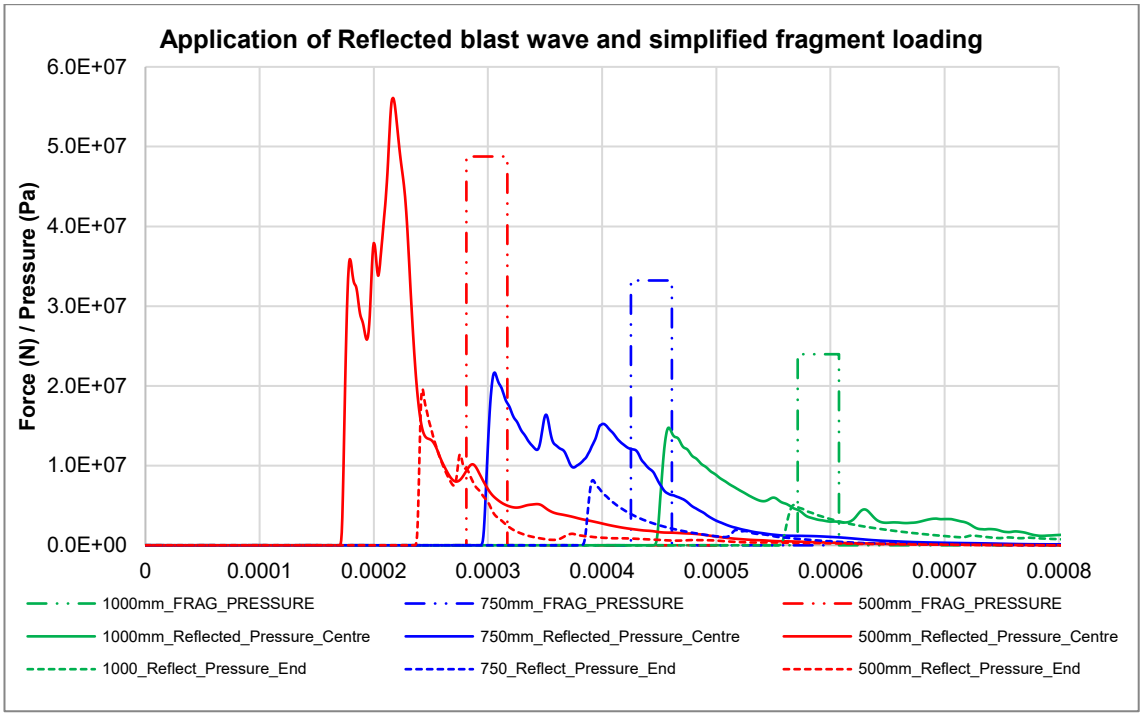

Figure 4.33: Illustration of fragment loading against blast pressure loading on the panel

The results of the maximum structural deformation from the simulations are presented in Figure 4.34 and summarized in Table 4.20. The simulation results show the maximum structural response matched well to the experimental data when the impulse from the fragment loading is included, with a difference of about 5% to 10% at all three different scaled distances. The time at the maximum structural deformation was predicted with similar accuracy with the maximum difference of 20% at a scaled distance of 0.58 m/kg$^{1/3}$. The proposed model was able to predict the change in the structural frequency from the damage of the panel accurately witnessed at the closest scaled distance of 0.39 m/kg$^{1/3}$. It was noted that the initial elastic deformations witnessed around 2-3 msec was not able to be replicated by the model due to the proposed smearing of the fragment loads across the panel and the absence of actual fragments impacting the panel.

Analysing the failure modes of the panel, the simulations similarly showed localized compression buckling behaviour on the panel's top steel plates. The localized buckling behaviour was however quite different, the top steel plates buckled with a significantly smaller critical length forming a distinctive fold across the panel at about 1/3 and 2/3 span length as shown in Figure 4.35. The buckling failure from the experiments and coupled simulations showed the steel plates formed two localized buckling failure zones symmetrical about the mid-span of panel across the fragment impact zone, likely due to the expansion of the concrete from the fragment impact, heaving the top plate away from the section. The segment loading methodology from the simplified approach is unable to replicate this behaviour, despite this, the structural response accurately predicted the maximum deflection at the midspan and the corresponding response time when compared with the experimental results. Analysing the concrete damage, the concrete at the mid-span was not as heavily damaged as witnessed in the coupled simulation models in both simulations from 0.58 m/kg$^{1/3}$ and 0.39 m/kg$^{1/3}$. About a quarter section of the concrete was still intact at the compression zone indicating an over prediction of the damage from the coupled models owing to the fragment impact.

The deceleration adopted in this methodology is simplified and assumes a constant linear deceleration through the penetration of the fragment to the section. The deceleration time is calculated based on a single fragment penetration assumption from UFC 3-340-02, to be about 0.031 msec. Comparing against the fully coupled blast and fragment impact simulation, the penetration of the multiple fragments into the panel is much deeper than that of a single fragment, moreover, the time extracted from the coupled models from

Section 4.2.3 is 0.085 msec, which is about 3 times longer than the calculated deceleration time. Additionally, the simulation shows a more complex exponential deceleration pattern, as compared to a constant deceleration assumption adopted in the simplified methodology. This suggests that the fragment loading in the simplified methodology proposed is conservative resulting in correspondingly conservative structural response despite not accounting for the material damage by the fragment impact.

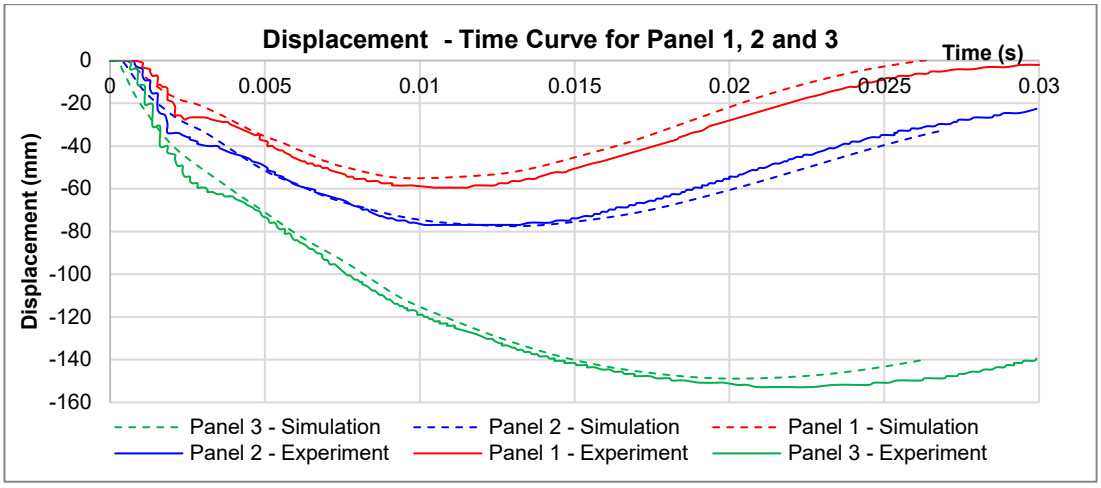

Figure 4.34. Structural response of the coupled simulation against experimental results

Table 4.20. Summary of structural response from experiments against simulations with blast and fragment loads

Test panel	Distance from charge, R (m)	Max mid-span deflection (mm)			Time at max deflection (msec)		
		Exp	Sim	Difference	Exp	Sim	Difference
1	1m	60	55.1	-8.2%	11	9.8	-10.9%
2	0.75m	78	77.5	-0.6%	11	13.0	18.2%
3	0.5m	153	148.9	-2.7%	21	20.2	-8.2%

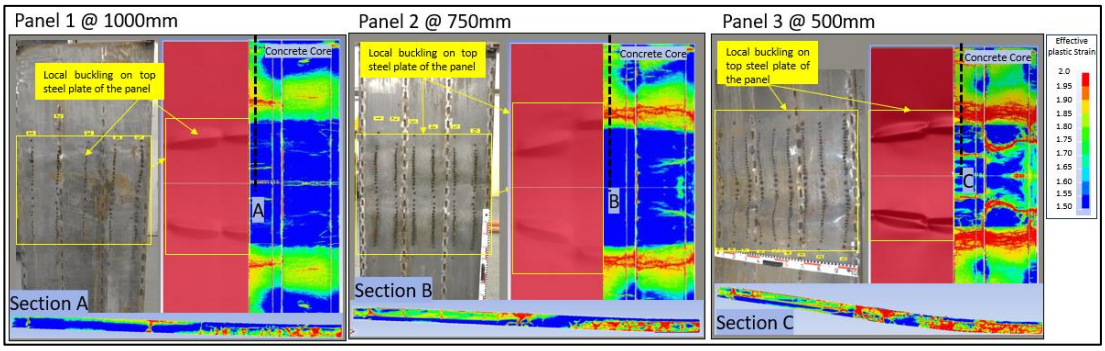

Figure 4.35: Comparison of damage mode from simulation results against experimental test for Panel 1, 2 and 3

4.3.3. Investigation of Independent Application of Blast and Fragment Loads

To investigate the synergy of the concurrent blast loading and fragment impact to the structural response, a sensitivity analysis was performed subjecting the panel to the blast and fragment loads independently, summing the deflections and comparing them against the experimental results. The simulation was performed by applying the fragment loading impulse independently on the SCC panel, subsequently, the structure deformation profile was added to that from the simulations that subjected the panel to bare cylindrical charges only from Section 4.2.2. The resultant structural deformation profile is shown in Figure 4.36 and summarized in Table 4.21.

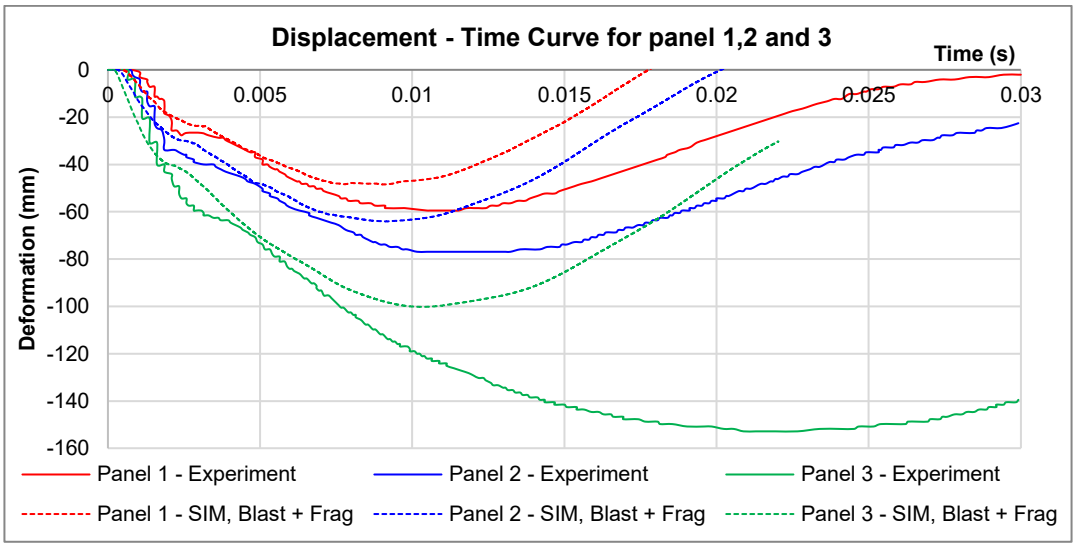

Figure 4.36: Structural response of simulations from independent application of blast and fragment loads against experimental results

Table 4.21. Summary of structural response from experiments against simulations with independent application of blast and fragment loads

Test panel	Distance from charge, R (m)	Max mid-span deflection (mm)			Time at max deflection (msec)		
		Exp	Sim	Difference	Exp	Sim	Difference
1	1m	60	48.5	-19.2%	11	9.1	-17.6%
2	0.75m	78	64.1	-17.8%	11	9.2	-16.8%
3	0.5m	153	100.2	-34.5%	21	10.3	-50.8%

The results show that the max deflections and respective time of the response of the panels are consistently underestimated by about 17% to 35% and 17% to 50%, respectively, the difference was the largest when the scaled distance was the closest at 0.39 m/kg$^{1/3}$. The results show that the independent application of the fragment and blast loads did not accurately capture the damage mode in the panel. This was witnessed by the significant

change in the structural period at the closest standoff in the experimental results, while the simulation returned similar structural periods for all three analyses.

This highlights the synergistic damage potential of the combined loads and the importance of true simultaneous blast and fragment load application in the structural analysis for accurate response results.

4.4. Optimisation Studies for the Composition of the SCC Panels

Optimisation studies on the configuration of built up of the SCC panels were conducted numerically to investigate the optimal built up of the panel. The panels were first compared against conventional steel sandwich panel with a hollow core, and subsequently the concrete section was varied using different grades of concrete from high strength concrete (HSC) and ultra high-performance concrete (UHPC). The numerical studies conducted adopted the same approach as presented in Section 4.2.3 with loading conditions like the panel at 500 mm.

4.4.1. Comparison Against Steel Sandwich Panels

To explore the effectiveness of the concrete core, the study was first performed with a hollow sandwich panel, to investigate its performance against combined blast and fragment loads as shown in Figure 4.37. The simulation adopted the same approach as presented in Section 4.2.3, except the concrete parts, contacts and material cards were removed.

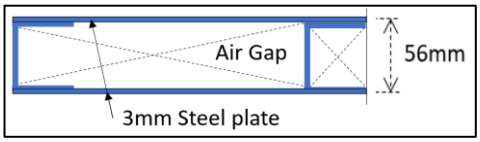

Figure 4.37. Section schematic of the steel sandwich panel

The simulation showed that due to the lack of a concrete core, the fragments perforated through both steel plates and exited the panel with significant residual velocity that was about half the strike velocity. The panel experienced total failure, there was significant structural deformation such that it was dislodged from its supports. Along its mid span, the C-channel stiffener beams experienced web buckling failure, crushing in on itself at the midspan evidenced by distinct folding of the web on itself. The top steel plates similarly experienced localised failure, caving into the panel at the stiffener supports, as shown in Figure 4.38. Without the concrete core, not only was the fragment penetration capability lost, the restraints for the steel members were also compromised subjecting

them to localised failure, hence compromising on its performance in blast loading environment.

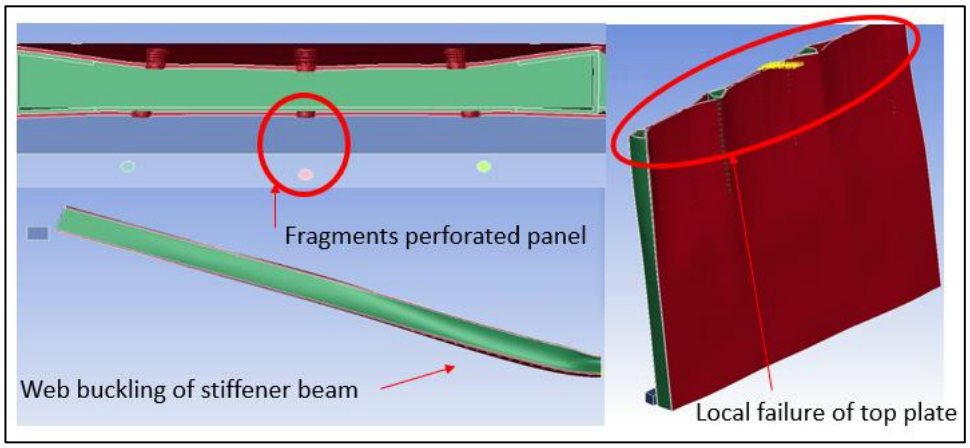

Figure 4.38. Simulated response of the hollow sandwich panel to the combined loading.

To provide an equivalent protective capability of the steel panel for an equal comparison, the top steel plate was thickened such that the fragment would not perforate leaving the bottom plate intact, like the experimental results from the SCC panels. To achieve the similar protective capability in the simulation model, the steel plate thickness was increased by iterating in gradual increments of 1.5 mm following the mesh size of a single element until the fragment would not perforate the top steel plate. The study concluded that a 15 mm plate thickness was required to prevent perforation of the fragments, making the total thickness of the steel plates required to be about 18 mm, the schematic and fragment protective capability is shown in Figure 4.39.

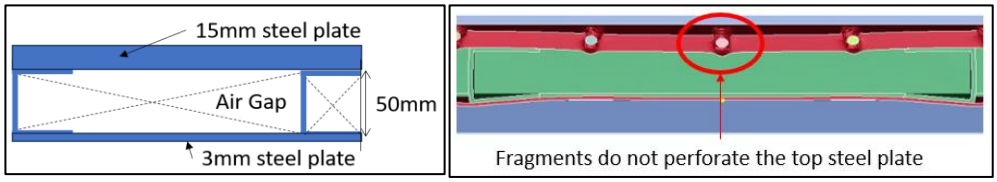

Figure 4.39. Schematic of the steel sandwich panel with equivalent protective capability (left) and illustration of fragment protective capability (right)

Next, an optimised design for the steel panels, where the design of the steel plates was iterated such that, the fragment was allowed to perforate the first steel plate and penetrate but not perforate the second steel plate. Both the top and bottom steel plates were thickened equally to obtain a balanced section design for optimal bending resistance. Like the previous study, the steel sections iterated by increasing the thickness of the plate, from 3 mm each, by steps of 1 mm until the fragment does not perforate the bottom steel plate. The study showed that a plate thickness of about 8 mm each was required to prevent

fragment perforation through the panel, the section of the optimised panel and fragment protective capability is shown in Figure 4.40.

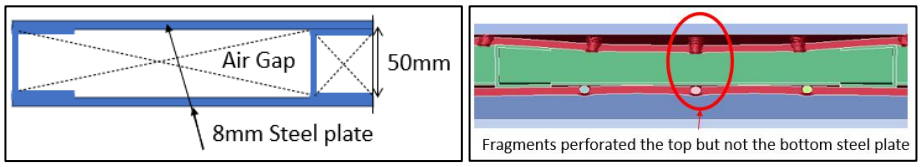

Figure 4.40. Schematic of the optimised steel sandwich panel (left) and illustration of fragment protective capability (right)

The structural response results are presented in Figure 4.41 and summarized in Table 4.22, proving the superior performance of the steel sandwich panels to the combined loads. The panels no longer exhibited the weakness of local failure of the steel sections due to the thicker steel plates. The maximum structural deformation was 102 mm for the optimised configuration which was about 50% lesser than what is expected from the SCC panel. The corresponding degree of rotation is about 5.7º which is well below the recommended maximum 12º rotation from UFC 3-340-02 but above the 2º criterion for serviceability of the panels that in blast door application. This indicates that the blast performance is superior but not good enough for use in serviceability without additional artificially thickening the panel. Additionally, the structural deformation of about 6º indicates that the steel panel can be optimised further to allow for more structural deformation indicating a possible leaner plate configuration. However, owing to the need to prevent the fragments from perforating the panel, further optimisation of the plate thickness is not feasible. This highlights the superior blast resistance of steel as compared to its relative weakness with regards to fragment / projectile penetration resistance. Additionally, the natural period of the steel panels was about half of the SCC panel due to the stiffer setup of the panel.

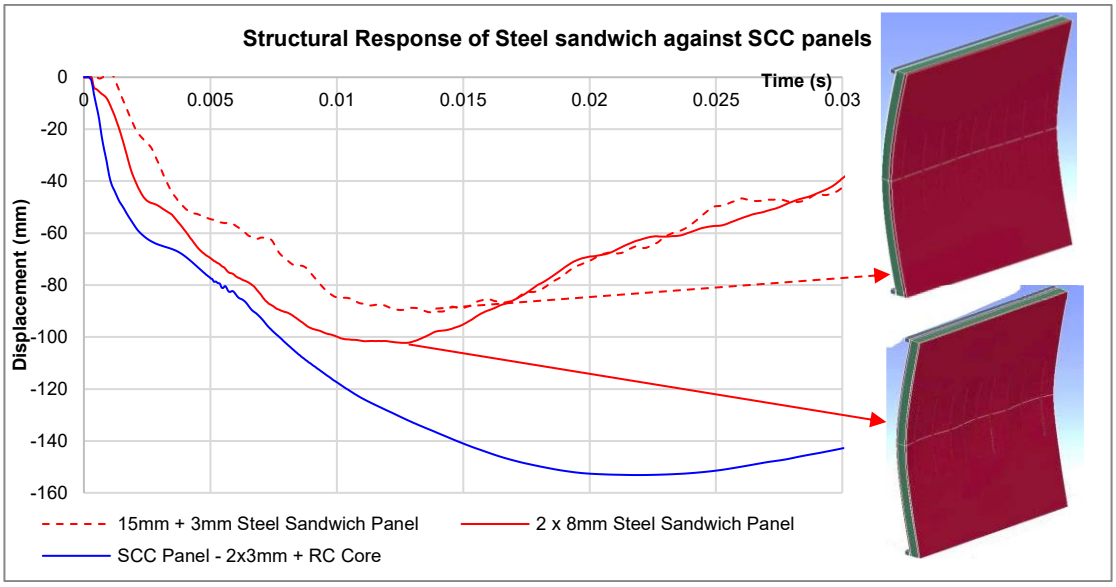

Figure 4.41. Simulation results of the different configuration of steel sandwich panels to the combined loading.

Table 4.22. Summary of structural response from the panel arrangement optimisation study

	SCC panel	2 x 8mm Steel Sandwich panel	Difference	15mm + 3mm Steel Sandwich panel	Difference
Max mid-span deflection (mm)	153	102	-50%	90	-70%
Time of max deflection (msec)	22	13	-68%	13	-68%

Comparing the optimised steel panel against the SCC panels, the concrete core within the sandwich panel significantly improved the penetration resistance of the panel. The concrete core further provides restraint to the steel plates mitigating local plate failures at both the stiffener beams and the steel plates, allowing a lean configuration of the steel plates as required by the anticipated blast effects and accompanying fragment impulse. This is shown in the larger structural deformation of the SCC panel, showing the design flexibility of the SCC panels against simultaneous blast and fragment threats. Another merit of the concrete core is its added mass to the system reducing the natural frequency, hence more likely to respond to blast loading in an impulse loading regime rather than in a dynamic loading regime which significantly reduces the structural response, improving the blast resistance of the panel. The SCC panels also allow the designer to customise the concrete thickness as required from the anticipated fragment threats while maintaining a lean steel plate design, whereas a similar protective panel using steel only would incur a weight penalty due to the need for a large minimum steel thickness for penetration

resistance, driving up fabrication costs of the sandwich panels. With the same protective capability, the SCC panels require at least half the steel weight as compared to its steel counterpart, again potentially saving fabrication costs of the panels. However, it should be noted that the SCC panels would likely be thicker and heavier due to the need for the concrete depth and thus associated mass concrete to mitigate fragment penetration effects. In this example, when comparing the panels with equivalent protective capability, the SCC panels is about 40% heavier than the steel panel. Hence, the SCC panel is recommended for most protective engineering applications, however, if there is a need for quick mobility of these panels such that weight of the panel becomes critical to its movement, a full steel sandwich panel is recommended.

4.4.2. Study of Influence of Strength of Concrete Core

Next, the sensitivity of the concrete's strength influence to the performance of the panel to blast and fragment loads was investigated. The concrete core was varied from grade 35 normal strength concrete (NSC), to grade 70 high strength concrete (HSC) and finally grade 140 Ultra high-performance concrete (UHPC). Similar to the study from Section 4.2.3, the concrete was idealised with the RHT model for this sensitivity study. The material parameters for the HSC and UHPC were achieved using the default parameter generation function on the RHT material model where the model iterates between parameters calibrated from Grade 35 and Grade 140 strength concrete as presented in Riedel (2004), with a similar erosion criterion of 2. Like the previous optimisation study, the numerical studies conducted adopted the same approach as presented in Section 4.2.3 with loading conditions as panel at 500 mm.

The penetration resistance of the panels is shown in Figure 4.42 and summarized in Table 4.23. The structural response is shown in Figure 4.43 and summarized in Table 4.24. The HSC and UHPC panels displayed significant improvement in penetration performance, reducing the fragment penetration depth by 27% to 31%. While the simulation of the fragments penetrated the entire section of NSC panel almost reaching the bottom steel plate, the fragments penetrated less than half of the section of the high strengths concrete indicating that there was significant penetration resistance left in the section and the section could potentially be optimised further. Comparing the penetration resistance, the fragment penetration within the UHPC panel was marginally smaller at about 13% difference from the HSC panel, the UHPC panel also displayed less material expansion

absorbing the fragment impact energy. However, this marginal difference indicates that the optimal penetration resistance is offered with the HSC panel.

Comparing the structural response, all three simulations gave similar maximum deflections that is within 15% difference from the NSC panel. The use of UHPC improved the peak structural deformation by about 12% due to its superior strength properties, additionally, the buckling of the top compression plates showed a diagonal buckling pattern about the centre of the panel as compared to the linear buckling pattern near the mid span shown in the NSC and HSC panels, improving the deformation response. The use of HSC core did not improve the structural response, the structural response and failure modes largely remained the same as the NSC core. The marginal difference in the structural response is likely attributed to the bending resistance of the section was contributed largely by the steel plates, as studied in Section 4.3, since there was no composite action with the concrete core as they were not mechanically attached to the steel plates.

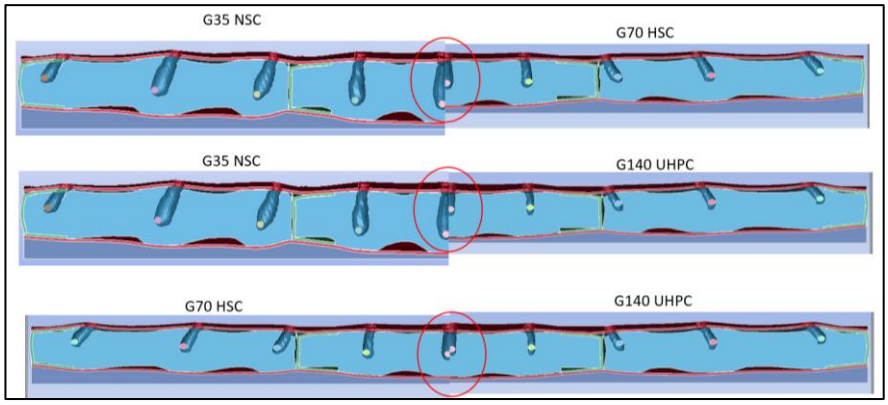

Figure 4.42: Comparison of the penetration performance of NSC, HSC and UHPC.

Table 4.23. Summary of penetration response from the optimisation study

	SCC Panel Type		
	NSC (baseline)	HSC	UHPC
Penetration depth (mm)	41	31 (-24%)	27 (-34%)

() difference to NSC panel

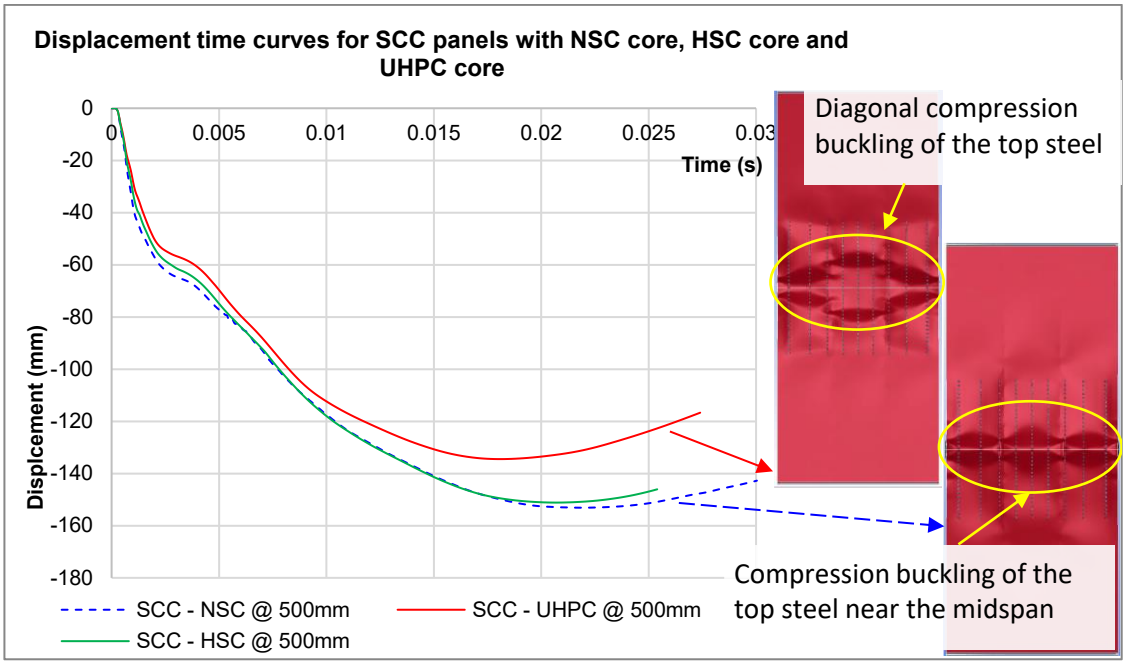

Figure 4.43. Deformation results of the SCC panels with NSC, HSC and UHPC.

Table 4.24. Summary of structural response from concrete core strength optimisation study

	SCC Panel Type		
	NSC (baseline)	HSC	UHPC
Max mid-span deflection (mm)	153	151 (-1%)	134 (-12%)
Time of max deflection (msec)	22	21 (-5%)	18.5 (-16%)

() difference to NSC panel

This study proves the use of SCC panels offers an efficient and effective protective solution against simultaneous blast and fragment impact loads. The presence of a concrete core allows the design of the section thickness required for the fragment penetration resistance to be decoupled with the steel plate thickness required for the dynamic bending response, providing design flexibility and efficiency in material usage. In a highly hazardous environment where fragmentation is a concern, the designer may consider the use of a higher strength concrete core for superior penetration resistance, noting that a superior concrete core does not significantly influence the peak dynamic deflection magnitudes. The use of a SCC panel design however comes with a weight penalty of about 40% as compared to conventional protective deign with steel sandwich panels. The effectiveness of a stronger concrete core against fragment penetration is recommended to be verified with future studies with heavier fragment densities at closer stand-off distances.

4.5. Summary

Numerical studies were performed to study the response of SCC panels that were exposed to the combined loads from a cased charge to evaluate the damage synergy to the panel at close-in loading regimes. A validated numerical model of the charge was presented that characterized the blast loading parameters. Subsequently the structural response and damage modes of the SCC panel from the concurrent application of blast loading and fragment impact was simulated and analysed. Finally, to optimize computational efficiency, a simplified method was proposed to idealize the fragment load on the SCC panel to obtain the maximum structural deformation. A summary of the findings is as follows:

1. Numerical studies analysing structural response to blast loads from bare cylindrical charges alone severely underestimated the structural response, emphasizing the need to consider the fragment loading in scenarios of close-in loading regimes.
2. A coupled simulation model proposed that incorporated the fragment impact was able to replicate the structural response well. The model was able to predict the structural response reasonably at the closest and furthest scaled distance of 0.78 and 0.39 m/kg$^{1/3}$, however, at scaled distance of 0.58 m/kg$^{1/3}$ the response was over-predicted, likely due to the use of rigid material model for the fragments, and the damage in the panel was over-predicted resulting in a similarly conservative structural response prediction. When analysing the penetration damage from multiple fragment impact, the RHT material model used in the panel was able to predict the penetration response of multiple fragments on the panel well that matched the experimental results.
3. A simplified methodology incorporating the fragment loads idealized as a smeared uniform loading across the fragment impact zone applied on a pristine SCC panel to estimate the maximum structural deformation was proposed. Although the damage mode in the steel plates and concrete was not precisely replicated, the simulation was able to predict the structural response quite well at all three scaled distances with a difference in the max deflection of about 10%. Despite the good results obtained by the model, it is acknowledged that the fragment deceleration during the penetration is simplified to a constant and the

structural damage from the fragments impact is not considered in the numerical model. Further studies are required to accurately quantify the blast loads and material damage into the numerical solution.

4. The summation of the structural response from the independent analysis of the blast and fragment loads grossly underestimates the maximum deflection from the simultaneous application of the combined loads. This highlights the synergistic damage potential of the combined loads and the importance of their simultaneous application in the structural analysis for accurate response results.
5. Optimization studies performed proved that SCC panels offer an efficient and effective protective solution against simultaneous blast and fragment impact loads as compared to conventional steel protective panels. The presence of a concrete core allows the design of the section thickness required for the fragment penetration resistance to be decoupled with the steel plate thickness required for the dynamic bending response, providing design flexibility and efficiency in material usage. The study also indicated use of a higher strength concrete core yielded superior penetration resistance. Its effectiveness is recommended to be verified with future studies with heavier fragment densities at closer stand-off distances.

The findings reported are limited to the study of SCC panels exposed to cased explosive charges that yields a maximum fragment mass and density of 2.1g and 1.12kg/m^2 respectively, loaded at loaded at a minimum of 0.39m/kg$^{1/3}$ scaled distance. Alternative heavier case to explosive ratios tested at closer scaled distance is recommended for future studies to verify the performance of the panels to the impact of fragment clusters with higher mass densities and the applicability of the proposed numerical methods.

5. CONCLUSION

In this study, the dynamic response of SCC panels to simultaneous blast loading and fragment impact was explored to evaluate the synergistic effects of combined loading at close-in scaled distances. An experimental program which comprised 3 phases (charge characterization tests, field blast tests, and quasi-static tests) was conducted to meet this objective. The experimental results were quantified analytically. A validated numerical model of the charge was presented that characterized the blast loading parameters. Subsequently the structural response and damage modes of the SCC panel from the concurrent application of blast loading and fragment impact was simulated and analysed. Finally, to optimize computational efficiency, a simplified method was proposed to idealize the fragment load on the SCC panel to obtain the maximum structural deformation. The key conclusions are as follows:

- The experimental results from the field blast test exhibited significant structural deformation of the panels. Post-test analysis revealed that the panels were not only damaged by the blast wave, but remarkable damage was caused by the high-density fragment penetration. Despite significant damage to the concrete core and the extreme deformation experienced, the steel concrete composite panels maintained their structural integrity and proved their performance in explosive environments generated from cased charges at close-in standoff distances.
- The field test demonstrated that the panels exhibited significant increase in the deflection when the scaled distance from the cased charge reduced. This was evident at scaled distance 0.39 m/kg$^{1/3}$ where the longer structural response time indicated that the natural frequency of the panel was altered by the damage in the panel. Additionally, the residual capacity derived from quasi-static load tests exhibited remarkable reduction in the panel's section capacity owing to the fragment damage, however, the panel was able to retain its plastic phase over a larger deformation than its pristine counterpart. The damage on the top face plate and in the concrete by the fragments most likely resulted in asymmetricity in stress distribution under static loading. Instead of inducing stress concentration at the mid-span, the stress was distributed over a larger area across the span of the panel under the three-point bending test.
- The results from quasi-static test on the SCC panels indicated that there was stiffness and strength degradation on the SCC panels that were damaged owing to the blast and fragment impact at close-in scaled ranges. The primary failure occurred through

compressive buckling failure at the top steel plates, mainly due to the lack of interface connectors between the steel plates and concrete infill, causing delamination of the steel plates rendering it more susceptible to local buckling failure once stresses went beyond elastic regime.

- The results from the fragment impact patterns and mass analysis were quantified well by analytical methods. However, the results from the penetration analysis of a single fragment as compared to multiple simultaneous fragment impact in the experiment was significantly different. Most notably, the concrete was not expected to perforate in a single fragment analysis, however, in the experiment fragments were found at the face of the rear steel plate indicating the concrete section was perforated. In addition, the craters from multiple fragment impact merged to form a large crater.
- Numerical studies analysing structural response to blast loads from bare cylindrical charges alone severely underestimated the structural response, emphasizing the need to consider the fragment loading in scenarios close-in loading regimes.
- A coupled simulation model proposed that incorporated the fragment impact provided a reasonably conservative prediction of the structural response. The model was able to predict the structural response at the closest and furthest scaled distance of 0.78 and 0.39 m/kg$^{1/3}$, however, at scaled distance of 0.58 m/kg$^{1/3}$ the response was over-predicted, likely owing to the use of rigid material model for the fragments, the damage in the panel was over-predicted resulting in a similarly conservative structural response prediction. When analysing the penetration damage from multiple fragment impact, the RHT material model used in the panel was able to predict the penetration response of multiple fragments on the panel well that matched the experimental results.
- A simplified methodology incorporating the fragment loads idealized as a smeared uniform loading across the fragment impact zone applied on a pristine SCC panel to estimate the maximum structural deformation was proposed. Although the damage mode in the steel plates and concrete was not precisely replicated, the simulation was able to predict the structural response quite well at all three scaled distances with a difference in the max deflection of about 10%. It is acknowledged that the fragment deceleration during the penetration is simplified to a constant and the structural damage from the fragments impact is not considered in the numerical model.
- The summation of the structural response from the independent application of the blast loads and fragment impulse loads grossly underestimates the maximum deflection

from the simultaneous application of the combined loads. This highlights the synergistic damage potential of the combined loads and the importance of their simultaneous application in the structural analysis for accurate response results.

- The use of SCC panels offers an efficient and effective protective solution against simultaneous blast and fragment impact loads. The presence of a concrete core allows the design of the section thickness required for the fragment penetration resistance to be decoupled with the steel plate thickness required for the dynamic bending response. The use of a higher strength concrete core improves the penetration resistance of the panel although the dynamic bending response is largely similar.

The conclusions of this study are limited to steel concrete composite panels subjected to cased explosive charges at close-in loading regimes at the closest stand-off distance of 0.39 $m/kg^{1/3}$, with the maximum fragment density of 1.12 kg/m^2 and maximum single fragment mass of 2.1 g. Future studies are recommended using different ratios of mass of case to mass of charge with a higher maximum single fragment mass at similar close-in standoff distances to investigate the survivability of these steel concrete composite panels to extreme explosive loading environment and the applicability of the numerical studies concluded.

Further studies are also recommended to understand the fragment penetration damage on the strength of the panel. The quantification of the damage of concrete from the multiple fragment impact and its influence on the panel's residual section capacity and resultant enhanced plastic phase are key areas of focus recommended. Subsequently, with the quantified material damage from the fragment impact, integration into the simplified numerical solution proposed for a complete representation of the structural response.

REFERENCES

1. Anandavalli, N., Lakshmanan, N., Rajasankar, J., & Prakash, A. (2012). Numerical studies on blast loaded steel-concrete composite panels. *J. Community Engagem. Scholarsh*, *1*(3), 102-108.
2. Attard, M. M., & Setunge, S. (1996). Stress-strain relationship of confined and unconfined concrete. *Materials Journal*, *93*(5), 432-442.
3. Biggs, J. M. (1964). Introduction to structural dynamics. *McGraw Hill, New York*.
4. Borrvall, T., & Riedel, W. (2011, May). The RHT concrete model in LS-DYNA. In *Proceedings of The 8th European LS-DYNA user conference* (pp. 23-24).
5. Brode, H. L. (1959). Blast wave from a spherical charge. *The Physics of Fluids*, *2*(2), 217-229.
6. Bruhl, J. C., & Varma, A. H. (2018). Experimental evaluation of steel-plate composite walls subject to blast loads. *Journal of Structural Engineering*, *144*(9), 04018155.
7. Bruhl, J. C., Varma, A. H., & Kim, J. M. (2015). Static resistance function for steel-plate composite (SC) walls subject to impactive loading. *Nuclear Engineering and Design*, *295*, 843-859.
8. Burchfield, C., French, R., Jaberi, B., Kim, J., Maher, E., Tsai, J., & Krauthammer, T. (2014). P43 Assessing the Capabilities to Predict Combined Blast and Fragment Effects.
9. Cai, S., Liu, J., Zhang, P., Li, C., Cheng, Y., & Chen, C. (2021). Experimental study on failure mechanisms of sandwich panels with multi-layered aluminum foam/UHMWPE laminate core under combined blast and fragments loading. *Thin-Walled Structures*, *159*, 107227.
10. Chen, Z., Zong, Z., Li, J., Li, J., Yan, Y., & Wu, C. (2024). Experimental and numerical study on damage behavior of air-backed steel-concrete-steel composite panels subjected to underwater contact explosion. *Engineering Structures*, *318*, 118744.

11. Chen, L., Hu, Y., Ren, H., Xiang, H., Zhai, C., & Fang, Q. (2019). Performances of the RC column under close-in explosion induced by the double-end-initiation explosive cylinder. *International Journal of Impact Engineering*, *132*, 103326.

12. Comité Euro-International du Béton. (1993). CEB-FIP model code 1990: Design code. Thomas Telford Publishing.

13. CEN, 2000, Concrete-Part 1: Specification, performance, production and conformity. EN 206-1, European Committee for Standardization (CEN).

14. CEN, (2010), Eurocode 2 Design of concrete structures — part 1-1: general rules and rules for buildings, BS EN 1992-1-1, European Committee for Standardization (CEN).

15. CEN, 2009, Eurocode 3 Design of steel structures—part 1-1: general rules and rules for buildings, BS EN 1993-1-1, European Committee for Standardization (CEN).

16. Charron, Y. J. (1979). *Estimation of velocity distribution of fragmenting warheads using a modified gurney method* (Doctoral dissertation, Air Force Institute of Technology).

17. Chen, L., Hu, Y., Ren, H., Xiang, H., Zhai, C., & Fang, Q. (2019). Performances of the RC column under close-in explosion induced by the double-end-initiation explosive cylinder. *International Journal of Impact Engineering*, *132*, 103326.

18. Crawford, J. E., & Malvar, L. J. (2006). User's and theoretical manual for K&C concrete model. *Rep. TR-06*, *19*.

19. Crowley, A. B. (2006). The effect of munition casings on reducing blast overpressures. *Gas*, *100*, M21.

20. Crawford, J. E., Magallanes, J., & Zhang, Y. (2010). Determining the effects of cased explosives on the response of RC columns. In *21th international symposium on military aspects of blast shock (MABS 21), Jerusalem, Israel, Israel*.

21. Curran, D. R. (1997). Simple fragment size and shape distribution formulae for explosively fragmenting munitions. *International journal of impact engineering*, *20*(1-5), 197-208.

22. Del Linz, P., Fan, S. C., & Lee, C. K. (2016). Modeling of combined impact and blast loading on reinforced concrete slabs. *Latin American Journal of Solids and Structures*, *13*, 2266-2282.

23. Del Linz, P., Fung, T. C., Lee, C. K., & Riedel, W. (2021). Response mechanisms of reinforced concrete panels to the combined effect of close-in blast and fragments: An integrated experimental and numerical analysis. *International Journal of Protective Structures*, *12*(1), 49-72.

24. Del Linz, P., Rana, M. M., Khan, A., Fung, T. C., & Lee, C. K (2018). DYNAMIC AND QUASI STATIC MODELLING OF A SANDWICH STRUCTURE LOADED WITH A CASED CHARGE.

25. DoD (2008), *Structures to Resist the Effects of Accidental Explosions*. Unified Facilities Criteria (UFC) 3-340-02, United States of America Department of Defence (DoD).

26. Ek, K. J., & Mattsson, P. (2009). Design with Regard to Blast-and Fragment Loading.

27. Elfving C. (1995). The effect of ground reflection (in Swedish), FOA-R-95-00135- 6(2.6)-SE, National Defence Research Establishment.

28. Fisher, E. M. (1953). The effect of the steel case on the air blast from high explosives. *NAVORD report*, *2753*.

29. Forsén, R., (2015), *Response to RC Slabs Subjected to Combined Blast and Fragment Loading,* The 5th International Conference on Design and Analysis of Protective Structures, DAPS 2015.

30. Forsén, R., & Nordström, M. (1992). Damage to reinforced concrete slabs due to the combination of blast and fragment loading. In *Structures Under Shock and Impact II: Proceedings of the Second International Conference, held in Portsmouth, UK, 16th–18th June, 1992* (pp. 509-520). Thomas Telford Publishing.

31. Forrestal, M. J., Frew, D. J., Hanchak, S. J., & Brar, N. S. (1996). Penetration of grout and concrete targets with ogive-nose steel projectiles. *International Journal of Impact Engineering*, *18*(5), 465-476.

32. Girhammar, U. A. (1990). Brief review of combined blast and fragment loading effects. FortF.

33. Grisaro, H. Y., & Dancygier, A. N. (2019). Representation of damage caused by fragmentation impact in design and analysis of reinforced concrete barriers. *Engineering Structures*, *197*, 109387.

34. Grisaro, H. Y., & Dancygier, A. N. (2018). Characteristics of combined blast and fragments loading. International Journal of Impact Engineering, 116, 51-64.

35. Grisaro, H. Y., Benamou, D., & Dancygier, A. N. (2018). Investigation of blast and fragmentation loading characteristics–field tests. *Engineering Structures*, *167*, 363-375.

36. Gurney, R. W. (1943). *The initial velocities of fragments from bombs, shell, grenades* (p. 11). Aberdeen Proving Ground, MD: Ballistic Research Laboratories.

37. Guo, Q., Chen, Q. W., Xing, Y., Xu, Y. N., & Zhu, Y. (2020). Experimental Study of Friction Resistance between Steel and Concrete in Prefabricated Composite Beam with High-Strength Frictional Bolt. *Advances in Materials science and Engineering*, *2020*(1), 1292513.

38. Hallquist, J.O. (2006). LS-DYNA Theory Manual, Livermore Software Technology Company, Livermore CA.

39. Hader, H. (1983, May). Effects of bare and cased explosive charges on reinforced concrete walls. In *Symposium Proceedings, The Interaction of Non-Nuclear Munitions with Structures (US Air Force Academy, Colorado), May* (pp. 10-13).

40. Hao, Y., & Hao, H. (2014). Influence of the concrete DIF model on the numerical predictions of RC wall responses to blast loadings. *Engineering Structures*, *73*, 24-38.

41. Helte A., Lundgren J., Örnhed H., Norrefeldt M. Evaluation of performance of m/46 (in Swedish), FOI-Re2051-SE, Swedish Defence Research Agency 2006.

42. Heng, L., Kennedy, L. J., & Mays, G. C. (1995). Blast resistance of fully enclosed steel-concrete-steel sandwich panels. In *7th International Symposium on Interaction of the Effects of Munitions with Structures* (pp. 189-197).

43. Held, M., & Tan, G. E. B. (2003, May). Radial blast loads of confined cylindrical charges. In *11th International Symposium on Interaction of the Effects of Munitions with Structures*.

44. Holmquist, T. J., & Johnson, G. R. (1993). A computational constitutive model for concrete subjected to large strains, high strain rates and high pressures. In: M. Murphy and J. Backofen (eds), 14th International Symposium on Ballistics, Quebec, 1993, pp. 591- 600.

45. Hutchinson, M. D. (2009). The escape of blast from fragmenting munitions casings. *International journal of impact engineering*, *36*(2), 185-192.

46. Hyde, D., (1992), Conventional Weapon Effects Software (ConWep), U. S. Army Engineer Waterways Experiment Station (USAEWES).

47. Johnson, G. R., & Cook, W. H. (1985). Fracture characteristics of three metals subjected to various strains, strain rates, temperatures and pressures. *Engineering fracture mechanics*, *21*(1), 31-48.

48. Kang, K. W. (2012). Blast resistance of steel-concrete composite structures (Doctoral dissertation, Dissertation, National University of Singapore).

49. Kazemahvazi, S., Nilsson, M., & Zenkert, D. (2014). Residual strength of GRP laminates with multiple randomly distributed fragment impacts. *Composites Part A: Applied Science and Manufacturing*, *60*, 66-74.

50. Khan, A. (2021). *Behaviour of Steel and Steel-Concrete Sandwich Panels under Combined Blast and Fragment Loadings* (Doctoral dissertation, UNSW Sydney).

51. Kingery, C. N., & Bulmash, G. (1984). Technical report ARBRL-TR-02555: Air blast parameters from TNT spherical air burst and hemispherical burst. *AD-B082*, *713*.

52. Knock, C., & Davies, N. (2013). Blast waves from cylindrical charges. *Shock Waves*, *23*(4), 337-343.

53. Koos, R. (1987). Die kombinierte Luftstoss-splitter-Last, eine quantitiv bestimmbare Grösse für die Schutzbaubemessung. In *Internationales Symposium, Interaktion Konventioneller Munition mit Schutzbauten* (Vol. 1, p. 348).

54. Krauthammer, T. (2008). *Modern protective structures* (Vol. 22). Crc Press.

55. Krauthammer, T., Shahriar, S., & Shanaa, H. M. (1990). Response of reinforced concrete elements to severe impulsive loads. *Journal of Structural Engineering*, *116*(4), 1061-1079.

56. Lan, S., Lim, H. S., Ow, M. C., & Morrill, K. B. (2015, November). Reinforced Concrete Slab Under Combined Blast and Fragment Loading. In *for the 16th International symposium on the Interaction of the Effects on Munitions with Structures, Florida*.

57. Lan, S., & Morrill, K. B. (2016, April). Numerical simulation for combined blast & fragment effects on RC slabs. In *Proceedings of the 7th international conference on computational methods (ICCM)*.

58. Lan, S., & Heng, L. (2002). Composite structural components under blast loading. *WIT Transactions on The Built Environment*, *63*.

59. Lan, S., Lok, T. S., & Heng, L. (2005). Composite structural panels subjected to explosive loading. *Construction and Building Materials*, *19*(5), 387-395

60. Liew, R., Yan, J., Huang, Z., (2017), *Steel-concrete-steel sandwich composite structures-recent innovations*, Journal of Constructional Steel Research, 130 (2017) 202–221.

61. Liew, J. R., Yan, J. B., & Huang, Z. Y. (2017). Steel-concrete-steel sandwich composite structures-recent innovations. *Journal of constructional Steel research*, *130*, 202-221.

62. J.Y.R. Liew, T.Y. Wang, Novel steel-concrete-steel sandwich composite plates subject to impact and blast load, Adv. Struct. Eng. 14 (4) (2010) 673–687.

63. Liew, J. R., & Wang, T. Y. (2011). Novel steel-concrete-steel sandwich composite plates subject to impact and blast load. *Advances in Structural Engineering*, *14*(4), 673-687.

64. Li, Y., Chen, Z., Ren, X., Tao, R., Gao, R., & Fang, D. (2020). Experimental and numerical study on damage mode of RC slabs under combined blast and fragment loading. *International Journal of Impact Engineering*, *142*, 103579.

65. Leppänen, J. (2006). Concrete subjected to projectile and fragment impacts: Modelling of crack softening and strain rate dependency in tension. *International Journal of Impact Engineering*, *32*(11), 1828-1841.

66. Leppänen, J. (2005). Experiments and numerical analyses of blast and fragment impacts on concrete. International Journal of Impact Engineering, 31(7), 843-860.

67. Leppänen, J. (2004). *Concrete structures subjected to fragment impacts*. Chalmers Tekniska Hogskola (Sweden).

68. Leppänen, J. (2002). *Dynamic behaviour of concrete structures subjected to blast and fragment impacts* (Doctoral dissertation, Chalmers tekniska högsk.).

69. Malvar, L. J., Crawford, J. E., Wesevich, J. W., & Simons, D. (1997). A plasticity concrete material model for DYNA3D. *International journal of impact engineering*, *19*(9-10), 847-873.

70. Magnusson, J., & Hansson, H. (2005). Numerical Simulations of Concrete Beams-A Principal Study. *National Defence Research Establishment, Sweden*, 63.

71. Marchand, K. A., Vargas, M. M., & Nixon, J. D. (1992). The synergistic effects of combined blast and fragment loadings. *San Antonio, Texas*.

72. McKinley, B., & Boswell, L. F. (2002). Behaviour of double skin composite construction. *Journal of constructional steel research*, *58*(10), 1347-1359.

73. Nordstrom, M., & Forsén, R. (1970). Damage to reinforced concrete slabs due to fragment loading with different fragment velocities, fragment areal densities and sizes of fragments. *WIT Transactions on The Built Environment*, *8*.

74. Nordstrom, M., & Forsén, R. (1994). Damage to reinforced concrete slabs due to fragment loading with different fragment velocities, fragment areal densities and sizes of fragments. *WIT Transactions on The Built Environment*, *8*.

75. Nyström, U., & Gylltoft, K. (2009). Numerical studies of the combined effects of blast and fragment loading. *International journal of impact engineering*, *36*(8), 995-1005.

76. Nyström, U. (2013). Modelling of concrete structures subjected to blast and fragment loading. Chalmers University of Technology.

77. Rana, M. M., Khan, A., Del Linz, P., Lee, C. K., & Fung, T. C. (2019). Effect of cased charges on plain steel and steel-concrete sandwich targets. *Thin-Walled Structures*, *136*, 302-314.

78. Randers-Pehrson, G., & Bannister, K. (1997). *Airblast loading model for DYNA2D and DYNA3D*. Army Research Laboratory.

79. Ren, G. M., Wu, H., Fang, Q., & Liu, J. Z. (2018). Effects of steel fiber content and type on dynamic compressive mechanical properties of UHPCC. *Construction and building materials*, *164*, 29-43.

80. Riedel, W. (2000). *Beton unter dynamischen Lasten: Meso-und makromechanische Modelle und ihre Parameter*. London: EMI. [in German].

81. Riedel, W., Thoma, K., Hiermaier, S., & Schmolinske, E. (1999, May). Penetration of reinforced concrete by BETA-B-500 numerical analysis using a new macroscopic concrete model for hydrocodes. In *Proceedings of the 9th International Symposium on the Effects of Munitions with Structures* (Vol. 315). Berlin-Strausberg Germany.

82. Riedel, W. (2009). 10 years RHT: A review of concrete modelling and hydrocode applications. *Predictive Modeling of Dynamic Processes: A Tribute to Professor Klaus Thoma*, 143-165.

83. R.G. Whirley and J. O. Hallquist, D YNA3D: A Nonlinear Explicit Three, Dimensional Finite Element Code Jbr Solid and Structural Mechanics, User Manual, Report UCRL-MA-107254, Lawrence Livermore National Laboratory, Livermore, CA, 1991

84. Schwartz, A. (1964). Report on Summary and Analysis of Full Scale Dividing Wall Tests and Comparisons with Analytically Predicted Results. *Ammunition Engineering Directorate, Picatinny Arsenal, Dover, NJ*.

85. Sobeski, R., & Urgessa, G. (2015). Review of quasi-analytical and cavity expansion methods for projectile penetration of concrete targets. *International Journal of Protective Structures*, *6*(1), 43-64.

86. Taylor, G. I. (1941). Analysis of the explosion of a long cylindrical bomb detonated at one end. *Mechanics of Fluids, Scientific Papers of GI Taylor*, *2*, 277-286.

87. Warren, T. L., Forrestal, M. J., & Randles, P. W. (2014). Evaluation of large amplitude deceleration data from projectile penetration into concrete targets. *Experimental Mechanics*, *54*(2), 241-253.

88. Wu, C., Fattori, G., Whittaker, A., & Oehlers, D. J. (2010). Investigation of air-blast effects from spherical-and cylindrical-shaped charges. *International Journal of Protective Structures*, *1*(3), 345-362.

89. Wu, Y., Crawford, J. E., Lan, S., & Magallanes, J. M. (2014, June). Validation studies for concrete constitutive models with blast test data. In *Proc., 13th Int. LS-DYNA® Users Conf., LSTC, Livermore, CA*.

90. Wu, J., & Liu, X. (2015). Performance of soft-hard-soft (SHS) cement based composite subjected to blast loading with consideration of interface properties. *Frontiers of structural and civil engineering*, *9*, 323-340.

91. Wu, J., Liu, Z., Yu, J., & Xu, S. (2022). Experimental and numerical investigation of normal reinforced concrete panel strengthened with polyurea under near-field explosion. *Journal of Building Engineering*, *46*, 103763.

92. US Army Corp of Engineers (2008), *Methodology Manual for the Single-Degree-of-Freedom Blast Effects Design Spreadsheets (SBEDS)*, PDC TR-06-01 Rev 1, U.S. Army Corps of Engineers Protective Design Center.

93. Varma, A. H., Malushte, S. R., Sener, K. C., & Lai, Z. (2014). Steel-plate composite (SC) walls for safety related nuclear facilities: Design for in-plane forces and out-of-plane moments. *Nuclear Engineering and Design*, *269*, 240-249.

94. Yu, S., Wu, H., Zhang, G., Wang, Z., Yao, J., Li, H., & Liu, C. (2023). Experimental study on anti-shallow-buried-explosion capacity of a corrugated steel-plain concrete composite structure. *International Journal of Impact Engineering*, *172*, 104393.

95. Yu, S., Zhang, G., Wang, Z., Liu, J., Deng, S., Song, X., & Wang, M. (2024). Experimental and numerical study of corrugated steel-plain concrete composite structures under contact explosions. *Thin-Walled Structures*, *197*, 111624.

96. Yu, J., Liang, S. L., Ren, Z. P., Deng, Y. J., & Fang, Q. (2023). Structural behavior of steel-concrete-steel and steel-ultra-high-performance-concrete-steel composite

panels subjected to near-field blast load. *Journal of Constructional Steel Research*, *210*, 108108.

97. Zimmerman, H.D., Nguyen, H.D., and Hookham, P. A., (1999), "Investigation of Spherical vs Cylindrical Shape Effects on Peak Free-Air Overpressure and Impulse", *In proceedings of 9th International Symposium on Interaction of the Effects of Munitions with Structures*. Berlin-Strausberg, Germany.

98. Zhao, C.F. (2021). *Blast Behavior of steel-concrete-steel-sandwich panel: Experiment and numerical simulation.* Engineering Structures, 246.

99. Zhou, Y., Xie, Y. C., Pan, T., Zhu, W., Zhang, H., & Huang, G. Y. (2023). Flexible materials and structures for mitigating combined blast and fragment loadings–A review. *International Journal of Impact Engineering*, *181*, 104759.

100. Zhang, P., Mo, D., Ge, X., Wang, H., Zhang, C., Cheng, Y., & Liu, J. (2022). Experimental investigation into the synergetic damage of foam-filled and unfilled corrugated core hybrid sandwich panels under combined blast and fragment loading. *Composite Structures*, *299*, 116089.

101. Zhu, W., Xiao, Y., Yu, J., Jia, J., & Li, Z. (2024). Damage modes and mechanism of steel-concrete composite bridge slabs under contact explosion. *Journal of Constructional Steel Research*, *212*, 108223.

102. Zulkoski, T. (1976). Development of optimum theoretical warhead design criteria. *Naval Weapons Center China Lake: Kern County, CA, USA*.

103. Zook, J. (1977). An analytical model of kinetic energy projectile/fragment penetration. *USA Ballistic Research Laboratory, BRL MR*, *2797*.

104. Zukas, J. A., & Scheffler, D. R. (2000). Practical aspects of numerical simulations of dynamic events: effects of meshing. *International journal of impact engineering*, *24*(9), 925-945.